



Title	Isotopic signature of oxygen and magnesium for coarse-grained Ca-Al-rich inclusions from carbonaceous chondrites
Author(s)	川崎, 教行
Citation	北海道大学. 博士(理学) 甲第11805号
Issue Date	2015-03-25
DOI	10.14943/doctoral.k11805
Doc URL	<a href="http://hdl.handle.net/2115/58834">http://hdl.handle.net/2115/58834</a>
Type	theses (doctoral)
File Information	Noriyuki_Kawasaki.pdf



[Instructions for use](#)

**Isotopic signature of oxygen and magnesium  
for coarse-grained Ca-Al-rich inclusions  
from carbonaceous chondrites**

(炭素質コンドライトに含まれる粗粒難揮発性包有物の  
酸素・マグネシウム同位体宇宙化学)

A dissertation submitted for the doctoral degree of science

presented by

**Noriyuki Kawasaki**

Department of Natural History Sciences

Graduate School of Science

Hokkaido University

2015

## Contents

ABSTRACT.....	1
1. INTRODUCTION.....	4
2. EXPERIMENTAL.....	7
2.1 SAMPLE PREPARATIONS AND PETROGRAPHIC OBSERVATIONS.....	7
2.2 OXYGEN ISOTOPE ANALYSIS .....	7
2.3 MAGNESIUM ISOTOPE ANALYSIS.....	8
3. OXYGEN ISOTOPIC AND CHEMICAL ZONING OF MELILITE CRYSTALS IN A FLUFFY TYPE A CA-AL-RICH INCLUSION OF EFREMOVKA CV3 CHONDRITE.....	10
3.1 RESULTS.....	10
3.1.1 <i>Mineralogy and Petrology</i> .....	10
3.2 DISCUSSION .....	17
3.2.1 <i>Oxygen isotopic compositions and chemical zoning of melilite crystals in domain-1</i> .....	17
3.2.2 <i>Oxygen isotopic compositions and chemical zoning of melilite crystals in domain-2</i> .....	19
3.2.3 <i>Formation sequence of HKE 01</i> .....	20
3.3 CONCLUSIONS.....	21
4. <sup>26</sup> AL-MG CHRONOLOGY AND OXYGEN ISOTOPE DISTRIBUTIONS OF MULTIPLE MELTING FOR A TYPE C CAI FROM ALLENDE CV3 .....	24
4.1 RESULTS.....	24
4.1.1 <i>Mineralogy and Petrology</i> .....	24
4.1.2 <i>Oxygen isotopic compositions of minerals</i> .....	29
4.1.3 <i>Magnesium isotopic compositions of minerals</i> .....	32
4.2 DISCUSSION .....	34
4.2.1 <i>Multiple melting of EK1-04-2</i> .....	34
4.2.2 <i><sup>26</sup>Al-Mg chronology of multiple melting of EK1-04-2</i> .....	39
4.3 CONCLUSIONS.....	45
5. <sup>26</sup> AL-MG CHRONOLOGY AND MAGNESIUM ISOTOPIC FRACTIONATION FOR REVERSELY ZONED MELILITE CRYSTALS IN A FLUFFY TYPE A CAI FROM VIGARANO CV3 .....	47
5.1 RESULTS.....	47

5.1.1 Petrographic observation.....	47
5.1.2 Chemical and oxygen isotopic zoning of reversely zoned melilite crystals.....	48
5.1.3 <sup>26</sup> Al-Mg isochrons of reversely zoned melilite crystals .....	51
5.1.4 Magnesium isotopic fractionations of reversely zoned melilite crystals .....	54
5.1.5 Oxygen and magnesium isotopic compositions of the accessory minerals .....	56
5.2 DISCUSSION .....	57
5.2.1 Formation processes of reversely zoned melilite crystals.....	57
5.2.2 Time duration for the formation of reversely zoned melilite crystals .....	61
5.2.3 Interpretation of initial ( <sup>26</sup> Al/ <sup>27</sup> Al) <sub>0</sub> for melilite in V2-01.....	62
5.2.4 Formation of V2-01 fluffy Type A CAI.....	63
5.2.5 Implication for astrophysical setting of Type A CAI-forming region .....	64
5.3 CONCLUSIONS .....	65
6. IMPLICATIONS AND FUTURE WORKS.....	67
ACKNOWLEDGEMENTS .....	70
REFERENCES .....	71

## ABSTRACT

Ca-Al-rich inclusions (CAIs) in meteorites are composed of high-temperature minerals and are the oldest objects in the Solar System formed at 4567 Ma. Disequilibrium oxygen isotopic distributions among inter- and intra-crystals have been observed for coarse-grained CAIs, which correspond mainly to multiple melting events and oxygen isotope exchanges between the melt and the surrounding gas with different oxygen isotopic composition in the solar nebula. On the other hand, fluffy Type A CAIs are believed to be direct condensates from a solar nebular gas, and therefore, have acquired oxygen from the solar nebular gas.  $^{26}\text{Al}$ -Mg systematics may be applicable for age differences among individual formation events of CAIs including melting events and condensation. In this thesis, I have conducted coordinate study of oxygen and/or magnesium isotope measurements by SIMS and precise petrographic observations for three coarse-grained CAIs, (1) Type A CAI from the Efremovka CV3, (2) Type C CAI from the Allende CV3, and (3) fluffy Type A CAI from the Vigarano CV3. Main purposes of thesis are to reveal the temporal variation of oxygen isotopic composition of surrounding nebular gas during CAI formation, and to determine the ages of individual formation events throughout the entire formations of the CAIs. The thesis consists of three parts as follows:

**(1) Oxygen isotopic and chemical zoning of melilite crystals in a Type A Ca-Al-rich inclusion of Efremovka CV3 chondrite:** The Type A CAI from the Efremovka CV3 is constructed of two domains, each of which has a core-mantle structure. Reversely zoned melilite crystals were observed in both domains. Melilite crystals in one domain have a homogeneous  $^{16}\text{O}$ -poor composition on the carbonaceous chondrite anhydrous mineral (CCAM) line of  $\delta^{18}\text{O} = 5\text{-}10\text{‰}$ , which suggests that the domain was formed in a  $^{16}\text{O}$ -poor oxygen isotope reservoir of the solar nebula. In contrast, melilite crystals in the other domain have continuous variations of oxygen isotopic composition from  $^{16}\text{O}$ -rich ( $\delta^{18}\text{O} = -40\text{‰}$ ) to  $^{16}\text{O}$ -poor ( $\delta^{18}\text{O} = 0\text{‰}$ ) along a carbonaceous chondrite anhydrous mineral (CCAM) line. The oxygen isotopic composition tends to be more  $^{16}\text{O}$ -rich towards the domain rim, which suggests that the domain was formed in a variable oxygen isotope reservoir of the solar nebula. Each domain of the Type A CAI has grown in distinct oxygen isotope reservoir of the solar nebula. After the domain formation, domains were accumulated together in the solar nebular to form a Type A CAI.

**(2)  $^{26}\text{Al}$ -Mg chronology and oxygen isotope distributions of multiple melting for a Type C CAI from Allende CV3:** The Type C CAI from the Allende CV3

consists mainly of spinel, anorthite, olivine, and pyroxene, and has a core and mantle structure. Petrography of the core suggests that the crystallization sequences of the core minerals are spinel, anorthite, olivine, and pyroxene. The mantle has the same mineral assemblages as the core, and shows incomplete melting and solidification textures. Oxygen isotopic compositions of the minerals are distributed along with the CCAM line ( $\delta^{18}\text{O} = -44$  to  $+9\%$ ), which indicates to preserve a chemical disequilibrium status in the CAI. Spinel shows  $^{16}\text{O}$ -rich signature ( $\delta^{18}\text{O} \sim -43\%$ ), while anorthite shows  $^{16}\text{O}$ -poor signature ( $\delta^{18}\text{O} \sim +8\%$ ). Olivine and pyroxene in the core have the same oxygen isotopic composition ( $\delta^{18}\text{O} \sim -15\%$ ), which indicates their equilibrium. Olivine and pyroxene in the mantle have variable oxygen isotopic compositions and are slightly depleted in  $^{16}\text{O}$  ( $\delta^{18}\text{O} = -13$  to  $-4\%$ ) compared with the same minerals in the core. The  $^{26}\text{Al}$ -Mg systematics is consistent with the disequilibrium status observed according to the petrography and oxygen isotopes. Spinel is plotted on a line of  $(^{26}\text{Al}/^{27}\text{Al})_0 = (3.5 \pm 0.2) \times 10^{-5}$ , anorthite is  $(-1 \pm 5) \times 10^{-7}$ , and olivine and pyroxene in the core are  $(-1 \pm 7) \times 10^{-6}$ . Plots of olivine and pyroxene in the mantle are scattered below the isochron of these minerals in the core. The coordinated study of the oxygen and magnesium isotopes and the petrography indicates that the EK1-04-2 Type C CAI underwent multiple heating events after a precursor CAI formation. The precursor CAI was formed at 0.43 Myr after the formation of the Solar System defined by canonical CAI formation. At least 1.6 Myr after the precursor CAI formation, the CAI was partially melted and the partial melting melt exchanged oxygen isotopes with surrounding  $^{16}\text{O}$ -poor nebular gas.  $^{16}\text{O}$ -poor olivine and pyroxene in the core were crystallized from the partial melting melt. Subsequently, Al-rich chondrules accreted on the CAI, and the CAI experienced partial melting again and recrystallized to form the mantle. The oxygen and magnesium isotopes in anorthite were redistributed during thermal metamorphism in the Allende parent body. This study reveals that the CAI had been retained in the solar nebula for at least 1.6 Myr and underwent multiple melting events in the nebula, and oxygen and  $^{26}\text{Al}$ -Mg systematics has been partially disturbed depending on crystal sizes by metamorphism on the parent body.

**(3)  $^{26}\text{Al}$ -Mg chronology and magnesium isotopic fractionation for reversely zoned melilite crystals in a fluffy Type A CAI from Vigarano CV3:** In the fluffy Type A CAI, three patterns of magnesium isotopic fractionation within the melilite grains have been found. The  $\delta^{25}\text{Mg}$  values were the constant at two grains ( $\delta^{25}\text{Mg} = 1$  and  $2\%$ , respectively). Other two grains have continuous variations of  $\delta^{25}\text{Mg}$  changing from heavy ( $\sim 6\%$ ) to light ( $\sim 0\%$ ) along with the crystal growth, which is an opposite trend expected for the crystallization of reversely zoned melilite crystals from a melt

with melt evaporation. These grains were likely formed by the condensation from the solar nebular gas of which oxygen isotopic compositions were changed from  $^{16}\text{O}$ -poor to  $^{16}\text{O}$ -rich and  $\delta^{25}\text{Mg}$  became smaller. In contrast, other two grains have continuous variations of  $\delta^{25}\text{Mg}$  changing from light to heavy along with the crystal growth ( $\sim 1$  to  $\sim 5\%$  and  $\sim 4$  to  $\sim 10\%$ , respectively), which can be explained by both the condensation from solar nebular gas and the crystallization from the melt with melt evaporation. The single  $^{26}\text{Al}$ -Mg isochrons are obtained for each six reversely zoned melilite crystal. The initial  $(^{26}\text{Al}/^{27}\text{Al})_0$  for each grain was the same within analytical error. The  $^{26}\text{Al}$ -Mg systematics indicates the formation of these grains occurred at  $0.12 \pm 0.03$  Myr after the canonical CAI formation and the time durations for their formation were less than 0.12-0.28 Myr. The formation regions for these reversely zoned melilite crystals may correspond to the inner edge region of the solar nebula where  $^{16}\text{O}$ -rich solar and  $^{16}\text{O}$ -poor planetary gases are encountered and mixed. The oxygen isotope change of solar nebular gas from  $^{16}\text{O}$ -poor to  $^{16}\text{O}$ -rich occurred at the time scale for less than 0.12 Myr. The  $\delta^{25}\text{Mg}$ -enrichment for gas ( $\sim 6\%$ ) could be produced by a vaporization of coarse-grained CAIs in the inner edge region of disk having high dust-to-gas ratio. Our study shows that each reversely zoned melilite crystals were locally formed at distinct environment in the early Solar System within 0.28 Myr, and accreted together to form V2-01.

## 1. Introduction

Ca-Al-rich inclusions (CAIs) in meteorites are composed of high-temperature minerals (Grossman, 1972) and the oldest objects in the Solar System formed at 4567 Ma (Amelin et al., 2002; Connelly et al., 2012). CAIs were classified into coarse-grained CAIs and fine-grained CAIs according to their crystal sizes. Coarse-grained CAIs are mainly observed in CV3 chondrites and almost absent in other subtypes of carbonaceous chondrite or other chondrite group. Coarse-grained CAIs are classified petrographically into the Type A, Type B, and Type C CAI. Type A CAIs are mainly composed of melilite, Type B CAIs are mainly composed of melilite and fassaite, and Type C CAIs contain abundant anorthite (Grossman, 1975; MacPherson, 2003). The Type A CAIs are subdivided into compact and fluffy CAIs (Grossman, 1980). Compact Type A, Type B, and Type C CAIs are believed to undergo partial or total melting, according to the major and trace element chemistry of the coexisting minerals and experimental petrology (MacPherson and Grossman, 1981; Wark and Lovering, 1982; Beckett and Stolper, 1994; Simon et al., 1999). In contrast, fluffy Type A CAIs are considered to be formed by gas-solid condensation and not extensive molten, because of their irregular shapes and the presence of reversely zoned melilite crystals that have magnesium-rich cores and aluminum-rich mantles (MacPherson and Grossman, 1984).

CAIs show heterogeneous oxygen isotopic compositions of their constitute minerals along the carbonaceous chondrite anhydrous mineral (CCAM) line (Clayton et al., 1977; Clayton, 1993). In-situ oxygen isotopic analyses by secondary ion mass-spectrometry (SIMS) have revealed disequilibrium oxygen isotopic distributions among inter- and intra-crystals of CAIs (Yurimoto et al., 1994; Yurimoto et al., 1998; Yurimoto et al., 2008). The disequilibrium oxygen isotopic distributions in the CAIs are interpreted to be results of multiple melting processes (Yurimoto et al., 1998; Ito et al., 2004; Yoshitake et al., 2005; Krot et al., 2008; Yurimoto et al., 2008; Wakaki et al., 2013), condensation processes (Katayama et al., 2012; Kawasaki et al., 2012; Park et al., 2012) and solid state diffusion processes (Fagan et al., 2004a) in the solar nebula with different oxygen isotopic environments (Itoh and Yurimoto, 2003; Yurimoto and Kuramoto, 2004) and also aqueous and thermal metamorphism/alteration on the parent body (Wasson et al., 2001). The combinations of such processes have formed the disequilibrium oxygen isotopic distributions in the CAI, although most efficient processes are different at each mineral and each CAI. In order to determine the oxygen isotope exchange processes, high spatial resolution studies of isotopic and chemical distributions and the petrography are important (e.g., Yurimoto et al., 1998).

The reverse zoning of melilite in fluffy Type A CAIs is readily explained by direct condensation from a solar nebular gas with decreasing pressure (MacPherson and Grossman, 1984). Therefore, the oxygen isotopic compositions of reversely zoned melilite in fluffy Type A CAIs are identical to those of the surrounding solar nebular gas. The reversely zoned melilite crystals of a fluffy Type A CAI from Vigarano CV3 chondrite have heterogeneous oxygen isotopic distributions correlated with the chemical compositions (Harazono and Yurimoto 2003; Yurimoto et al. 2008; Katayama et al. 2012), where magnesium-rich melilite was  $^{16}\text{O}$ -poor and aluminum-rich melilite was  $^{16}\text{O}$ -rich. It is considered that the oxygen isotopic compositions of the solar nebular gas that formed the reversely zoned melilite in Type A CAI were changed from  $^{16}\text{O}$ -poor to  $^{16}\text{O}$ -rich during condensation of the melilite, and each fluffy domain in the CAI may have been formed separately in the nebula and then accumulated together to form the CAI. However, there are very few studies of that focus have been made on the relationship between oxygen isotopic and chemical compositions of condensed melilite. In addition, the formation ages of the individual melilite crystals have not been studied in depth. The investigation of time durations for the formation of each reversely zoned melilite crystal can be direct determination of the time scale for oxygen isotope change of the solar nebular gas from  $^{16}\text{O}$ -poor to  $^{16}\text{O}$ -rich. On the other hand, in contrast to the condensation model for the formation of reversely zoned melilite crystals in fluffy Type A CAIs, crystallization of them from incomplete melt with melt evaporation was also suggested (Grossman et al., 2002). Significant mass dependent fractionation of magnesium isotopes was expected for the melt evaporation processes (Richter et al., 2002; Richter et al., 2007; Mendybaev et al., 2013). Thus, the formation process can be tested by the magnesium isotope analyses using SIMS along with the reverse zoning.

The crystals formed by the condensation directly conserve the oxygen isotopes of the surrounding nebular gas. In contrast, the oxygen isotopic distributions of multiple melted CAIs are controlled by exchanges of oxygen isotopes between the CAI melts and the surrounding nebular gas. If CAIs have experienced multiple incomplete melting by heating events in the solar nebula, the partial melting melts exchanged their oxygen isotopes with the surrounding nebular gas with various oxygen isotopic compositions at the melting events (Yurimoto et al., 1998; Yurimoto et al., 2008). Highest temperatures and cooling rates of the CAI melting events have been determined by experimental petrologic studies (Stolper, 1982; MacPherson et al., 1984; Stolper and Paque, 1986; Beckett and Stolper, 1994; Tronche et al., 2007). Many CAIs show a record of live- $^{26}\text{Al}$  at their formation, which is a short-lived radionuclide with a half-life of 0.73 Myr (MacPherson et al., 1995). Thus, a relative chronometer with  $^{26}\text{Al}$ -Mg systematics has

been applied for determining time interval of the heating events in the early Solar System (e.g., Kita et al., 2012; MacPherson et al., 2012; Mishra and Chaussidon, 2014). However, age differences between individual CAI melting events have been poorly studied.

In this thesis, I have conducted coordinate study of oxygen and/or magnesium isotope measurements by SIMS and precise petrographic observations for three CAIs, Type A CAI from the Efremovka CV3 (chapter 3), Type C CAI from the Allende CV3 (chapter 4), and fluffy Type A CAI from the Vigarano CV3 (chapter 5). It is noted that chapter 3 is essentially taken from a paper published in the *Meteoritics and Planetary Science* (Kawasaki et al., 2012), chapter 4 is from a manuscript submitted to the *Geochimica et Cosmochimica Acta*, and chapter 5 is from a manuscript to be prepared for submitting to the *Geochimica et Cosmochimica Acta*.

In chapter 3, the chemical compositions and oxygen isotopic distributions of melilite in a Type A CAI from Efremovka CV3 chondrite were studied to elucidate the formation processes and variations of oxygen isotopic composition of the solar nebular gas of Type A CAI forming area.

In chapter 4, I have conducted a coordinated study of oxygen and magnesium isotope measurements using SIMS and detailed petrographic observations for a Type C CAI, EK1-04-2 from Allende CV3, to determine the melting events and history of the CAI. Precise petrographic observations and oxygen isotopic measurements were performed to understand the individual melting processes that occurred in the CAI. Investigation of the  $^{26}\text{Al}$ -Mg systematics was then performed for minerals formed by different melting and recrystallization processes to determine the age differences of individual CAI melting events.

In chapter 5, I have conducted the  $^{26}\text{Al}$ -Mg systematics using SIMS for six single reversely zoned melilite crystals in V2-01, the fluffy Type A CAI from the Vigarano CV3 of that chemical and oxygen isotopic zoning were studied by Katayama et al. (2012), in order to determine the ages of individual reversely zoned melilite crystals, and the time scale for oxygen isotope change of the solar nebular gas. The magnesium isotope distributions for each single reversely zoned melilite crystal were simultaneously investigated to test the models for formation process. In addition, we also have measured oxygen and Al-Mg isotopic compositions of accessory minerals in V2-01, diopside, hibonite and spinel, to be compared with those of melilite.

## 2. Experimental

### 2.1 Sample preparations and petrographic observations

The CAIs were examined using backscattered electron (BSE) imaging, X-ray elemental analyses, electron back scattered diffraction (EBSD) mapping and secondary ion mass-spectrometry (SIMS). The Type A CAI, HKE 01 (Kawasaki et al., 2012) is from a polished section of the Efremovka CV3. The Type C CAI, EK1-04-2 (Ito et al., 2000) is a CAI fragment from the Allende CV3. The fluffy Type A CAI, V2-01 (Katayama et al., 2012) is from a polished thin section of the Vigarano CV3.

The sections of CAI were coated with a carbon thin film (~20 nm) for petrologic observations and with a gold thin film (~70 nm) for isotope measurements with SIMS. The BSE images were obtained using a field emission type scanning electron microscope (FE-SEM; JEOL JSM-7000F) of Hokkaido University. Chemical compositions of CAI minerals and X-ray elemental maps were obtained with an energy dispersive X-ray spectrometer (EDS; Oxford INCA, Oxford X-Max 150) installed with the FE-SEM. A 15 keV electron beam probe with a current of 0.3 to 0.9 nA and 5 to 10 nA was used for a quantitative elemental analysis and an X-ray elemental mapping, respectively. Crystal orientation mapping of the minerals was obtained using an EBSD system (HKL Channel 5) equipped with the FE-SEM to determine the grain boundaries of each mineral crystals using a 15 or 20 keV electron beam probe with a current of 4 to 10 nA.

### 2.2 Oxygen isotope analysis

Oxygen isotopic compositions of the minerals were measured using SIMS instruments (Cameca ims-1270; ims-1280HR) of Hokkaido University. A  $^{133}\text{Cs}^+$  primary beam (20 keV, 60 to 200 pA) with a diameter of 2 to 10  $\mu\text{m}$  was used. Negative secondary ions ( $^{16}\text{O}^-$ ,  $^{17}\text{O}^-$ , and  $^{18}\text{O}^-$ ) were measured. A normal incident electron flood gun was used for a charge compensation of sample surface charging during the measurements.  $^{16}\text{O}^-$  was measured using a faraday cup while  $^{17}\text{O}^-$  and  $^{18}\text{O}^-$  were measured using an electron multiplier with the peak jumping mode of a sector magnet. The mass resolution of  $M/\Delta M$  was set to ~5500 to achieve a contribution of  $^{16}\text{OH}^-$  to  $^{17}\text{O}^-$  were negligible. Secondary ion intensity of  $^{16}\text{O}^-$  was 0.5 to  $1 \times 10^8$  cps. Each measurement was conducted for 30 cycles of a counting sequence with  $^{16}\text{O}^-$  for 1s,  $^{17}\text{O}^-$  for 2s and  $^{18}\text{O}^-$  for 1s. Russian spinel and synthetic åkermanite glass with known oxygen isotopic compositions were used as standards to correct the instrumental mass

fractionation.

### 2.3 Magnesium isotope analysis

Magnesium isotopic compositions and Al/<sup>24</sup>Mg ratios of the minerals were measured using SIMS instruments (Cameca ims-1270; ims-1280HR) of Hokkaido University. An <sup>16</sup>O<sup>-</sup> primary beam accelerated to 23 keV was used. For minerals of pyroxene, olivine and spinel, magnesium isotopes (<sup>24</sup>Mg<sup>+</sup>, <sup>25</sup>Mg<sup>+</sup> and <sup>26</sup>Mg<sup>+</sup>) and <sup>27</sup>Al<sup>+</sup> were measured simultaneously using a multicollecion mode with four Faraday cups: <sup>24</sup>Mg<sup>+</sup> for L2\* (10<sup>10</sup> Ω at ims-1270 and 10<sup>11</sup> Ω at ims-1280HR), <sup>25</sup>Mg<sup>+</sup> for C (10<sup>11</sup> Ω), <sup>26</sup>Mg<sup>+</sup> for H1 (10<sup>11</sup> Ω) and <sup>27</sup>Al<sup>+</sup> for H2\* (10<sup>10</sup> Ω). The primary beam current was set to 12 nA (pyroxene and spinel) and 5 nA (olivine) with a diameter of ~20 μm and ~15 μm, respectively. The mass resolution of M/ΔM was set to ~2000. The contributions of ion interferences (e.g., <sup>52</sup>Cr<sup>2+</sup>, <sup>24</sup>MgH<sup>+</sup>, <sup>48</sup>Ca<sup>2+</sup>) were negligible at these conditions. Secondary ion intensities of <sup>24</sup>Mg<sup>+</sup> were 1.4 to 2.5 × 10<sup>8</sup> cps, 2.7 × 10<sup>8</sup> cps and 2.4 × 10<sup>8</sup> cps for pyroxene, spinel and olivine, respectively. Each measurement was conducted for 20 cycles of a counting time of 10s. An instrumental mass fractionation of SIMS was determined by measurements of Takashima augite, synthetic fassaite glass, San Carlos olivine and Russian spinel for each mineral because mass fractionation factor is not equivalent within analytical error between minerals under the measurement condition (Itoh et al., 2008). After the collection of the instrumental mass fractionation of SIMS, excess of radiogenic <sup>26</sup>Mg was calculated using an exponential fractionation law with the slope of 0.514 because natural fractionation for magnesium isotopes is believed to be controlled by the evaporation processes (Davis et al., 2005). A detail of the calculation methods for the instrumental mass fractionation and the excess of radiogenic <sup>26</sup>Mg was described elsewhere (Itoh et al., 2008). The relative sensitivity factor for aluminum and magnesium were determined for each mineral by measurements of synthetic fassaite glass, San Carlos olivine and Russian spinel.

For melilite and anorthite, magnesium isotopes (<sup>24</sup>Mg<sup>+</sup>, <sup>25</sup>Mg<sup>+</sup> and <sup>26</sup>Mg<sup>+</sup>) were measured using an electron multiplier while <sup>27</sup>Al<sup>+</sup> was measured using a Faraday cup with the peak jumping mode of a sector magnet. The <sup>16</sup>O<sup>-</sup> primary beam accelerated to 23 keV was used and secondary ion intensity of <sup>24</sup>Mg<sup>+</sup> was set to 1 to 3 × 10<sup>5</sup> cps under mass resolution of M/ΔM of ~3500. Because melilite crystals in V2-01 show the chemical zonation, primary beam current was adjusted for each spot according to the chemical compositions. Under these conditions, the primary beam current was about 0.2 to 1 nA with a diameter of 2 to 10 μm. Each measurement was conducted for 50 cycles of a counting sequence with <sup>24</sup>Mg<sup>+</sup> for 3s, <sup>25</sup>Mg<sup>+</sup> for 10s, <sup>26</sup>Mg<sup>+</sup> for 10s and <sup>27</sup>Al<sup>+</sup> for 1s.

An instrumental mass fractionation and the relative sensitivity factor for aluminum and magnesium were determined by measurements of Miyakejima anorthite and synthetic åkermanite glass. Other calculations to estimate the excess of radiogenic  $^{26}\text{Mg}$  are the same as described above.

### 3. Oxygen isotopic and chemical zoning of melilite crystals in a fluffy

#### Type A Ca-Al-rich inclusion of Efremovka CV3 chondrite

##### 3.1 RESULTS

###### 3.1.1 Mineralogy and Petrology

Fig. 1 shows a BSE image of a Type A CAI from Efremovka CV3 chondrite, named HKE 01. The CAI is 10×4 mm and has an irregular texture. The CAI is mainly composed of melilite (62%), spinel (19%), and fassaite (13%), in addition to diopside, anorthite, forsterite, hibonite and metal grains as accessory minerals. Nepheline is present as a secondary alteration mineral, although the amounts are very small. The CAI is surrounded by mineral layers of gehlenitic melilite, spinel and diopside, referred to as a Wark-Lovering (W-L) rim (Wark and Lovering 1977). The W-L rim divides the CAI into two domains. Fig. 2 shows that the W-L rim, which is composed of spinel and diopside layers, separates the CAI into two domains; domain-1 and domain-2. A matrix is observed between the W-L rims of both domains.

The area of domain-1 is dominant in the CAI and it has a core-mantle structure enclosed by a W-L rim. The core consists of many euhedral spinel crystals that are poikilitically enclosed within anorthite,

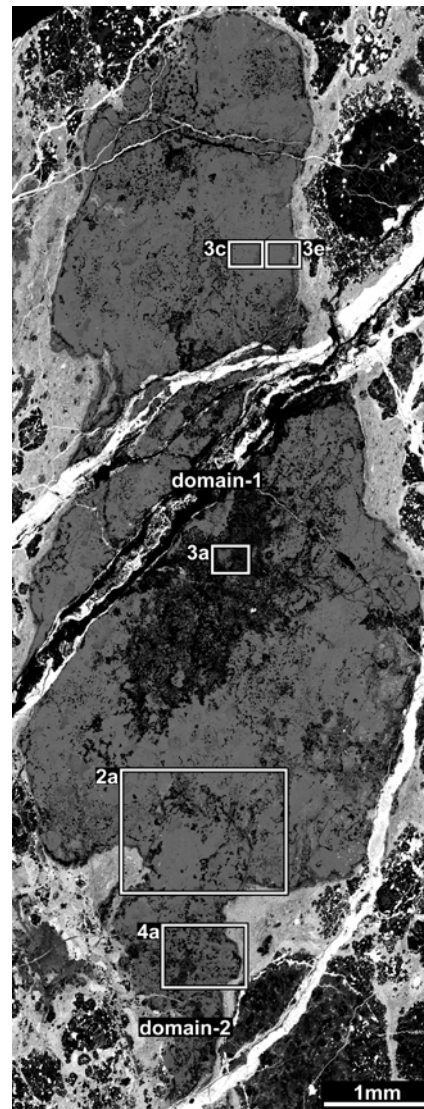


Figure 1. Backscattered electron (BSE) image of a Type A CAI, HKE 01, from Efremovka CV3 chondrite. White boxes numbered 2a, 3a, 3c, 3e and 4a indicate the areas shown in Figs. 2a, 3a, 3c, 3e and 4a, respectively.

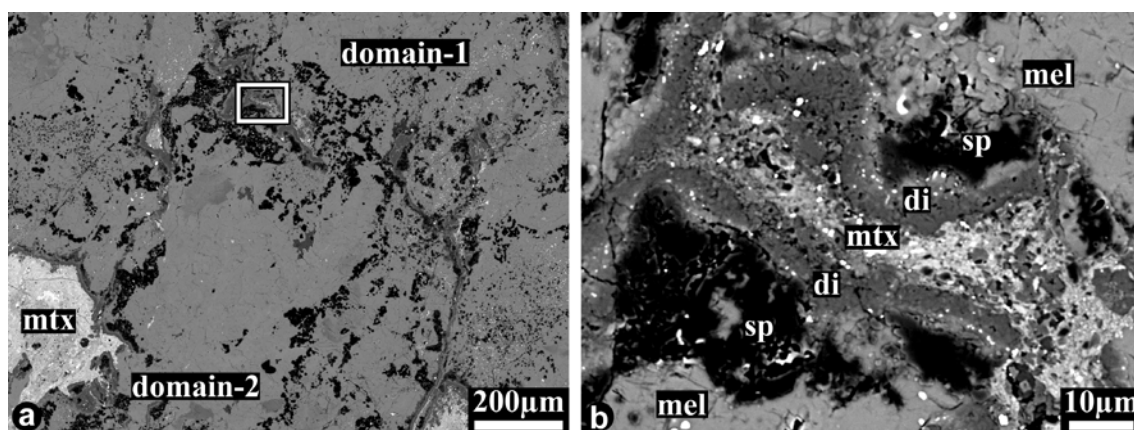


Figure 2. BSE images of the W-L rim that separates the CAI into domains 1 and 2. (a) Region outlined as 2a in Fig. 1. (b) Magnified image of the rectangular area indicated in (a). di, diopside; mel, melilite; mtx, matrix; sp, spinel.

fassaite and melilite (Figs. 3a, 3b). The size of the spinel crystals is less than several tens of micrometers. The mantle consists of mainly melilite (Figs. 3c-3f) with typical grain sizes of several tens of micrometers, and fassaite as the second most abundant phase. Spinel is not abundant in the mantle. The mantle is subdivided into inner and outer mantles according to the melilite composition. The boundary of the inner and outer mantles locates  $\sim 50 \mu\text{m}$  in depth from the W-L rim (Fig. 3g). The chemical compositions of the melilite are åkermanite-rich ( $\text{\AA}k_{30-60}$ ) in the inner mantle and åkermanite-poor ( $\text{\AA}k_{15-30}$ ) in the outer mantle. Each åkermanite-poor crystal of the outer mantle exhibits reverse zoning in the composition (Fig. 3h). The reverse zoning is typically  $\text{\AA}k_{30}$  in the center of the crystal and  $\text{\AA}k_{15}$  at the grain boundary. Melilite with  $\text{\AA}k_{10}$  rarely appears at the grain boundary.

Melilite crystals of the inner mantle exhibit complex zoning, alternated as normal zoning, reverse zoning and then changing to normal zoning again (Fig. 3i), although some melilite crystals exhibit zoning patterns that start as reverse zoning and change to normal zoning. The åkermanite content of the melilite crystals typically changed from  $\text{\AA}k_{30}$  to  $\text{\AA}k_{35}$ ,  $\text{\AA}k_{35}$  to  $\text{\AA}k_{30}$  and  $\text{\AA}k_{30}$  to  $\text{\AA}k_{40}$  from the grain center to the grain boundary. Highly åkermanite-rich ( $\text{\AA}k_{40-60}$ ) melilite was partially observed at the inner mantle. The typical width of the normal zoning part at the grain boundary was  $2 \mu\text{m}$ . The typical grain size of fassaite was several tens to hundreds of micrometers. Fassaite is also present interstitially among åkermanite-rich melilite crystals.

Domain-2 has a core-mantle and W-L rim structure, although the texture of the core-mantle is different to that observed in domain-1 (Figs. 4a, 4b). In the core part, spinel is enclosed by anorthite, melilite and fassaite, but in the core of domain-2 there

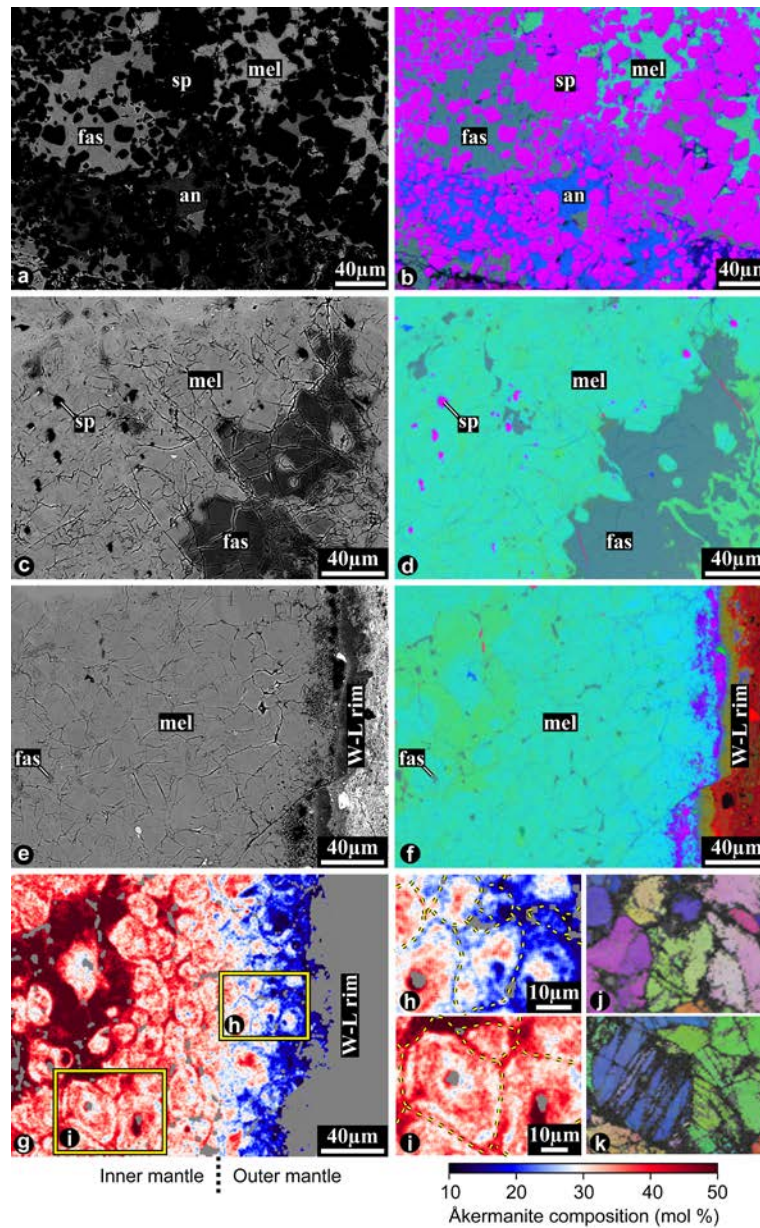


Figure 3. Representative textures of domain-1. (a) BSE image of the core part indicated as 3a in Fig. 1. (b) Combined X-ray elemental map of the area in (a) with Mg (red), Ca (green) and Al (blue). (c) BSE image of the mantle part indicated as 3c in Fig. 1. (d) Combined X-ray elemental map of the area in (c) showing Mg (red), Ca (green) and Al (blue). (e) BSE image of the mantle part indicated as 3e in Fig. 1. (f) Combined X-ray elemental map of the area in (e) showing Mg (red), Ca (green) and Al (blue). (g) X-ray elemental map corresponding to the åkermanite contents of melilite in the region shown in (e). (h) Magnified image of the area indicated as (h) in (g) showing the grain boundaries of melilite crystals. (i) Magnified image of the area indicated as (i) in (g) showing the grain boundaries of melilite crystals. Dashed lines indicate the grain boundaries. (j) EBSD map of the area in (h). (k) EBSD map of the area in (i). an, anorthite; fas, fassaite; mel, melilite; sp, spinel.

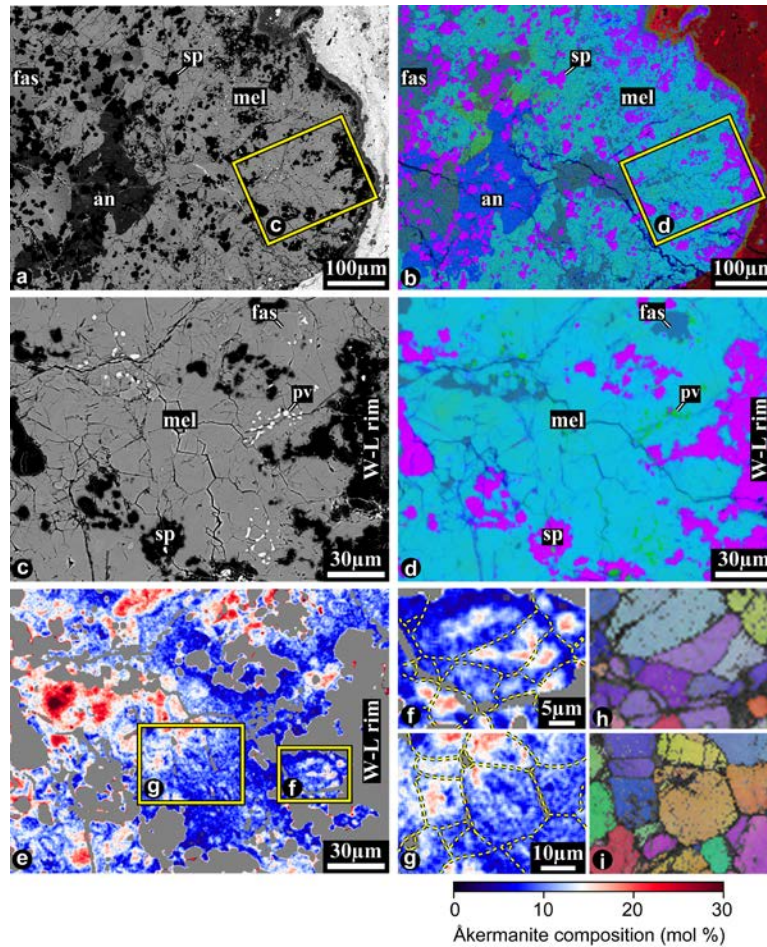


Figure 4. (a) BSE images of domain-2 indicated as 4a in Fig. 1. (b) Combined X-ray elemental map of the area in (a) showing Mg (red), Ca (green) and Al (blue). (c) Representative BSE image of the mantle part area indicated as (c) in (a). (d) Combined X-ray elemental map of the area in (c) showing Mg (red), Ca (green) and Al (blue). (e) X-ray elemental map corresponding to the Åkermanite contents of melilite in the region shown in (c). (f) Magnified image of the area indicated as (f) in (e) showing the grain boundaries of melilite crystals. (g) Magnified image of the area indicated as (g) in (e) showing the grain boundaries of melilite crystals. Dashed lines indicate the grain boundaries. (h) EBSD map of the area in (f). (i) EBSD map of the area in (g). an, anorthite; fas, fassaite; mel, melilite; pv, perovskite; sp, spinel.

are lower amounts of spinel than in the core of domain-1. The mantle part is mainly composed of melilite and contains fassaite, spinel and perovskite (Figs. 4c, 4d). The chemical composition of the melilite crystals are Åk<sub>3-35</sub> (Fig. 4e), which is a narrower range than that for the melilite present in domain-1 (Åk<sub>10-60</sub>). The melilite crystals locate within ~150 µm from the W-L rim exhibit reverse zoning (Figs. 4f, 4g), which is typically Åk<sub>15</sub> in the center and Åk<sub>5</sub> at the grain boundary.

### 3.1.2 Oxygen isotopic compositions of melilite crystals

The oxygen isotopic compositions of melilite crystals in domain-1 and domain-2 were measured (Table 1). Fig. 5 shows the oxygen isotopic compositions plotted on a three oxygen isotope diagram. The spatial distribution of oxygen isotopic compositions in the CAI is shown in Fig. 6.

The oxygen isotopic compositions of melilite crystals in domain-1 are distributed homogeneously at  $\delta^{18}\text{O} = 5\text{-}10\text{‰}$ , despite the different chemical compositions and complex growth zoning patterns observed from the CAI interior to the W-L rim (Fig. 3g). In contrast, the oxygen isotopic compositions of the melilite crystals in domain-2 are distributed along the CCAM line ranging between  $\delta^{18}\text{O} = -40$  and  $0\text{‰}$  (Fig. 5). The melilite crystals positioned near the W-L rim are  $^{16}\text{O}$ -rich ( $\delta^{18}\text{O} = -40\text{‰}$ ), while the melilite becomes  $^{16}\text{O}$ -poor ( $\delta^{18}\text{O} = 0\text{‰}$ ) with increasing distance from the W-L rim (Fig. 6).

The relationship between the oxygen isotopic compositions and åkermanite contents of the melilite crystals in domain-1 and domain-2 is shown in Fig. 7. The oxygen isotopic composition of melilite in domain-1 is distributed homogeneously, despite the wide range of chemical composition from  $\text{Åk}_{17}$  to  $\text{Åk}_{54}$ . In contrast, the oxygen isotopic compositions of melilite crystals in domain-2 are heterogeneously distributed between  $\Delta^{17}\text{O} = -21$  and  $-4\text{‰}$  within a relatively smaller range of the åkermanite content ( $\text{Åk}_6$  to  $\text{Åk}_{22}$ ) and åkermanite poor compositions than those of domain-1. The oxygen isotopic composition of domain-2 tends to become  $^{16}\text{O}$ -rich with decreasing åkermanite content.

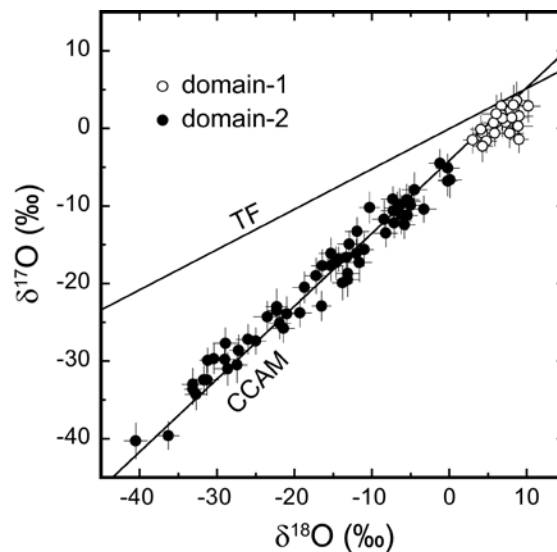


Figure 5. Oxygen isotopic compositions of the melilite crystals in domain-1 and domain-2. Errors are  $2\sigma$ .

Table 1. Oxygen isotopic compositions and åkermanite contents (Åk) of melilite crystals. Each entry number corresponds to the spot numbers in Fig. 6.

Spot	$\delta^{17}\text{O}$	$2\sigma$	$\delta^{18}\text{O}$	$2\sigma$	$\Delta^{17}\text{O}$	$2\sigma$	Åk	Spot	$\delta^{17}\text{O}$	$2\sigma$	$\delta^{18}\text{O}$	$2\sigma$	$\Delta^{17}\text{O}$	$2\sigma$	Åk
Domain-1															
1	0.3	2.1	8.9	1.9	-4.3	2.1	18	20	-17.7	2.0	-15.3	1.6	-9.7	1.7	12
2	-0.6	1.5	4.3	1.2	-2.8	1.6	31	21	-23.8	1.8	-19.3	1.5	-13.8	2.0	8
3	-0.6	1.9	7.8	1.8	-4.7	1.9	21	22	-16.1	1.8	-12.0	1.4	-9.9	1.7	11
4	-0.6	1.7	5.9	1.2	-3.7	1.8	50	23	-25.8	1.8	-21.4	1.4	-14.6	1.6	10
5	2.9	1.7	6.7	1.1	-0.6	1.7	17	24	-20.5	2.0	-18.7	1.5	-10.7	2.0	9
6	0.7	1.9	6.0	1.0	-2.4	1.8	27	25	-24.3	2.0	-23.5	1.8	-12.1	1.9	6
7	0.8	1.6	7.3	1.3	-3.0	1.8	24	26	-9.1	1.6	-7.3	1.5	-5.3	1.5	13
8	-1.4	1.7	9.0	1.2	-6.1	1.8	20	27	-29.9	1.6	-31.2	1.0	-13.7	1.5	9
9	-1.6	1.5	4.8	1.3	-4.1	1.7	37	28	-16.1	2.0	-15.3	1.5	-8.1	2.0	11
10	1.7	1.9	6.8	1.2	-1.9	2.0	17	29	-9.2	2.0	-5.5	1.6	-6.3	2.0	12
11	0.7	1.7	5.7	1.2	-2.2	1.6	18	30	-17.3	2.5	-11.6	1.6	-11.3	2.4	10
12	-0.1	1.8	4.1	1.4	-2.3	1.7	43	31	-27.7	2.0	-28.9	1.6	-12.6	2.2	7
13	-2.3	2.0	4.3	1.3	-4.5	2.0	36	32	-32.4	2.0	-31.3	1.2	-16.1	1.9	8
14	-1.5	1.7	3.0	1.2	-3.1	1.7	35	33	-28.6	2.0	-27.2	1.2	-14.5	1.8	6
15	2.9	2.1	10.2	1.5	-2.3	2.4	32	34	-19.9	2.2	-13.8	1.3	-12.6	2.1	19
16	1.3	2.4	6.9	1.5	-2.3	2.5	35	35	-10.4	1.7	-3.3	1.6	-8.6	1.7	15
17	3.6	2.4	8.7	1.5	-1.0	2.4	33	36	-10.0	2.3	-6.4	1.4	-6.7	2.2	9
18	1.6	2.4	9.0	1.8	-3.0	2.8	54	37	-22.9	1.9	-16.5	1.2	-14.3	1.8	11
19	3.0	2.6	8.3	2.0	-1.3	2.6	33	38	-23.9	2.2	-21.0	1.3	-12.9	2.0	11
20	1.9	2.4	6.1	1.9	-1.3	2.7	18	39	-18.7	2.3	-13.1	1.5	-11.9	2.0	15
21	1.4	2.0	8.1	2.0	-2.8	2.0	22	40	-7.9	2.2	-4.5	1.6	-5.6	1.9	14
Domain-2								41	-15.6	2.2	-11.0	1.2	-9.9	1.9	11
1	-29.8	2.0	-29.0	1.7	-14.8	2.0	9	42	-31.0	2.1	-28.6	1.7	-16.1	1.6	10
2	-34.3	2.0	-32.7	1.4	-17.2	2.0	9	43	-17.3	2.0	-14.6	1.3	-9.7	2.2	10
3	-40.3	2.3	-40.5	1.5	-19.2	2.2	7	44	-19.5	2.2	-13.1	1.5	-12.6	2.5	11
4	-32.4	1.8	-31.7	1.9	-15.9	1.7	13	45	-10.2	2.0	-10.3	1.3	-4.9	2.0	8
5	-33.0	2.1	-33.1	1.4	-15.8	1.9	13	46	-17.7	2.1	-16.4	1.4	-9.2	2.2	7
6	-29.7	1.9	-30.4	1.6	-13.9	1.7	9	47	-9.4	2.0	-5.2	1.5	-6.8	2.4	6
7	-33.6	2.0	-33.1	1.1	-16.4	1.8	11	48	-12.2	1.9	-7.1	1.4	-8.5	2.1	13
8	-39.6	1.8	-36.3	1.4	-20.8	1.7	6	49	-13.3	1.8	-11.9	1.5	-7.0	2.0	9
9	-9.9	2.1	-5.0	1.5	-7.3	1.8	12	50	-14.9	1.7	-12.9	1.5	-8.2	2.0	11
10	-6.6	2.3	0.1	1.5	-6.6	2.1	16	51	-16.9	1.6	-14.3	1.5	-9.5	2.1	9
11	-4.5	1.8	-1.2	1.4	-3.9	1.6	12	52	-23.5	2.1	-22.3	1.1	-11.9	2.3	10
12	-12.4	1.8	-5.8	1.4	-9.4	1.6	15	53	-27.4	1.7	-25.0	1.3	-14.4	1.9	9
13	-10.6	1.9	-7.2	1.6	-6.9	1.8	21	54	-25.1	2.0	-21.9	1.4	-13.7	2.4	11
14	-10.3	2.1	-6.7	1.7	-6.8	2.0	16	55	-27.2	1.9	-26.0	1.5	-13.7	2.0	9
15	-11.2	1.8	-5.4	1.3	-8.4	1.7	22	56	-30.5	2.3	-27.4	1.3	-16.3	2.5	7
16	-11.1	2.5	-6.2	1.2	-7.9	2.3	12	57	-13.5	1.8	-8.2	1.5	-9.2	2.1	17
17	-11.2	1.9	-5.5	1.4	-8.3	1.9	12	58	-6.8	1.9	-0.2	1.2	-6.7	2.0	18
18	-16.6	1.6	-13.3	1.6	-9.6	1.3	12	59	-5.1	1.8	-0.2	1.5	-5.0	2.0	18
19	-11.7	2.4	-8.4	1.5	-7.3	2.4	13	60	-19.0	2.3	-17.2	1.4	-10.0	2.5	8
								61	-23.0	2.3	-22.3	1.4	-11.4	2.3	7

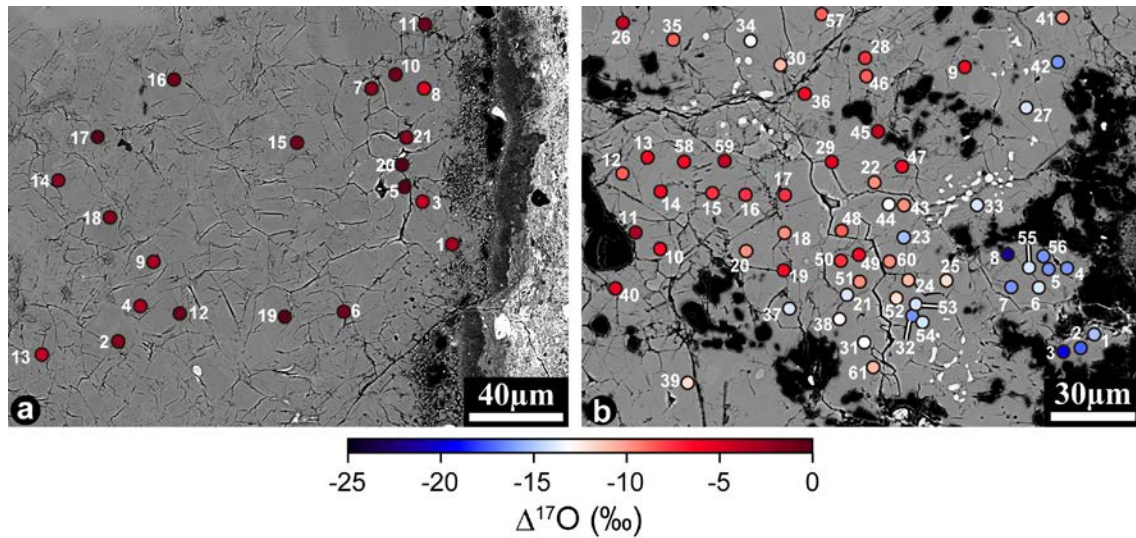


Figure 6. Measurement positions and oxygen isotopic compositions plotted on BSE images of the regions shown in Figs. 3e and 4c. The spot numbers of each plot correspond to the entries listed in Table 1. The symbol colors correspond to the oxygen isotopic composition scale.

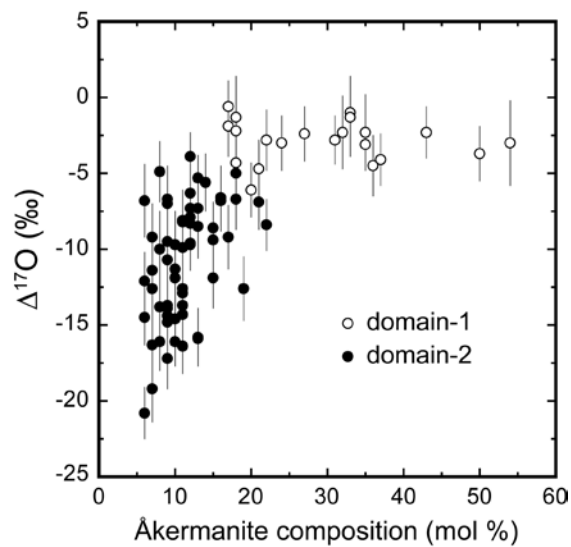


Figure 7. Relationship between the oxygen isotopic compositions and chemical compositions of melilite crystals in domain-1 and domain-2. Error bars are  $2\sigma$ . The chemical compositions of melilite crystals are obtained from X-ray quantitative maps.

## 3.2 Discussion

### 3.2.1 Oxygen isotopic compositions and chemical zoning of melilite crystals in domain-1

The melilite crystals in domain-1 have complex chemical growth zoning patterns (Fig. 3). The melilite crystals positioned shallower than  $\sim 50 \mu\text{m}$  from the W-L rim (outer mantle) exhibit reverse zoning (Fig. 3h). Reversely zoned melilite crystals found in fluffy Type A CAIs are explained by condensation from a solar nebular gas during a period of decreasing pressure (MacPherson and Grossman 1984) or by crystallization from incomplete melting with melt evaporation (Grossman et al. 2002). Significant mass dependent isotope fractionation is predicted for the melt evaporation origin for the reverse zoning. However, mass dependent fractionation of oxygen isotopes is not clear (Fig. 5) and it supports a condensation origin for the reverse zoning.

On the other hand, the åkermanite-rich melilite crystals in the inner mantle show oscillatory zoning, where the crystals are initially grown with normal zoning, change to reverse zoning, and then change to normal zoning (Fig. 3i). The oscillatory zoned melilite crystals could be formed by direct condensation in a solar nebular gas with decreasing temperature under variable pressure change. In this case, the formation processes could be described using the melilite condensation diagram by Yoneda and Grossman (1995) (Fig. 8) as follows: (1) melilite is formed by condensation from a gas with decreasing temperature under a constant or decreasing pressure to form normal zoning. (2) The pressure is decreased enough to form reverse zoning. (3) The temperature decrease continues to form normal zoning. After condensation of individual

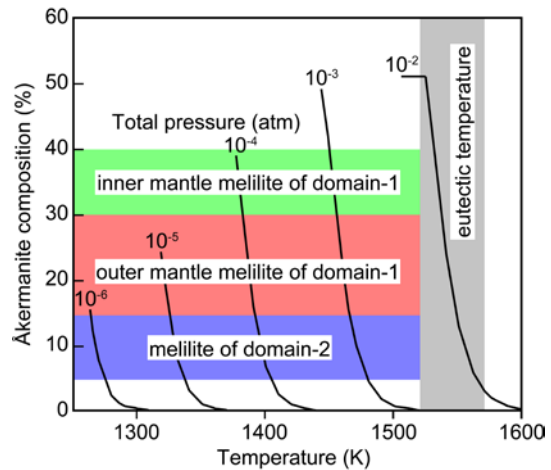


Figure 8. Relationship between the melilite composition, condensation temperature and pressure in domain-1 and domain-2. The equilibrium condensation diagram is from Yoneda and Grossman (1995). The eutectic melting temperature of melilite and fassaite is from Stolper (1982) and Onuma and Moridaira (1991) and is indicated by the gray area.

melilite crystals with oscillatory zoning, the melilite crystals accumulate to form the inner mantle.

Åkermanite-poor reversely zoned melilite crystals are observed in the outer mantle of domain-1. Therefore, if the outer mantle melilite grew following the condensation of oscillatory zoned melilite crystals in the inner mantle, then the inner mantle melilite should form åkermanite-poor reverse zoning at the most outer edge. Furthermore, if the outer zoned melilite crystals condense before the end of the oscillatory zoned melilite crystal accumulation, then the reversely zoned melilite crystals should be incorporated among the oscillatory zoned melilite crystals. The åkermanite-poor reversely zoned melilite crystals observed in the outer mantle are not observed in the inner mantle; therefore, the melilite crystals in the outer mantle must be formed after the end of the inner mantle formation and accumulation onto the inner mantle.

In the mantle, melilite and fassaite coexist (Figs. 3c-3f). The mantle melilite has never largely molten because the inner mantle melilite preserves the oscillatory growth zoning pattern and the outer mantle melilite preserves the reverse zoning pattern. Therefore, the mantle melilite was condensed below the eutectic melting temperature of melilite and fassaite. The eutectic temperature has been experimentally determined as 1520 K (Stolper 1982) or 1568 K (Onuma and Moridaira 1991); therefore, the melilite crystals in domain-1 were condensed below 1520-1568 K and at pressures lower than  $10^{-2}$  atm (Fig. 8).

The chemical zoning of the inner mantle melilite ranges from Åk<sub>30</sub> to Åk<sub>60</sub> (typically from Åk<sub>30</sub> to Åk<sub>40</sub>). Therefore, the condensation conditions for the formation of the inner mantle melilite are within the green area shown in Fig. 8. On the other hand, the reverse zoning of melilite crystals in the outer mantle was typically Åk<sub>30</sub> in the center and Åk<sub>15</sub> at the grain boundary, and thus, condensation would occur under the conditions indicated by the red area shown in Fig. 8. If the condensation temperature was constant or decreased during crystallization of the inner and outer mantle melilite, then the condensation pressure was lower during outer mantle melilite crystallization than that during inner mantle melilite crystallization.

The melilite crystals in domain-1 inherited the oxygen isotopic compositions from the solar nebular gas according to the condensation origin. Therefore, the homogeneous <sup>16</sup>O-poor composition ( $\delta^{18}\text{O} = 5\text{-}10\%$ ) of melilite in domain-1 (Fig. 5) indicates that the oxygen isotopic composition of the nebular gas was maintained at a <sup>16</sup>O-poor state during the formation of melilite in the inner mantle and outer mantle.

### 3.2.2 Oxygen isotopic compositions and chemical zoning of melilite crystals in domain-2

The melilite crystals positioned shallower than  $\sim 150 \mu\text{m}$  from the W-L rim in domain-2 exhibit reverse zoning (Fig. 4). These reversely zoned melilite crystals could have crystallized by direct condensation from solar nebular gas with decreasing pressure and then accumulate onto the CAI, similar to the process discussed in the previous section.

The melilite in domain-2 was condensed below the eutectic temperature of melilite and fassaite for the same reason as that discussed for domain-1 (i.e., they are zoned). These crystals were condensed under the conditions indicated by the blue area shown in Fig. 8. The reversely zoned melilite in domain-2 could condense under a pressure 1.5-2 times lower than the condensation pressure of the outer mantle melilite of domain-1 if the condensation temperature was the same. For example, if the temperature was 1400 K, then the pressure was changed from  $3.2 \times 10^{-4}$  to  $2.2 \times 10^{-4}$  atm for the formation of the outer mantle of domain-1, and from  $2.2 \times 10^{-4}$  to  $9.7 \times 10^{-5}$  atm for that of domain-2.

The oxygen isotopic compositions of the melilite crystals in domain-2 are heterogeneously distributed along the CCAM line ranging between  $\delta^{18}\text{O} = -40$  and  $0\%$  (Fig. 5). The oxygen isotopic compositions of the reversely zoned melilite crystals tend to change from  $^{16}\text{O}$ -poor ( $\delta^{18}\text{O} = 0\%$ ) at the CAI interior to  $^{16}\text{O}$ -rich ( $\delta^{18}\text{O} = -40\%$ ) near the W-L rim (Fig. 6). The width of the heterogeneous oxygen isotope layer is approximately  $100 \mu\text{m}$  of the mantle. The distinct oxygen isotopic compositions between melilite of both domains show that they were formed at distinct nebular environments.

The oxygen isotopic variation of melilite from the CAI interior to the W-L rim has been observed in a compact Type A CAI (Simon et al. 2011), which was interpreted as high temperature gas-solid diffusion in the solar nebula after the CAI formation. In their study, the oxygen isotopic compositions of melilite changed within a range of about  $75 \mu\text{m}$  from  $^{16}\text{O}$ -rich at the CAI interior to  $^{16}\text{O}$ -poor near the W-L rim, which is opposite to the trend determined in this study.

The oxygen isotopic variation from  $^{16}\text{O}$ -poor at the CAI interior to  $^{16}\text{O}$ -rich near the W-L rim determine in this study is not monotonic as described by Simon et al. (2011).  $^{16}\text{O}$ -poor and  $^{16}\text{O}$ -rich melilites are often mixed in the CAI interior in this study. For example, spots 30 and 34 in Fig. 6b are more  $^{16}\text{O}$ -rich than spots 28, 36 and 46.

Therefore, the oxygen isotopic variation in domain-2 cannot simply be discussed according to gas-solid diffusion with  $^{16}\text{O}$ -rich gas of the solar nebula after CAI solidification. This oxygen variation pattern also cannot simply be achieved by parent body processes because oxygen isotopic compositions around the CAI are  $^{16}\text{O}$ -rich. The oxygen isotopic variation observed in domain-2 is described as reversely zoned melilite crystals condensed from gas where the oxygen isotopic composition gradually changed towards  $^{16}\text{O}$ -rich during formation of the mantle layer.

Domain-2 appears to have formed by the accumulation of single melilite crystals that condensed separately. Therefore, the melilite crystals at the CAI interior are older than those near the W-L rim. The general oxygen isotopic variation of the melilite crystals from the CAI interior to the W-L rim indicates that the oxygen isotopic composition of the solar nebula gas from which the melilite crystals were condensed was changed from  $^{16}\text{O}$ -poor to  $^{16}\text{O}$ -rich. Some irregularity of the general oxygen isotopic variation observed may be due to the fluffy nature of the CAI caused by the accumulation process. The chemical and oxygen isotopic distribution of the melilite indicates that the oxygen isotopic composition of the nebular gas around the CAI was temporally changed from  $^{16}\text{O}$ -poor to  $^{16}\text{O}$ -rich with decreasing pressure, or the CAI was transported towards  $^{16}\text{O}$ -richer and lower pressure regions of the solar nebula.

### **3.2.3 Formation sequence of HKE 01**

The reversely zoned melilite crystals in the outer mantle of domain-1 and mantle of domain-2 condensed from solar nebular gas with decreasing pressure and accreted together to form the separate CAI domain. However, the melilite crystals in domain-1 and domain-2 were formed independently from different oxygen isotopic and chemical compositions (Fig. 9). Melilite of domain-1 was condensed in an  $^{16}\text{O}$ -poor nebular environment and accumulated on the core. The environment changed, firstly with decreasing temperature and then with decreasing pressure. These changes may correspond to the heliocentric and vertical motion of the CAI.

On the other hand, the melilite of domain-2 was condensed on the core in a nebular environment with variable oxygen isotopic composition. The environment changed from  $^{16}\text{O}$ -poor to  $^{16}\text{O}$ -rich with decreasing pressure. The environmental changes resemble those for the formation of a fluffy Type A CAI from Vigarano chondrite (Katayama et al. 2012). This situation may correspond to the inner edge region of the solar nebula where  $^{16}\text{O}$ -rich solar and  $^{16}\text{O}$ -poor planetary gases are encountered and mixed (Yurimoto et al. 2008). The environmental changes around domain-2 were occurred by the fluctuation of the inner edge of the solar nebula

(Yurimoto et al. 2008) or the radial transportation of grains (Ciesla 2007; 2009).

After the formation of domain-1 and -2, the domains aggregated to form HKE 01. HKE 01 is a compound object like several CAIs previously described (e.g., Kim et al. 2002; Aléon et al. 2005). The W-L rims surrounding the domains would be formed in the environment where the domains encountered each other.

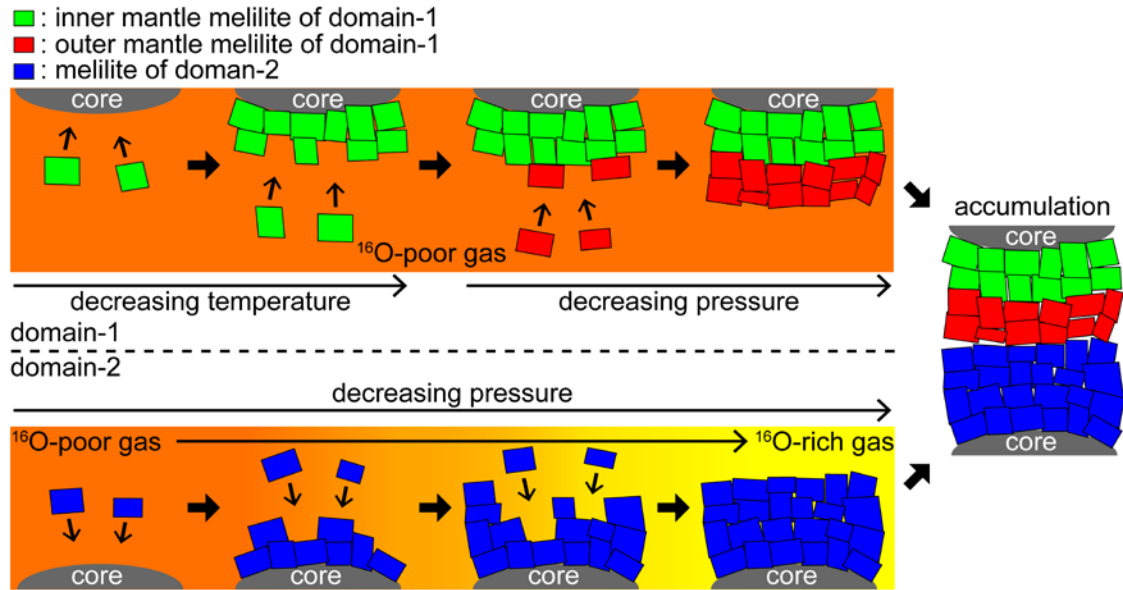


Figure 9. Schematic scenario of melilite formation in domain-1 and domain-2. The inner mantle melilite of domain-1 condensed from  $^{16}\text{O}$ -poor gas with decreasing temperature and accreted onto the core. The reversely zoned melilite then condensed from the gas with decreasing pressure and accreted on the inner mantle. The oxygen isotopic compositions of the gas was always  $^{16}\text{O}$ -poor. The reversely zoned melilite of domain-2 condensed from  $^{16}\text{O}$ -poor gas with decreasing pressure. The environment where domain-2 was formed is different from that where domain-1 was formed, because the oxygen isotopic composition of the nebular gas surrounding domain-2 was varied from  $^{16}\text{O}$ -poor to  $^{16}\text{O}$ -rich. Domain-1 and -2 were aggregated together to form the entire CAI, HKE 01.

### 3.3 CONCLUSIONS

We have measured the oxygen isotopic and chemical compositions of melilite crystals in the Type A CAI, HKE 01, from Efremovka CV3 chondrite. The W-L rim divides the CAI into two domains, denoted domain-1 and domain-2. Both domains show a core-mantle structure and are surrounded by the Wark-Lovering rims. The mantle parts of each domain were mainly composed of melilite.

The mantle part of domain-1 was subdivided into inner and outer mantles

according to the melilite composition. The chemical compositions of the melilite are åkermanite-rich (typically Åk<sub>30-40</sub>) in the inner mantle and åkermanite-poor (typically Åk<sub>15-30</sub>) in the outer mantle. Each åkermanite-poor crystal of the outer mantle exhibits reverse zoning in the composition. On the other hand, the melilite crystals of the inner mantle exhibit complex zoning, initially started as normal zoning that changes to reverse zoning and then changes to normal zoning. Melilite crystals in the mantle part of domain-2 exhibit reverse zoning. The chemical compositions of these crystals typically ranged from Åk<sub>5-15</sub>.

The oxygen isotopic compositions of the melilite crystals in domain-1 are homogeneously distributed at  $\delta^{18}\text{O} = 5\text{-}10\text{‰}$  on the CCAM line, despite the differences in the chemical compositions and complex growth zoning patterns. In contrast, the oxygen isotopic compositions of the melilite crystals in domain-2 are distributed along the CCAM line ranging between  $\delta^{18}\text{O} = -40$  and  $0\text{‰}$ . The melilite crystals positioned near the W-L rim are  $^{16}\text{O}$ -rich ( $\delta^{18}\text{O} = -40\text{‰}$ ) and the melilite crystals become  $^{16}\text{O}$ -poor ( $\delta^{18}\text{O} = 0\text{‰}$ ) with increasing distance from the W-L rim.

The reversely zoned melilite crystals in the outer mantle of domain-1 and domain-2 could be crystallized by direct condensation from solar nebular gas during a period of decreasing pressure. However, the reversely zoned melilite crystals in each domain were formed independently, because they have different oxygen isotopic and chemical compositions. The oscillatory zoned melilite crystals in the inner mantle of domain-1 could be formed by direct condensation from the solar nebular gas with decreasing temperature under variable pressure change.

The melilite crystals in the mantle part of each domain inherited the oxygen isotopic compositions from the solar nebular gas because of the condensation origin. The homogeneous  $^{16}\text{O}$ -poor composition of melilite in domain-1 indicates that the oxygen isotopic composition of the nebular gas was maintained at the  $^{16}\text{O}$ -poor condition during the formation of melilite in the inner and outer mantles. The environment was firstly changed with decreasing temperature and then with decreasing pressure while the domain was formed in an oxygen isotopic reservoir of the solar nebula. The changes of temperature and pressure may correspond to the heliocentric and vertical motion of the CAI.

On the other hand, the oxygen isotopic variation of the reversely zoned melilite crystals in domain-2 indicates that the domain was formed in a variable oxygen isotopic reservoir of the solar nebula, and the oxygen isotopic composition of the region of solar nebular gas from which the melilite condensed was changed from  $^{16}\text{O}$ -poor to  $^{16}\text{O}$ -rich. The environment changed from  $^{16}\text{O}$ -poor to  $^{16}\text{O}$ -rich with decreasing pressure. This

situation may correspond to the inner edge region of the solar nebular where  $^{16}\text{O}$ -rich solar and  $^{16}\text{O}$ -poor planetary gases are encountered and mixed (Yurimoto et al. 2008) or radial transport of the grains (Ciesla 2007; 2009). After the formation of each domain, the domains aggregated to form HKE 01.

## 4. $^{26}\text{Al}$ -Mg chronology and oxygen isotope distributions of multiple melting for a Type C CAI from Allende CV3

### 4.1 RESULTS

#### 4.1.1 Mineralogy and Petrology

EK1-04-2 is a CAI fragment picked out from Allende CV3 with an approximate diameter of 2 mm. Figure 1 shows a BSE image and an elemental map of the CAI. The CAI is composed of spinel, anorthite, olivine, and pyroxene. Small amounts of nepheline, sodalite, and Fe-rich augite are present as secondary alteration minerals. The CAI appears to have a core-mantle structure according to the abundances and chemical compositions of the constituent minerals, although the boundary is not clearly apparent. The core consists of 42% anorthite, 32% spinel, 17% Ti-Al-diopside (0.3-7.5 wt%  $\text{TiO}_2$ ; 8.1-20.6 wt%  $\text{Al}_2\text{O}_3$ ) and 9% of olivine, while the mantle consists of 57% anorthite, 39% Ti-Al-bearing augite (0.5-3.4 wt%  $\text{TiO}_2$ ; 0.2-11.9 wt%  $\text{Al}_2\text{O}_3$ ), 3% olivine, and 1% spinel. The spinel in the core has a representative FeO content of 0.5 wt%, although the spinels throughout both the core and mantle of the CAI have variable FeO contents (0.4-10.7 wt% FeO). Melilite is not observed in EK1-04-2 and the abundance of olivine is much higher than that in a typical Type C CAI. The chemical compositions of pyroxene in the CAI have bimodal distributions, as shown by the different peaks of the

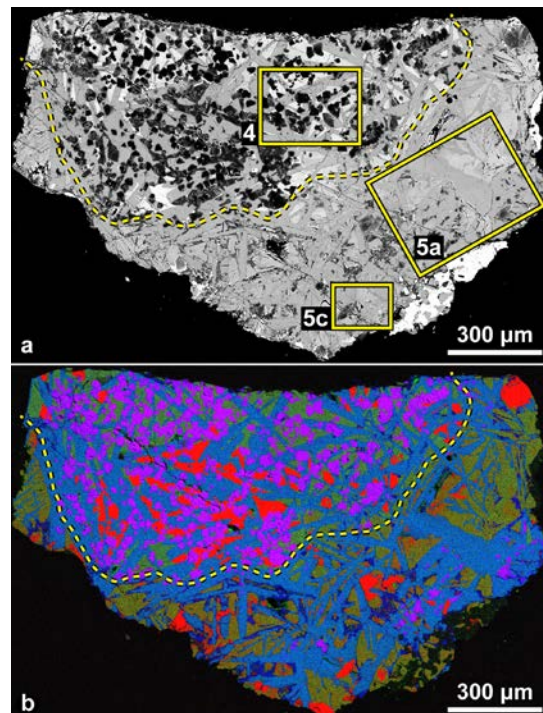


Figure 1. (a) Backscattered electron (BSE) image of a Type C CAI, EK1-04-2, from the Allende CV3 chondrite. Yellow boxes numbered 4, 5a and 5c indicate the areas shown in Figs. 4, 5a, and 5c, respectively. (b) Combined X-ray elemental map of EK1-04-2 with Mg (red), Ca (green), and Al (blue). Dashed lines indicate an outline of the boundary between the core and mantle.

histograms for the  $Al/^{24}Mg$  ratio and  $TiO_2$  contents for pyroxene in the core and mantle (Fig. 2); pyroxene in the core is enriched in Al and Ti, while that in the mantle is enriched in Mg. Representative analyses of the chemical compositions of the minerals are shown in Table 1.

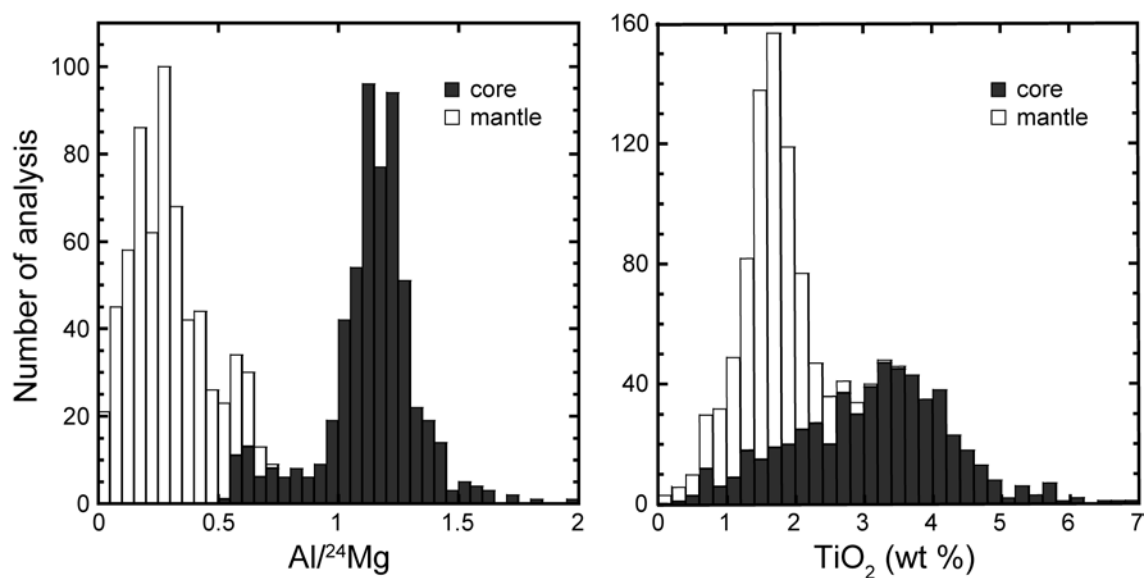


Figure 2. Histograms of  $Al/^{24}Mg$  ratio and  $TiO_2$  content (wt %) for pyroxene from the core and mantle.

Table 1. Representative compositions of minerals in EK1-04-2.

core	An	An	Px	Px	Ol	Ol	Sp	Sp
Na <sub>2</sub> O	0.2	0.2	n.d.	n.d.	n.d.	n.d.	n.d.	n.d.
MgO	0.2	n.d.	12.2	11.0	55.7	55.8	27.9	27.0
Al <sub>2</sub> O <sub>3</sub>	36.2	36.2	15.6	17.9	n.d.	n.d.	70.1	70.5
SiO <sub>2</sub>	43.4	43.3	43.3	43.4	42.7	42.9	n.d.	n.d.
CaO	20.1	20.3	25.3	25.8	0.8	0.8	n.d.	n.d.
TiO <sub>2</sub>	n.d.	n.d.	3.2	1.0	n.d.	n.d.	0.4	0.3
V <sub>2</sub> O <sub>5</sub>	n.d.	n.d.	n.d.	n.d.	n.d.	n.d.	1.0	0.9
Cr <sub>2</sub> O <sub>3</sub>	n.d.	n.d.	0.3	0.3	n.d.	n.d.	n.d.	n.d.
FeO	n.d.	n.d.	0.3	0.3	1.2	0.9	0.4	1.7
Total	100.1	99.9	100.2	99.7	100.4	100.4	99.8	100.4
Cations								
Na	0.02	0.02	n.d.	n.d.	n.d.	n.d.	n.d.	n.d.
Mg	0.01	n.d.	0.66	0.60	1.95	1.95	0.99	0.96
Al	1.98	1.97	0.67	0.77	n.d.	n.d.	1.97	1.98
Si	2.01	2.01	1.58	1.58	1.00	1.01	n.d.	n.d.
Ca	1.00	1.01	0.99	1.01	0.02	0.02	n.d.	n.d.
Ti	n.d.	n.d.	0.09	0.03	n.d.	n.d.	0.01	0.01
V	n.d.	n.d.	n.d.	n.d.	n.d.	n.d.	0.02	0.01
Cr	n.d.	n.d.	0.01	0.01	n.d.	n.d.	n.d.	n.d.
Fe	n.d.	n.d.	0.01	0.01	0.02	0.02	0.01	0.03
Total	5.01	5.01	4.00	4.00	3.00	2.99	2.99	2.99
per oxygen	8	8	6	6	4	4	4	4
mantle								
Na <sub>2</sub> O	0.2	0.3	n.d.	n.d.	n.d.	n.d.	n.d.	n.d.
MgO	n.d.	0.2	18.4	19.6	55.5	53.4	26.1	24.0
Al <sub>2</sub> O <sub>3</sub>	36.4	36.2	5.2	4.6	n.d.	n.d.	69.5	68.2
SiO <sub>2</sub>	43.6	43.7	52.1	53.0	42.8	42.0	n.d.	n.d.
CaO	20.2	20.1	21.9	20.9	0.6	0.7	0.2	0.2
TiO <sub>2</sub>	n.d.	n.d.	2.0	1.5	n.d.	n.d.	0.3	0.4
V <sub>2</sub> O <sub>5</sub>	n.d.	n.d.	n.d.	n.d.	n.d.	n.d.	0.3	0.6
Cr <sub>2</sub> O <sub>3</sub>	n.d.	n.d.	0.5	0.4	n.d.	n.d.	0.8	0.7
FeO	n.d.	n.d.	0.3	0.4	1.9	4.1	3.3	6.2
Total	100.4	100.4	100.3	100.5	100.8	100.1	100.4	100.3
Cations								
Na	0.02	0.02	n.d.	n.d.	n.d.	n.d.	n.d.	n.d.
Mg	n.d.	0.02	0.98	1.04	1.94	1.90	0.93	0.87
Al	1.98	1.97	0.22	0.19	n.d.	n.d.	1.97	1.96
Si	2.01	2.01	1.86	1.88	1.00	1.00	n.d.	n.d.
Ca	1.00	1.00	0.84	0.80	0.01	0.02	0.01	0.00
Ti	n.d.	n.d.	0.05	0.04	n.d.	n.d.	0.00	0.01
V	n.d.	n.d.	n.d.	n.d.	n.d.	n.d.	0.00	0.01
Cr	n.d.	n.d.	0.01	0.01	n.d.	n.d.	0.02	0.01
Fe	n.d.	n.d.	0.01	0.01	0.04	0.08	0.07	0.13
Total	5.01	5.01	3.97	3.97	3.00	3.00	3.00	2.99
per oxygen	8	8	6	6	4	4	4	4

An: anorthite, Px: pyroxene, Ol: olivine, Sp: spinel, n.d. = not detected

The bulk chemical compositions of the core and mantle in EK1-04-2 (Table 2) are plotted on the cosmochemical phase diagram presented by MacPherson and Huss (2005) (Fig. 3). The spinel coordinates of the core and mantle compositions are  $-65$  and  $-142$ , respectively. The core composition is plotted above the spinel-saturated surface ( $\sim -130$ ) and the crystallization sequences from a melt of the core composition were spinel, anorthite, olivine, and pyroxene, according to the diagram (MacPherson and Huss, 2005). The core has an intermediate chemical composition between Type C CAIs and Al-rich chondrules. The bulk chemical composition of the core is enriched in MgO and depleted in CaO relative to typical Type C CAIs, and is also distinct from the compositions of Al-rich chondrules. However, abundant spinel crystals in the core and their  $^{16}\text{O}$ -rich signatures (as discussed in section 4.1.2) suggest that the core is categorized as a Type C CAI because these are common features of the Type C CAIs (Wark, 1987; Krot et al., 2007, 2008). In contrast, the mantle composition in the diagram is plotted almost on the spinel-saturated surface ( $\sim -140$ ), which is similar to the compositions for Al-rich chondrules (Fig. 3). The bulk chemical composition of the mantle (Table 2) is enriched in  $\text{SiO}_2$  and CaO, and depleted in MgO and  $\text{Al}_2\text{O}_3$  relative to the core.

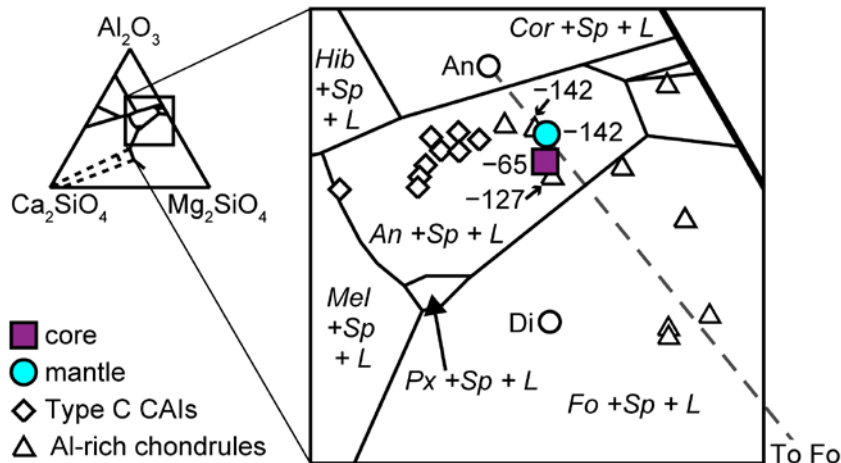


Figure 3. Bulk chemical compositions (wt %) for the core (square) and mantle (circle) of EK1-04-2 projected from spinel ( $\text{Mg}_2\text{AlO}_4$ ) onto the plane of  $\text{Ca}_2\text{SiO}_4$  - forsterite ( $\text{Mg}_2\text{SiO}_4$ ) - corundum ( $\text{Al}_2\text{O}_3$ ) (MacPherson and Huss, 2005). Literature data for the Type C CAIs (Wark, 1987) and Al-rich chondrules (Wark, 1987; MacPherson and Huss, 2005) are plotted for comparison. The numbers denote the spinel coordinates of the core ( $-65$ ), mantle ( $-142$ ), and two Al-rich chondrules ( $-127$  and  $-142$ ) which are plotted near the core and mantle on the projection. The spinel-saturated surface is  $\sim -130$  to  $-140$  at the plots of the core and mantle compositions. An, anorthite; Cor, corundum; Di, diopside; Fo, forsterite; Hib, hibonite; Mel, melilite; Px, pyroxene, Sp, spinel.

Table 2. Bulk chemical compositions of the core and mantle of EK1-04-2.

area	Na <sub>2</sub> O (wt %)	MgO	Al <sub>2</sub> O <sub>3</sub>	SiO <sub>2</sub>	S	Cl	CaO	TiO <sub>2</sub>	V <sub>2</sub> O <sub>5</sub>	Cr <sub>2</sub> O <sub>3</sub>	FeO
core	0.4	15.7	37.4	31.8	n.d.	n.d.	12.6	0.6	0.2	0.3	1.0
mantle	1.9	9.0	25.3	44.2	0.3	0.2	16.8	0.6	n.d.	0.3	2.0

n.d. = not detected

Figure 4 shows representative textures of the core. Euhedral spinel crystals are enclosed by other mineral crystals. The size of the spinel crystals is less than several tens of micrometers. Anorthite is the most abundant mineral in the core, with euhedral or subhedral shapes that often enclose spinel crystals. Olivine crystals have subhedral or anhedral shapes and are enclosed by pyroxene crystals. Pyroxene crystals are anhedral shaped and also enclose spinel and olivine crystals. These textural relationships indicate that the crystallization sequence of the core minerals is spinel, anorthite, olivine, and pyroxene, which is consistent with that expected from the chemical composition and the phase equilibrium of the core.

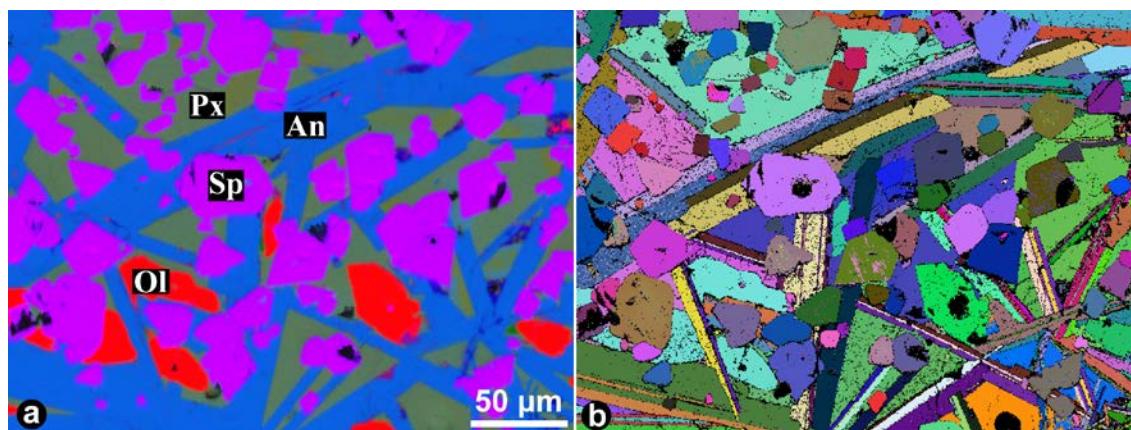


Figure 4. Representative textures of the EK1-04-2 core. (a) Combined X-ray elemental map of the area indicated as area 4 in Fig. 1, showing Mg (red), Ca (green), and Al (blue). (b) EBSD Euler map of the area in (a). An, anorthite; Px, pyroxene; Ol, olivine; Sp, spinel.

Figure 5 shows representative textures of the mantle, in which the amounts of spinel and olivine are smaller than those in the core, while those of anorthite and pyroxene are larger. Spinel crystals have subhedral or anhedral shapes and are enclosed by anorthite crystals. Anorthite crystals are euhedral or subhedral shaped and in contact with subhedral or anhedral olivine crystals and anhedral pyroxene crystals. The size of anorthite crystals in the mantle is larger than that in the core. The amount of euhedral anorthite crystals is lower in the mantle than in the core, and most of the anorthite

crystals have subhedral shapes. Olivine crystals have subhedral or anhedral shapes and are enclosed by pyroxene or observed among anorthite crystals, which indicates that the crystallization of olivine was earlier than that of pyroxene. These textural relationships are similar to the core, except for the subhedral or anhedral shapes of spinel crystals and the larger amount of subhedral anorthite crystals. These mantle textures appear to correspond to partial melting from outside of the CAI and subsequent recrystallization of the melt.

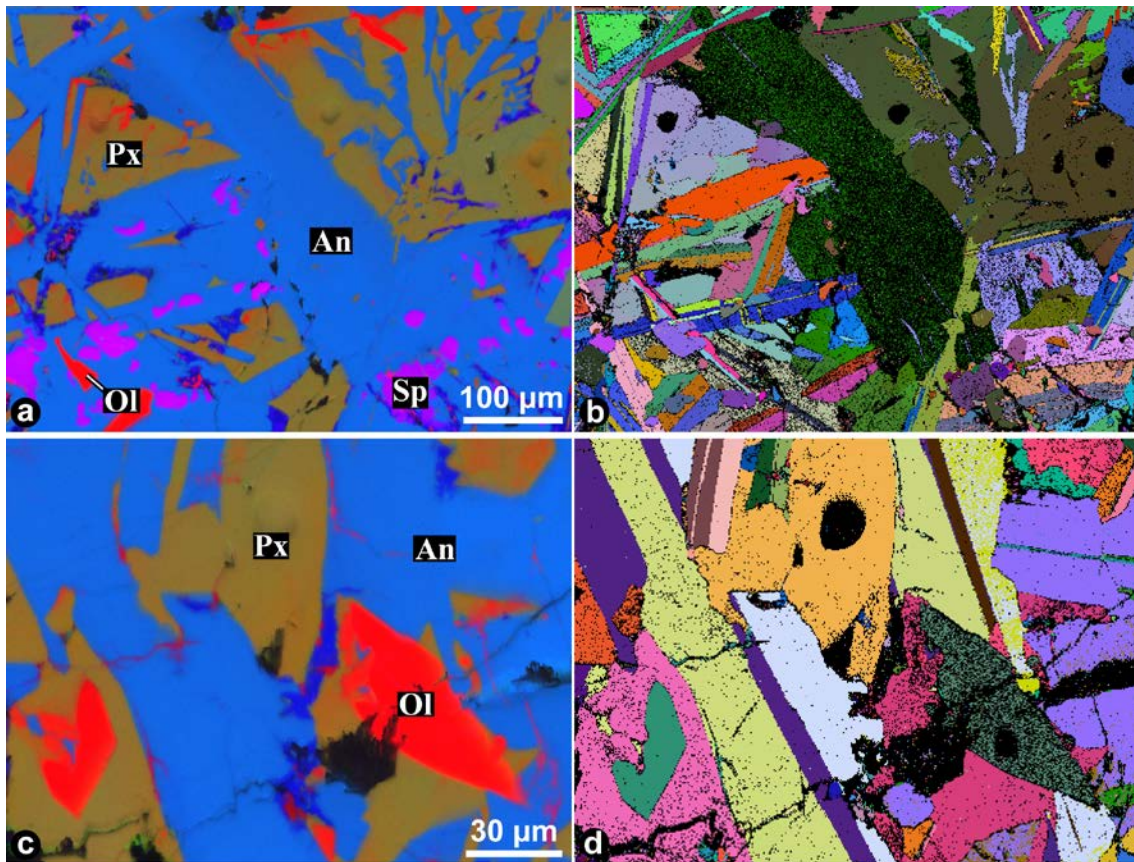


Figure 5. Representative textures of the EK1-04-2 mantle. (a) Combined X-ray elemental map of the area indicated as area 5a in Fig. 1, showing Mg (red), Ca (green), and Al (blue). (b) EBSD Euler map of the area in (a). (c) Combined X-ray elemental map of the area indicated as area 5c in Fig. 1, showing Mg (red), Ca (green), and Al (blue). (d) EBSD Euler map of the area in (c). An, anorthite; Px, pyroxene; Ol, olivine; Sp, spinel.

#### 4.1.2 Oxygen isotopic compositions of minerals

The oxygen isotopic compositions of minerals in EK1-04-2 are summarized in Table 3. Figure 6 shows the oxygen isotopic compositions plotted on a three oxygen

isotope diagram. The oxygen isotopic compositions of all minerals are distributed along the CCAM line ranging between  $\delta^{18}\text{O} = -44$  and  $+9\text{‰}$ , which indicates disequilibrium among the inter- and intra-minerals in the CAI.

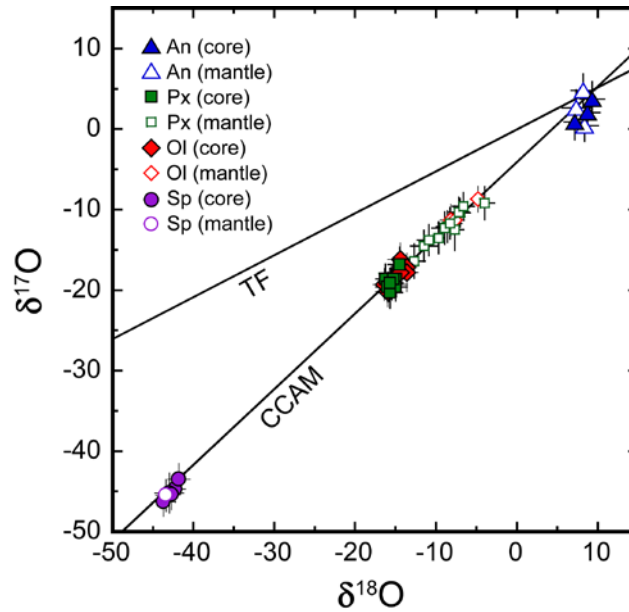


Figure 6. Oxygen isotopic compositions of minerals in EK1-04-2. Error bars are  $2\sigma$ . TF, terrestrial fractionation line; CCAM, carbonaceous chondrite anhydrous mineral line; An, anorthite; Px, pyroxene; Ol, olivine; Sp, spinel.

The oxygen isotopic compositions of spinel are distributed homogeneously at  $\delta^{18}\text{O} \sim -43\text{‰}$ . The oxygen isotopic compositions of anorthite are also distributed homogeneously at  $\delta^{18}\text{O} \sim 8\text{‰}$ . No differences in the oxygen isotopic compositions between the core and mantle are observed for spinel or anorthite. In contrast, olivine and pyroxene have different oxygen isotopic characteristics between the core and mantle. Olivine and pyroxene in the core have the same oxygen isotopic compositions ( $\delta^{18}\text{O} \sim -15\text{‰}$ ), which is intermediate between  $^{16}\text{O}$ -rich spinel and  $^{16}\text{O}$ -poor anorthite, and indicates isotopic equilibrium between olivine and pyroxene in the core.

However, olivine and pyroxene in the mantle have variable oxygen isotopic compositions ( $\delta^{18}\text{O} = -13$  to  $-4\text{‰}$ ) and are slightly depleted in  $^{16}\text{O}$  compared to olivine and pyroxene in the core. The relationships between the oxygen isotopic compositions and the chemical compositions of pyroxene in the mantle are shown in Figure 7. The oxygen isotopic composition tends to become depleted in  $^{16}\text{O}$  with a decrease in the  $\text{Al}/^{24}\text{Mg}$  ratio and  $\text{TiO}_2$  content.

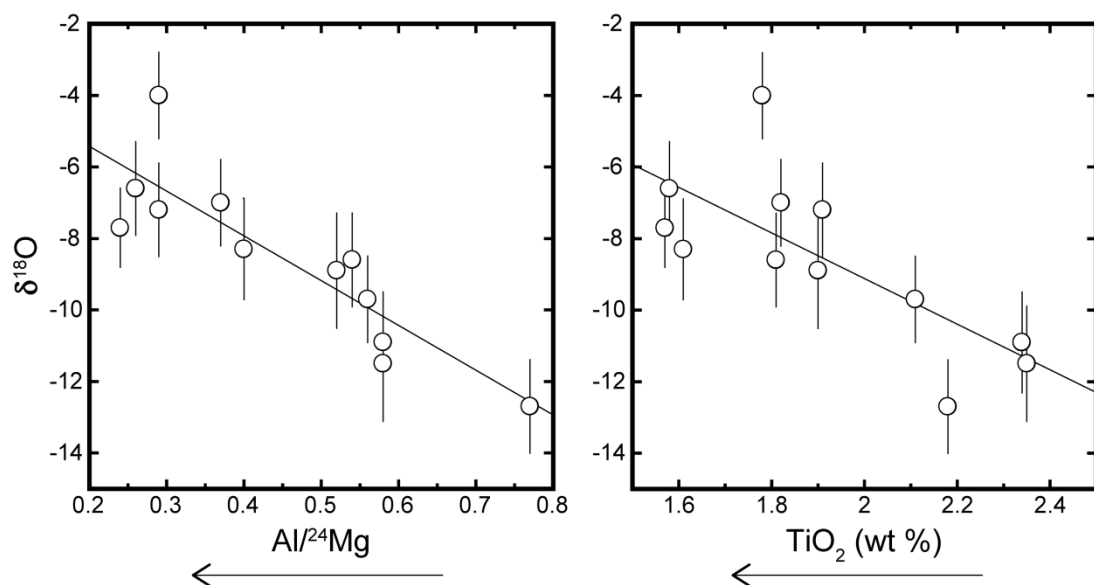


Figure 7. Relationships between the chemical compositions and oxygen isotopic compositions of pyroxene in the mantle. Error bars are  $2\sigma$ . Arrows correspond to directions of compositional change with pyroxene crystal growth.

Table 3. Oxygen isotopic compositions of EK1-04-2 minerals.

mineral	$\delta^{17}\text{O}$	$2\sigma$	$\delta^{18}\text{O}$	$2\sigma$	$\Delta^{17}\text{O}$	$2\sigma$
core						
An	2.0	1.9	8.7	1.5	-2.5	1.8
An	3.7	2.1	9.3	1.5	-1.1	1.6
An	0.9	2.1	7.1	1.2	-2.9	2.1
Px	-18.6	2.2	-14.9	1.4	-10.9	1.9
Px	-19.6	1.7	-15.0	1.4	-11.8	1.7
Px	-16.8	2.1	-14.5	1.4	-9.3	2.0
Px	-19.1	2.0	-15.5	1.4	-11.0	1.8
Px	-18.6	1.8	-16.3	1.1	-10.2	1.7
Px	-18.6	1.7	-15.3	1.6	-10.6	1.7
Px	-19.6	1.8	-16.0	1.4	-11.3	1.6
Px	-20.3	1.9	-15.7	1.5	-12.1	2.0
Px	-19.1	1.8	-15.7	1.1	-11.0	1.5
Ol	-16.2	2.1	-14.4	1.6	-8.8	2.1
Ol	-19.3	2.0	-15.4	1.9	-11.3	1.9
Ol	-17.2	1.7	-13.6	1.2	-10.1	1.6
Ol	-19.6	1.8	-15.8	1.2	-11.4	1.6
Ol	-19.3	2.0	-16.4	1.4	-10.8	1.7
Ol	-20.2	1.9	-16.0	1.5	-11.9	2.0
Ol	-17.8	2.4	-13.6	1.4	-10.8	2.3
Ol	-17.8	2.3	-14.4	1.6	-10.3	1.8
Sp	-44.7	1.7	-42.3	1.3	-22.7	1.6
Sp	-45.2	2.5	-43.0	1.8	-22.9	2.6
Sp	-43.5	2.0	-41.8	1.4	-21.7	2.0
Sp	-45.4	1.9	-42.7	1.1	-23.2	1.7
Sp	-46.3	1.8	-43.7	1.5	-23.6	1.5
mantle						
An	0.4	1.9	8.4	1.6	-3.9	1.7
An	4.8	2.0	8.2	1.4	0.6	1.6
An	2.6	2.2	7.4	1.7	-1.2	2.2
Px	-13.5	1.9	-9.7	1.2	-8.4	1.8
Px	-14.5	1.9	-11.5	1.6	-8.5	1.9
Px	-12.1	1.9	-8.6	1.3	-7.6	1.7
Px	-10.4	1.7	-7.0	1.2	-6.8	1.6
Px	-12.3	2.0	-8.9	1.6	-7.7	1.6
Px	-16.4	2.1	-12.7	1.3	-9.9	1.9
Px	-10.3	1.8	-7.2	1.3	-6.6	1.6
Px	-12.5	2.5	-7.7	1.1	-8.5	2.3
Px	-9.6	1.7	-6.6	1.3	-6.2	1.5
Px	-9.2	2.0	-4.0	1.2	-7.1	1.9
Px	-13.8	1.9	-10.9	1.4	-8.2	1.7
Px	-11.7	1.9	-8.3	1.4	-7.4	1.8
Ol	-8.7	1.6	-4.8	1.0	-6.2	1.4
Ol	-11.3	2.0	-8.2	1.3	-7.1	1.8
Ol	-11.3	1.8	-7.7	1.2	-7.3	1.4
Sp	-45.5	2.0	-43.4	1.3	-23.0	2.1

An: anorthite, Px: pyroxene, Ol: olivine, Sp: spinel

### 4.1.3 Magnesium isotopic compositions of minerals

The magnesium isotopic compositions and  $\text{Al}/^{24}\text{Mg}$  ratios of minerals in EK1-04-2 are summarized in Table 4. Figure 8 shows the magnesium isotopic compositions and  $\text{Al}/^{24}\text{Mg}$  ratios plotted on  $^{26}\text{Al}$ -Mg isochron diagrams.

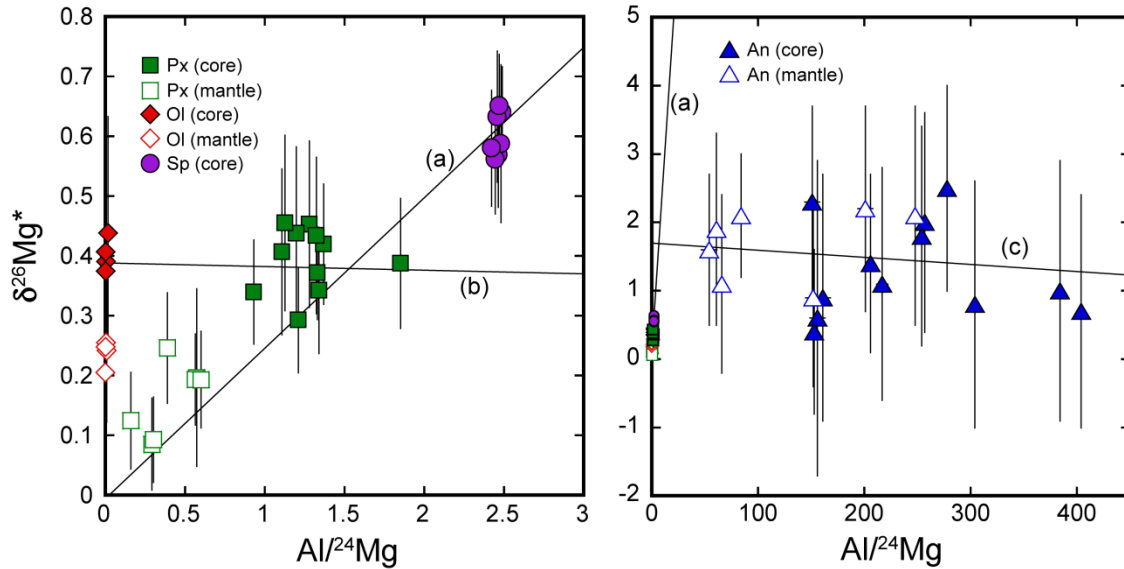


Figure 8.  $^{26}\text{Al}$ -Mg isochrons in EK1-04-2. (a) An isochron of spinel with an initial value of  $(^{26}\text{Al}/^{27}\text{Al})_0 = (3.5 \pm 0.2) \times 10^{-5}$  with  $(\delta^{26}\text{Mg}^*)_0 = -0.003 \pm 0.001\text{‰}$  assuming with the solar initial  $(^{26}\text{Al}/^{27}\text{Al})_0 = (5.252 \pm 0.019) \times 10^{-5}$  and  $(\delta^{26}\text{Mg}^*)_0 = -0.0159 \pm 0.0014\text{‰}$  (Larsen et al., 2011). (b) An isochron of olivine and pyroxene in the core with an initial value of  $^{26}\text{Al}/^{27}\text{Al}_0 = (-1 \pm 7) \times 10^{-6}$  with  $(\delta^{26}\text{Mg}^*)_0 = 0.39 \pm 0.06\text{‰}$ . (c) An apparent isochron of anorthite corresponding to an initial value of  $^{26}\text{Al}/^{27}\text{Al}_0 = (-1 \pm 5) \times 10^{-7}$  with  $(\delta^{26}\text{Mg}^*)_0 = 1.7 \pm 0.7\text{‰}$ . Errors are  $2\sigma$ . An, anorthite; Px, pyroxene; Ol, olivine; Sp, spinel.

Spinel crystals measured have a homogeneous excess  $^{26}\text{Mg}$ , where  $\delta^{26}\text{Mg}^* \sim 0.60\text{‰}$ , which is slightly smaller than that for canonical CAIs ( $\sim 0.91\text{‰}$ ) (Larsen et al., 2011). The magnesium isotopic compositions of spinel in the mantle cannot be measured due to small grain sizes with respect to the primary beam size used. Olivine and pyroxene in the core have homogeneous values of  $\delta^{26}\text{Mg}^* \sim 0.40\text{‰}$ , which are clearly different from for spinel. Olivine and pyroxene in the mantle have lower  $\delta^{26}\text{Mg}^*$  values than the same minerals in the core. Olivine in the mantle has a homogeneous value of  $\delta^{26}\text{Mg}^* \sim 0.24\text{‰}$ . In contrast,  $\delta^{26}\text{Mg}^*$  for pyroxene in the mantle is not homogeneous among the grains and varies in the range of  $0.09\text{‰} < \delta^{26}\text{Mg}^* < 0.25\text{‰}$ , which tends to be smaller than the range for mantle olivine. Anorthite crystals measured have an almost homogeneous value of  $\delta^{26}\text{Mg}^* \sim 1.4\text{‰}$ . These magnesium isotopic

compositions and Al/<sup>24</sup>Mg ratios for the minerals of EK1-04-2 mean that a single isochron line cannot be obtained for all minerals. Therefore, the <sup>26</sup>Al-Mg systematics is in disequilibrium within the CAI. The <sup>26</sup>Al-Mg disequilibrium is consistent with the disequilibrium indicated by petrography and the oxygen isotopic distributions of the CAI.

Table 4. Al/<sup>24</sup>Mg ratios and Mg isotopic compositions of minerals in EK1-04-2.

mineral	Al/ <sup>24</sup> Mg	2σ	δ <sup>26</sup> Mg*	2σ	δ <sup>25</sup> Mg	2σ	mineral	Al/ <sup>24</sup> Mg	2σ	δ <sup>26</sup> Mg*	2σ	δ <sup>25</sup> Mg	2σ
core							Sp	2.46	0.00	0.63	0.11	2.65	0.26
An	217	5	1.1	1.7	3.8	1.5	Sp	2.47	0.00	0.57	0.09	2.55	0.26
An	278	3	2.5	1.5	1.0	1.5	Sp	2.49	0.00	0.64	0.08	2.42	0.26
An	206	3	1.4	1.3	1.1	1.6	Sp	2.47	0.01	0.65	0.09	2.15	0.07
An	161	7	0.9	1.8	1.5	1.5	Sp	2.48	0.01	0.59	0.13	2.72	0.12
An	156	7	0.6	2.3	1.3	1.5	Sp	2.45	0.04	0.56	0.09	2.06	0.07
An	151	7	2.3	1.4	0.6	0.8	Sp	2.42	0.04	0.58	0.10	2.27	0.07
An	257	2	2.0	1.6	1.3	1.4	mantle						
An	254	2	1.8	1.6	1.9	1.5	An	201	7	2.2	1.5	0.5	1.5
An	153	2	0.4	1.2	1.7	1.4	An	84	2	2.1	0.9	1.4	1.4
An	384	2	1.0	1.9	0.7	1.5	An	61	2	1.9	1.4	1.4	1.4
An	304	4	0.8	1.8	2.6	1.5	An	66	2	1.1	1.3	1.7	1.4
An	404	1	0.7	1.7	0.3	1.4	An	54	7	1.6	1.1	2.1	0.8
Px	0.93	0.00	0.34	0.09	2.43	0.16	An	152	7	0.9	1.3	1.9	0.9
Px	1.37	0.01	0.42	0.10	2.89	0.16	An	248	2	2.1	1.6	0.6	1.4
Px	1.34	0.02	0.34	0.11	3.10	0.16	Px	0.57	0.00	0.20	0.15	3.30	0.16
Px	1.33	0.01	0.37	0.08	2.69	0.16	Px	0.29	0.00	0.09	0.08	2.11	0.16
Px	1.21	0.01	0.29	0.09	1.99	0.16	Px	0.57	0.00	0.19	0.08	2.14	0.16
Px	1.85	0.01	0.39	0.11	1.99	0.16	Px	0.39	0.00	0.25	0.09	2.11	0.16
Px	1.28	0.03	0.45	0.14	1.91	0.40	Px	0.60	0.00	0.19	0.08	1.94	0.16
Px	1.32	0.04	0.43	0.13	1.76	0.40	Px	0.16	0.00	0.12	0.08	1.54	0.16
Px	1.20	0.03	0.44	0.14	1.90	0.40	Px	0.30	0.00	0.09	0.07	1.89	0.16
Px	1.11	0.03	0.41	0.14	2.20	0.40	Ol	0.00	0.00	0.21	0.12	2.49	0.05
Px	1.13	0.03	0.46	0.15	2.11	0.40	Ol	0.01	0.01	0.24	0.12	2.51	0.04
Ol	0.00	0.01	0.39	0.14	2.42	0.12	Ol	0.00	0.01	0.25	0.11	2.64	0.04
Ol	0.00	0.00	0.37	0.14	2.29	0.11	Ol	0.00	0.00	0.25	0.12	2.63	0.05
Ol	0.00	0.00	0.41	0.20	2.97	0.09							
Ol	0.02	0.03	0.44	0.19	2.72	0.09							

An: anorthite, Px: pyroxene, Ol: olivine, Sp: spinel

## 4.2 DISCUSSION

### 4.2.1 Multiple melting of EK1-04-2

#### 4.2.1.1 Partial melting of precursor CAI

Disequilibrium oxygen isotopic distributions were observed in EK1-04-2. Spinel ( $\delta^{18}\text{O} \sim -43\text{‰}$ ), anorthite ( $\delta^{18}\text{O} \sim 9\text{‰}$ ), olivine and pyroxene in the core ( $\delta^{18}\text{O} \sim -15\text{‰}$ ), and olivine and pyroxene in the mantle ( $\delta^{18}\text{O} = -13$  to  $-4\text{‰}$ ) were not in equilibrium. From the textural relationships (Fig. 4), the crystallization sequence of the core was spinel, anorthite, olivine, and pyroxene, which is consistent with the crystallization sequence determined from the phase diagram (Fig. 3).

Yurimoto et al. (1998) showed that the disequilibrium oxygen isotopic distributions in a CAI were the result of oxygen isotope exchange between a partial melting melt of a CAI and the surrounding nebular gas. The differences in the oxygen isotopic compositions between spinel and the other minerals in EK1-04-2 can thus be explained by a partial melting of the CAI and oxygen isotope exchange between the partial melting melt and the surrounding nebular gas.

Formation of the CAI could be explained by the following sequential process. (1) A precursor CAI containing  $^{16}\text{O}$ -rich spinel was formed. (2) The CAI, except spinel, was melted in an  $^{16}\text{O}$ -poor nebular gas; spinel survived the melting event as a relict. The heating temperature of this melting event would have been higher than  $\sim 1623$  K and lower than  $\sim 1670$  K, because  $1623$  K is the temperature of olivine crystallization from the melt and  $1670$  K is the liquidus temperature (Stolper, 1982). During the partial melting event, olivine crystals were completely melted and anorthite crystals were partially melted, if these minerals were present in the precursor. The reason for this is discussed in detail later in this section and in section 4.2.2.3. (3) Oxygen isotope exchange occurred between the partial melting melt and the  $^{16}\text{O}$ -poor surrounding nebular gas. As a result of the isotope exchange, the partial melting melt became  $^{16}\text{O}$ -poor ( $\delta^{18}\text{O} \sim -15\text{‰}$ ). (4)  $^{16}\text{O}$ -poor minerals were crystallized from the  $^{16}\text{O}$ -poor melt. Similar oxygen isotopic exchange processes between melts and nebular gas have also been suggested for other CAIs (Yurimoto et al., 1998; Ito et al., 2004; Yoshitake et al., 2005; Aléon et al., 2007; Krot et al., 2008; Yurimoto et al., 2008). The same oxygen isotopic composition of the core olivine and pyroxene indicates that they crystallized during this event and that the oxygen isotopic composition of the nebular gas was  $\delta^{17}\text{O} \sim -19\text{‰}$  and  $\delta^{18}\text{O} \sim -15\text{‰}$ .

The oxygen isotopic compositions of olivine and pyroxene in the mantle of EK1-04-2 are different from those in the core. The distinct oxygen isotopic compositions of mantle minerals therefore suggest that they were formed by subsequent heating events.

#### **4.2.1.2 Second partial melting and the mantle formation**

Although the mantle was composed of the same minerals as the core, the textures and chemical compositions of the mantle and the core were distinct. Spinel and anorthite in the mantle were subhedral or anhedral shaped, while these same minerals in the core were euhedral or subhedral shaped (Figs. 3 and 4). In addition, the chemical compositions of pyroxene crystals in the core and mantle have distinctly different distributions (Fig. 2), which cannot be explained by a single fractional crystallization event from a single melt. These observations indicate that the mantle was formed by the second partial melting and solidification (recrystallization) of the core.

The chemical composition of the mantle of EK1-04-2 is similar to the composition of the PL1 reported in the paper by Tronche et al. (2007), which studied isothermal experiments under the compositions of Type C CAIs and Al-rich chondrules. From the PL1 melt, anorthite was the liquidus mineral and spinel was the second liquidus mineral. This crystallization sequence of the PL1 melt is consistent with the texture of the mantle, where the spinel had subhedral or anhedral shapes (Fig. 5).

Spinel in the mantle has an  $^{16}\text{O}$ -rich composition that is indistinguishable from that in the core (Fig. 6), which indicates that spinel in the mantle was a relict mineral of the second partial melting event. On the other hand, the distinct oxygen isotopic compositions of olivine and pyroxene in the core and the mantle (Fig. 6) suggest that they were not in equilibrium with each other, but indicate that all mantle olivine and pyroxene was crystallized at the second partial melting event. The heating temperature would be higher than  $\sim 1580$  K and lower than  $\sim 1637$  K because olivine and spinel appear from the PL1 melts at  $\sim 1580$  K and  $\sim 1637$  K, respectively (Tronche et al., 2007). The heating temperature of the second partial melting event ( $\sim 1580$  to  $\sim 1637$  K) is slightly lower than that of the first partial melting event that formed the core ( $\sim 1623$  to  $\sim 1670$  K), which supports that the mantle formation was a different process from the core formation. The difference of the melting temperatures suggests that the heating event of the second partial melting could not melt the core part of the CAI and that melting only occurred at the outer edge of the CAI. The unclear boundary between the core and mantle (Fig. 1) is also consistent with the second partial melting temperature. Olivine and pyroxene in the mantle are slightly depleted in  $^{16}\text{O}$  compared to the same

minerals in the core. In addition, pyroxene in the mantle exhibits oxygen isotopic variations ( $\delta^{18}\text{O} = -13$  to  $-4\%$ ), which tend to become  $^{16}\text{O}$ -poor with decreasing Ti and increasing Mg concentration (Fig. 7). Simon et al. (1991) showed that Ti-Al-diopside crystals in Type B CAI melts tend to grow with decreasing Ti and increasing Mg concentration. The observed trends seem to suggest that pyroxene crystals in the mantle grew in a melt with an oxygen isotopic composition that changed from  $^{16}\text{O}$ -rich to  $^{16}\text{O}$ -poor. On the other hand, the oxygen isotopic compositions of olivine in the mantle ( $\delta^{18}\text{O} = -8$  to  $-5\%$ ) ranged from intermediate to equivalent with the most  $^{16}\text{O}$ -poor compositions of pyroxene in the mantle, and the textural relationships (Fig. 5c) show that the crystallization of olivine was prior to pyroxene in the mantle. Thus, mantle olivine, the liquidus mineral, has oxygen isotopic compositions plotted on  $^{16}\text{O}$ -poor region in the oxygen isotopic range shown for mantle pyroxene (Fig. 6). The simple oxygen isotopic exchange model between partial melting melt and the surrounding  $^{16}\text{O}$ -poor nebular gas discussed for the core formation cannot explain the oxygen isotopic variations among the mantle minerals. Non-monotonic variation of the oxygen isotopic composition of the nebular gas may be applicable to explain such variations in the mantle minerals. However, we propose a more simple mechanism to explain these oxygen isotopic variations based on differences in the chemical composition of the mantle and the core (Table 2). The chemical composition of the mantle is similar to that of Al-rich chondrules (Fig. 3); therefore, an admixing process of Al-rich chondrules with the core of EK1-04-2 and subsequent melting to form the mantle can be considered to explain the different chemical compositions of the core and mantle. The melting of CAI-chondrule compound objects is common in the solar nebular gas (Maruyama et al., 1999; Itoh and Yurimoto, 2003; Maruyama and Yurimoto, 2003; Krot et al., 2005, 2007, 2008; Wakaki et al., 2013; Zhang et al., 2014). The range of oxygen isotopic compositions of olivine and pyroxene in the mantle may also be explained by this process. The oxygen isotopic compositions of Al-rich chondrules are depleted in  $^{16}\text{O}$ , typically  $\delta^{18}\text{O} \sim -4\%$  (e.g., Ushikubo et al., 2012), compared to the core minerals, at  $\delta^{18}\text{O} \sim -15\%$ , and comparable with the  $^{16}\text{O}$ -poorest composition for mantle pyroxene and olivine ( $\delta^{18}\text{O} = -4\%$ ). If the mixing of the core minerals in the CAI and Al-rich chondrules had occurred, the newly crystallized minerals would have intermediate  $\delta^{18}\text{O}$  values between  $-15$  and  $-4\%$ , which is consistent with that observed for olivine and pyroxene in the mantle ( $\delta^{18}\text{O} = -13$  to  $-4\%$ ). The heterogeneous oxygen isotopic compositions of olivine and pyroxene in the mantle suggest an incomplete mixing of Al-rich chondrule and CAI components among partial melting melts. Because anorthite was the liquidus mineral and spinel was the second liquidus mineral from the melt with

the chemical composition of the mantle, the presence of relict spinel in the mantle indicates that anorthite was melted lesser extent. This suggests that there were some melt pockets divided by anorthite crystals during the second partial melting event. If the mixing proportions between Al-rich chondrule and CAI components were different at each melt pocket, the oxygen isotopic composition would also be variable among each divided melt, which could form the heterogeneous oxygen isotopic compositions of the mantle olivine and pyroxene. In this model, the  $^{16}\text{O}$ -poorer composition of olivine in the mantle than that of pyroxene in the mantle can be explained because both olivine and pyroxene in the mantle could have the oxygen isotopic compositions in the range of  $\delta^{18}\text{O} \sim -15$  to  $-4\%$ . The relationship between the oxygen isotopic and chemical compositions of mantle pyroxene (Fig. 7) is also consistent with this model, because the Al-rich chondrule components tend to be depleted in  $^{16}\text{O}$  and Ti with respect to the CAI components. Therefore, we conclude that the mantle was formed by the admixing of Al-rich chondrules and a subsequent partial melting process.

The lower  $\delta^{26}\text{Mg}^*$  values for olivine and pyroxene in the mantle than those of the core (Fig. 8) are also consistent with the admixing of Al-rich chondrules because bulk  $\delta^{26}\text{Mg}^*$  values for Al-rich chondrules are  $\delta^{26}\text{Mg}^* \sim 0.1 \%$  (e.g., Bizzarro et al., 2004). By considering the differences in the  $\delta^{26}\text{Mg}^*$  values between olivine and pyroxene in the core and those in the mantle (Fig. 8), at least half of the magnesium in the mantle should be derived from Al-rich chondrule components. The  $\delta^{26}\text{Mg}^*$  variation of pyroxene in the mantle is consistent with different mixing proportions between Al-rich chondrule and CAI components at each melt pocket.

#### **4.2.1.3 Oxygen isotopic compositions of anorthite**

The oxygen isotopic compositions of anorthite were homogeneously distributed and  $^{16}\text{O}$ -poor with respect to the other minerals of EK1-04-2 (Fig. 6). The  $^{16}\text{O}$ -poor nature of anorthite cannot be explained by the partial melting events discussed earlier in sections 4.2.1.1 and 4.2.1.2, because anorthite should be crystallized from the melt prior to olivine and pyroxene, and as a result, the oxygen isotopic compositions of anorthite should be similar to those of olivine and pyroxene. The petrography indicates that anorthite was crystallized in a melt; however, oxygen isotope exchanges by the solid-state diffusion of oxygen isotopes in anorthite on the Allende parent body may have changed the original oxygen isotopic composition. Oxygen self-diffusion in anorthite is relatively faster than that in spinel, olivine and pyroxene (Oishi and Ando, 1984; Ryerson and McKeegan, 1994), although the exchange rate is highly dependent on the crystal sizes (Yurimoto et al., 1989; Fagan et al., 2004a).

The Allende parent body is known to have undergone thermal metamorphism under temperatures of 623-973 K (Keil, 2000; Scott and Krot, 2003; Ito and Messenger, 2010). Figure 9 shows that the oxygen isotopic exchange by solid-state diffusion during the metamorphism is much less than a surface depth of 10  $\mu\text{m}$  depth for spinel, olivine, and pyroxene. The crystal sizes of spinel, olivine, and pyroxene in EK1-04-2 are larger than 10  $\mu\text{m}$ ; therefore, the effect of oxygen isotopic exchange of these minerals during metamorphism was very small. In contrast, anorthite crystals less than 100  $\mu\text{m}$  thick would be in re-equilibrium for oxygen isotopes within the crystals and completely exchange their oxygen isotopes during metamorphism. The oxygen isotopes of anorthite crystals larger than 200  $\mu\text{m}$  thick would be partially disturbed during the metamorphism. The maximum thickness of anorthite crystals in EK1-04-2 was  $\sim 100$   $\mu\text{m}$ , which indicates that the oxygen isotopes of anorthite in EK1-04-2 are re-equilibrated with the matrix materials, which have  $^{16}\text{O}$ -poor characteristics ( $\delta^{17}\text{O} = -1.10\text{‰}$ ,  $\delta^{18}\text{O} = 3.41\text{‰}$ ,  $\Delta^{17}\text{O} = -2.87\text{‰}$ ; Clayton and Mayeda, 1999), during metamorphism on the parent body. The oxygen isotopic composition of anorthite in this study ( $\Delta^{17}\text{O} = -3.9$  to  $+0.6\text{‰}$ ) is consistent with that of the matrix within the analytical error. Therefore, oxygen isotopic composition of anorthite in EK1-04-2 was reset to the matrix value by metamorphism on the Allende parent body, although the igneous morphology of anorthite grains was preserved.

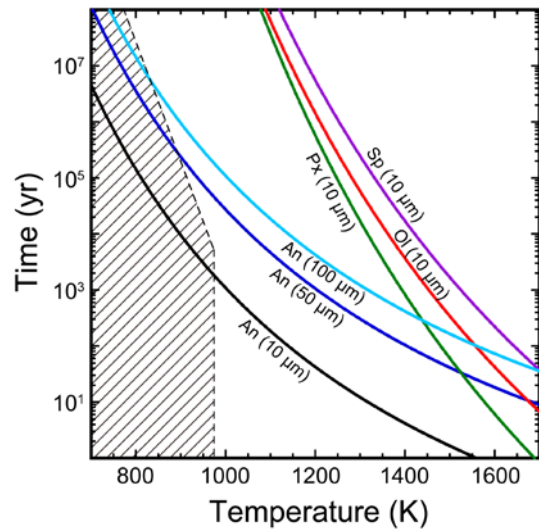


Figure 9. Temperature and time dependence for oxygen self-diffusion distances in minerals. The diffusion distance  $((Dt)^{1/2}$ ; D: diffusion coefficient, t: time) for each mineral is shown in the diagram. The diffusion distances correspond to representative mineral sizes of EK1-04-2 CAI. The shaded area corresponds to the metamorphic condition on the Allende parent body (Keil, 2000; Scott and Krot, 2003; Ito and Messenger, 2010). Oxygen self-diffusion coefficients for anorthite, pyroxene, and spinel were taken from Ryerson and McKeegan (1994), and that for olivine from Oishi and Ando (1984). An, anorthite; Px, pyroxene; Sp, spinel; Ol, olivine.

## 4.2.2 $^{26}\text{Al}$ -Mg chronology of multiple melting of EK1-04-2

### 4.2.2.1 Chronology of spinel formation

Spinel in EK1-04-2 was determined as a relict mineral that survived two partial melting events. There are no simultaneously formed mineral with the spinel and the spinel has little compositional variation; therefore, an isochron cannot be obtained for spinel.

If we assume that the spinel was formed from the solar nebular gas with its Al-Mg system evolved from canonical  $(^{26}\text{Al}/^{27}\text{Al})_0 = (5.252 \pm 0.019) \times 10^{-5}$  and  $(\delta^{26}\text{Mg}^*)_0 = -0.0159 \pm 0.0014\%$  (Larsen et al., 2011), at a certain time after the formation of Solar System, spinel can have the initial values of  $(^{26}\text{Al}/^{27}\text{Al})_0 = (3.5 \pm 0.2) \times 10^{-5}$  and  $(\delta^{26}\text{Mg}^*)_0 = -0.003 \pm 0.001\%$  (Fig. 10). These values are calculated by considering that the  $^{26}\text{Al}$ -Mg system was evolved in the nebular gas ( $\text{Al}/^{24}\text{Mg} = 0.101$ ) until formation of the precursor CAI of EK1-04-2, and then, that evolved in spinel ( $\text{Al}/^{24}\text{Mg} \sim 2.46$ ) after solidification of the spinel. In this model, the age difference between the canonical and spinel in EK1-04-2 is calculated to be  $0.43 \pm 0.05$  Myr. Note that, if the distribution of  $^{26}\text{Al}$  in the solar system were heterogeneous, formation age of spinel would not be calculable from  $\delta^{26}\text{Mg}^*$ .

Let us consider an alternative Al-Mg evolution model assuming that the initial  $^{26}\text{Al}$ -Mg systematics of EK1-04-2 was canonical. This assumption is also conceivable

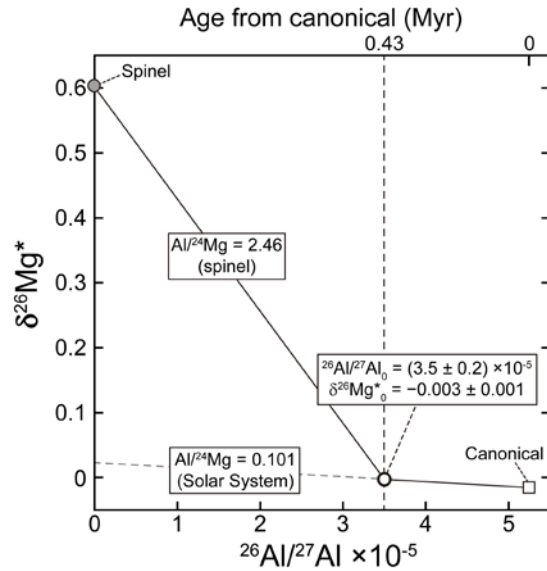


Figure 10. Magnesium isotopic evolution of the spinel in EK1-04-2. The  $^{26}\text{Al}$ -Mg system was evolved in the nebular gas with  $\text{Al}/^{24}\text{Mg} = 0.101$  (Lodders, 2003) from the canonical (open square) (Larsen et al., 2011) until formation of the spinel (open circle), which corresponds to isolation from the nebular gas. After spinel formation, the  $^{26}\text{Al}$ -Mg system was evolved in the spinel with  $\text{Al}/^{24}\text{Mg} = 2.46$  and become the present value observed (filled circle). The evolution of  $^{26}\text{Al}$ -Mg system reveals the initial values of spinel are  $(^{26}\text{Al}/^{27}\text{Al})_0 = (3.5 \pm 0.2) \times 10^{-5}$  and  $(\delta^{26}\text{Mg}^*)_0 = -0.003 \pm 0.001\%$ . This indicates that the age difference between the canonical and the spinel, precursor CAI is  $0.43 \pm 0.05$  Myr.

because spinels in many CAIs are often plotted on the canonical line of the  $^{26}\text{Al}$ -Mg systematics even if they have experienced multiple melting (e.g., MacPherson et al., 2012). Thus, to reset the  $^{26}\text{Al}$ -Mg systematics of spinel by a melting mechanism, complete melting of the CAI is required because spinel is the liquidus mineral. If such melting occurs,  $\delta^{26}\text{Mg}^*$  of the spinel crystallized from the melt would be larger than the canonical value if the  $\text{Al}/^{24}\text{Mg}$  ratio of the melt were larger than that for the spinel, whereas  $\delta^{26}\text{Mg}^*$  for the spinel would be smaller than the canonical value if the  $\text{Al}/^{24}\text{Mg}$  ratio of the melt were smaller than that for the spinel. In the case of EK1-04-2, the  $\text{Al}/^{24}\text{Mg}$  ratio of the melt is inferred to be 2.38, which corresponds to the core composition and is smaller than the value for spinel ( $\text{Al}/^{24}\text{Mg} \sim 2.46$ ). If the total melting had occurred after the complete decay of  $^{26}\text{Al}$ ,  $\delta^{26}\text{Mg}^*$  of the recrystallized spinel would be 0.89‰. On the other hand, if the total melting had occurred before the complete decay of  $^{26}\text{Al}$ ,  $\delta^{26}\text{Mg}^*$  would be intermediate between 0.89‰ and 0.91‰. In summary,  $\delta^{26}\text{Mg}^*$  of the spinel would become smaller than the canonical, if the total melting event had occurred after the canonical CAI formation, but the value should be no less than 0.89‰. This is inconsistent with the  $\delta^{26}\text{Mg}^*$  of the spinel in EK1-04-2. Therefore, the remelting of canonical CAI can be ruled out for the formation of EK1-04-2 spinel by crystallization.

#### 4.2.2.2 $^{26}\text{Al}$ -Mg Chronology of the partial melting events

The precursor CAI containing  $^{16}\text{O}$ -rich spinel underwent two partial melting events, the first of which formed the core, while the second partial melting event formed the mantle. Olivine and pyroxene in the core were formed by the first partial melting event. These minerals have homogeneous oxygen isotopic compositions ( $\delta^{18}\text{O} \sim -15\text{‰}$ ) and the isochron for these minerals gives  $(^{26}\text{Al}/^{27}\text{Al})_0 = (-1 \pm 7) \times 10^{-6}$  and  $(\delta^{26}\text{Mg}^*)_0 = 0.39 \pm 0.06\text{‰}$  (Fig. 8). These minerals were crystallized in equilibrium for oxygen and magnesium isotopes during the first melting event. The relative age difference between the initial  $(^{26}\text{Al}/^{27}\text{Al})_0$  values for the spinel and olivine-pyroxene isochrons is calculated to be  $>1.6$  Myr. The age difference between the precursor CAI formation and the first partial melting event can be independently calculated using the difference between the  $(\delta^{26}\text{Mg}^*)_0$  values of the two isochrons and the  $\text{Al}/^{24}\text{Mg}$  value at the intersect. In this method, the calculated age difference between the precursor CAI formation and the first partial melting event would be at least 1.9 Myr, which is comparable with the time interval of 1.6 Myr determined from the difference of the initial  $(^{26}\text{Al}/^{27}\text{Al})_0$  values. This consistency of the time intervals supports the reliability of the isochrons for olivine-pyroxene and spinel.

In summary, the precursor CAI containing  $^{16}\text{O}$ -rich spinel was formed at 0.43 Myr after the canonical or formed in the solar nebula having  $(^{26}\text{Al}/^{27}\text{Al})_0 = (3.5 \pm 0.2) \times 10^{-5}$ , and the first partial melting event occurred at least 1.6 Myr after the precursor CAI formation. This indicates that the precursor CAI was retained in the solar nebula for at least 1.6 Myr after formation.

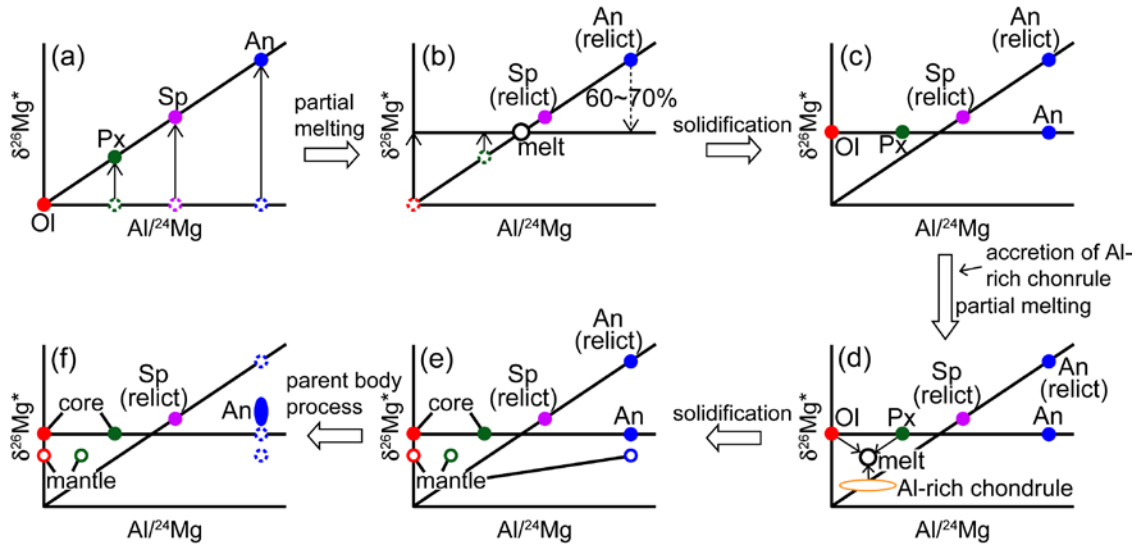


Figure 11. Schematic diagram of Al-Mg evolution for EK1-04-2. (a) The precursor CAI was formed at the timing of the initial value of  $(^{26}\text{Al}/^{27}\text{Al})_0 = (3.5 \pm 0.2) \times 10^{-5}$ . (b) After almost all  $^{26}\text{Al}$  had been decayed, the first partial melting event occurred. 60-70% of anorthite and other minerals, except spinel, in the precursor CAI were melted. The melting process reset the  $^{26}\text{Al}$ -Mg systematics of the melt. (c) Olivine, pyroxene, and anorthite in the core were crystallized. (d) After the accretion of Al-rich chondrules on the CAI, the second partial melting occurred. The melt composition was partially mixed between melt components of the CAI and those of the Al-rich chondrules. (e) Olivine, pyroxene, and anorthite were crystallized from the melt to form the mantle. (f) Magnesium isotopes in anorthite were reset during thermal metamorphism in the Allende parent body. An, anorthite; Px, pyroxene; Ol, olivine; Sp, spinel.

The partial melting events isotopically homogenize the partial melting melt according to the  $\text{Al}/^{24}\text{Mg}$  ratio of the melt (Fig. 11b). The  $\text{Al}/^{24}\text{Mg}$  ratio of the partial melting melt from the first partial melting event was a point at the intersection of the isochron for olivine and pyroxene in the core with that for spinel (“melt” in Fig. 11b). The expected  $\text{Al}/^{24}\text{Mg}$  ratio of the melt is  $\sim 1.6$  (Fig. 8). However, the measured  $\text{Al}/^{24}\text{Mg}$  ratio of the core excluding the spinel component is  $\sim 2.3$ , which is slightly higher than that for  $\text{Al}/^{24}\text{Mg}$  ratio of the melt ( $\text{Al}/^{24}\text{Mg} \sim 1.6$ ). The crystallization sequence of the core is spinel, anorthite, olivine, and pyroxene; therefore  $\text{Al}/^{24}\text{Mg} \sim 1.6$  can be obtained

if anorthite in the core was incompletely melted during the partial melting event. The fraction of melted anorthite inferred from the abundance and chemical compositions of the minerals is 60-70%. Therefore, we infer that olivine, pyroxene, and 60-70% of anorthite in the precursor CAI were melted by the first melting event that formed the core.

After the first partial melting event, admixing of Al-rich chondrules to the CAI and subsequent flash heating (partial melting and recrystallization) occurred to form the mantle, as discussed in section 4.2.1.2. The lower  $\delta^{26}\text{Mg}^*$  values for olivine and pyroxene in the mantle compared with those in the core are explained by the mixing of the Al-rich chondrule compositions (Figs. 11d, e). The variation for the  $\delta^{26}\text{Mg}^*$  values for olivine and pyroxene in the mantle could be also due to differences in the mixing proportions of the Al-rich chondrule component with the host CAI component among each melt pocket. Pyroxene with lower Al/<sup>24</sup>Mg ratios tends to have lower  $\delta^{26}\text{Mg}^*$  values (Fig. 8) and <sup>16</sup>O-poorer compositions (Fig. 7). This is consistent with the results that indicate heterogeneity among the melt pockets because both lower  $\delta^{26}\text{Mg}^*$  value and <sup>16</sup>O-poorer composition can be explained by contributions from the Al-rich chondrule component, which suggests that olivine and pyroxene were not in equilibrium. Therefore, the <sup>26</sup>Al-Mg systematics cannot be used to determine the age of this second partial melting event. However, the timing for admixing of the Al-rich chondrule and heating is apparently after the first partial melting event that formed the core. Thus, it is indicated that the precursor CAI was retained in the solar nebula for at least 1.6 Myr after its formation, and the precursor CAI underwent multiple partial melting event in the solar nebula.

#### 4.2.2.3 Magnesium isotopic compositions of anorthite

The regression line of anorthite showed an initial  $(^{26}\text{Al}/^{27}\text{Al})_0 = (-1 \pm 5) \times 10^{-7}$  with initial  $(\delta^{26}\text{Mg}^*)_0 = 1.7 \pm 0.7\text{‰}$  (Fig. 8). At the first partial melting event, 60-70% of anorthite was melted, as discussed in section 4.2.2.1; therefore, ~30% of anorthite should be plotted on the spinel isochron of  $(^{26}\text{Al}/^{27}\text{Al})_0 = (3.5 \pm 0.2) \times 10^{-5}$ . However, such plots of anorthite have not been observed in EK1-04-2 (Fig. 8). Moreover, the Al-Mg isotopic compositions of anorthite are not plotted on the isochron formed by olivine and pyroxene in the core, although some anorthite grains must be newly crystallized from the melt during cooling at the first and second partial melting.

Fast diffusivity of magnesium in anorthite crystals implies that re-equilibrium of magnesium isotopes could be achieved for anorthite crystals during thermal metamorphism on the Allende parent body (LaTourette and Wasserburg, 1998). The

anorthite crystals could have exchanged their magnesium isotopes with adjacent minerals in EK1-04-2 and the Allende matrix materials during metamorphism. Redistributions of magnesium isotopes between anorthite and adjacent minerals have been suggested for other CAIs (Podosek et al., 1991; Fagan et al., 2007; MacPherson et al., 2012).

The isotopic exchange of magnesium by solid-state self-diffusion for each mineral in EK1-04-2 under metamorphism was evaluated using the same method as that for oxygen isotope exchange in section 4.2.1.3 (Fig. 12). We used self-diffusion coefficients from the literature (Morioka, 1981; Sheng et al., 1992; LaTourette and Wasserburg, 1998; Liermann and Ganguly, 2002), in addition to the Fe-Mg inter-diffusion coefficient in pyroxene (Müller et al., 2013) due to the absence of experimental data for magnesium self-diffusion in pyroxene. Fe-Mg inter-diffusion is usually faster than magnesium self-diffusion in ferromagnesian silicates (Morioka, 1981); therefore, magnesium self-diffusion in pyroxene would be slower than Fe-Mg inter-diffusion.

Magnesium exchange rates in olivine and pyroxene are slower than that in anorthite. Magnesium self-diffusion coefficients for spinel from two studies were significantly different (Sheng et al., 1992; Liermann and Ganguly, 2002). However, if the magnesium isotopes in 100  $\mu\text{m}$ -sized anorthite equilibrated by diffusion, equilibrium also be achieved in 10  $\mu\text{m}$ -sized spinel. The magnesium isotopes in 10  $\mu\text{m}$ -sized

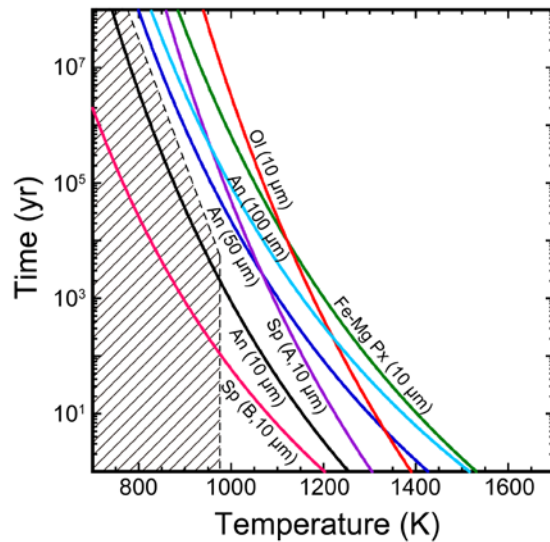


Figure 12. Temperature and time dependences for magnesium self-diffusion distances  $((Dt)^{1/2}$ ; D: diffusion coefficient, t: time) in minerals. The diffusion distance for each mineral is shown in the diagram. The shaded area corresponds to the equilibrium condition inferred by the Allende parent body metamorphism. Magnesium self-diffusion coefficients were obtained from the literature for anorthite, An (LaTourette and Wasserburg, 1998), olivine, Ol (Morioka, 1981), and spinel, Sp (A) (Sheng et al., 1992) and Sp (B) (Liermann and Ganguly, 2002). Fe-Mg inter-diffusion in pyroxene, Fe-Mg Px (Müller et al., 2013).

anorthite grains easily achieve equilibrium during metamorphism of the Allende parent body, whereas those in 100  $\mu\text{m}$ -sized anorthite grains may not equilibrate completely during metamorphism (Fig. 12).

Of anorthite, 30-40% was a relict mineral from the first partial melting event, as discussed in section 4.2.2.1. When the magnesium isotopes re-equilibrium was achieved among anorthite crystals of the core, the homogenized  $\delta^{26}\text{Mg}^*$  values could be calculated as  $\sim 17\text{‰}$ , which is significantly higher than  $\delta^{26}\text{Mg}^*$  measured for anorthite. Thus, the redistributions of magnesium isotopes between anorthite and other minerals are necessary to explain the Al-Mg isotopic compositions of anorthite in EK1-04-2. If the magnesium isotopes in 100  $\mu\text{m}$ -sized anorthite equilibrated by diffusion, those in 10  $\mu\text{m}$ -sized spinel would also achieve equilibrium (Fig. 12). Spinel crystals were enclosed by anorthite crystals (Fig. 4). Therefore, the redistributions in magnesium isotopes between spinel and adjacent anorthite crystals should be considered. The change of  $\delta^{26}\text{Mg}^*$  for anorthite can be calculated using the number of magnesium atoms in the diffusion volume of anorthite and spinel, and starting with  $\delta^{26}\text{Mg}^*$  for anorthite (17‰) and that for spinel (0.6‰).  $\delta^{26}\text{Mg}^*$  for anorthite could be diluted to be  $\sim 1\text{‰}$  when the relative amount of spinel to anorthite is 1:10. When the relative amount of spinel to anorthite is 4:3, which corresponds to that in the core of EK1-04-2,  $\delta^{26}\text{Mg}^*$  for anorthite should become  $\sim 0.64\text{‰}$ . These calculations imply that the Al-Mg isotopic compositions of anorthite in EK1-04-2 can be explained by the redistributions of magnesium isotopes between spinel and adjacent anorthite crystals. Figure 8 shows that the mantle anorthite and some data for core anorthite have significantly higher  $\delta^{26}\text{Mg}^*$  values than those of spinel. In the mantle, spinel is rare (1%), while anorthite is abundant (57%), which indicates that the magnesium isotopes in anorthite were not easily homogenized with spinel and corresponds to the mantle anorthite having relatively high  $\delta^{26}\text{Mg}^*$  compared with the core anorthite. Core anorthite crystals with relatively high  $\delta^{26}\text{Mg}^*$  values were located near the boundary between the core and mantle where the spinel is almost absent, except one spot. These observations are consistent with the redistributions in magnesium isotopes between anorthite and adjacent spinel. In contrast to anorthite, the maximum change of  $\delta^{26}\text{Mg}^*$  for spinel was less than 0.04‰, which is within the analytical error, and thus, the change is negligible.

Even if the magnesium isotopes were derived from the Allende matrix minerals, the change of  $\delta^{26}\text{Mg}^*$  for the spinel could be estimated from the iron contents of the spinel. Spinel in the core typically has  $\text{Mg}/(\text{Mg}+\text{Fe}) \sim 0.99$ . When all of the iron in the spinel is derived during metamorphism,  $\sim 1\%$  of the magnesium was exchanged for iron. Diffusivity for magnesium isotopes and for  $\text{Fe}^{2+}$  in spinel is almost the same or that for

$\text{Fe}^{2+}$  in spinel is faster (Liermann and Ganguly, 2002); therefore, if amounts of magnesium and iron supplied during metamorphism were the same, less than 1% of magnesium in spinel was exchanged for the magnesium from the Allende matrix minerals, and the change of  $\delta^{26}\text{Mg}^*$  for the spinel of EK1-04-2 can be estimated as less than 0.01‰. Moreover, the heterogeneity of the FeO contents within spinel crystals suggests that spinels of EK1-04-2 have not achieved re-equilibrium with each other. Therefore, the original  $\delta^{26}\text{Mg}^*$  values for spinel have been preserved within the analytical errors although a negligibly small change may have occurred.

### 4.3 CONCLUSIONS

EK1-04-2 is mainly composed of spinel, anorthite, olivine, and pyroxene, and has a core and mantle structure. The oxygen isotopic compositions of minerals were distributed along the CCAM line ( $\delta^{18}\text{O} = -44$  to  $+9\%$ ). Spinel was  $^{16}\text{O}$ -rich ( $\delta^{18}\text{O} \sim -43\%$ ), while anorthite was  $^{16}\text{O}$ -poor ( $\delta^{18}\text{O} \sim +8\%$ ). Olivine and pyroxene in the core had the same oxygen isotopic composition ( $\delta^{18}\text{O} \sim -15\%$ ), while the oxygen isotopic compositions of those minerals in the mantle were variable and slightly depleted in  $^{16}\text{O}$  ( $\delta^{18}\text{O} = -13$  to  $-4\%$ ) compared with these minerals in the core. On the  $^{26}\text{Al}$ -Mg isochron diagram, spinel was plotted on a line of  $(^{26}\text{Al}/^{27}\text{Al})_0 = (3.5 \pm 0.2) \times 10^{-5}$ , anorthite was plotted on a line of  $(^{26}\text{Al}/^{27}\text{Al})_0 = (-1 \pm 5) \times 10^{-7}$ , and olivine and pyroxene in the core were plotted on a line of  $(^{26}\text{Al}/^{27}\text{Al})_0 = (-1 \pm 7) \times 10^{-6}$ . Plots of olivine and pyroxene in the mantle were scattered below the isochron of these minerals in the core. The coordinated study of petrography, oxygen isotopes, and  $^{26}\text{Al}$ -Mg chronology indicated that EK1-04-2 underwent two partial melting events after the precursor CAI formation (Fig. 13). The precursor CAI was formed at 0.43 Myr after formation of the Solar System defined by canonical CAI formation. The first partial melting occurred at least 1.6 Myr after the precursor CAI formation. The precursor CAI containing  $^{16}\text{O}$ -rich spinel partially melted in the  $^{16}\text{O}$ -poor nebular gas and oxygen isotope exchange occurred between the melt and nebular gas.  $^{16}\text{O}$ -poor olivine and pyroxene were subsequently crystallized from the melt. After some period, the admixing of Al-rich chondrule to the CAI occurred and the CAI experienced partial melting again. The second partial melting event formed the core-mantle structure of EK1-04-2. The oxygen and magnesium isotopes in anorthite were selectively reset by solid-state diffusion during thermal metamorphism in the Allende parent body with a negligibly small disturbance of other minerals in EK1-04-2. Our findings show that the CAI was retained in the solar nebula for at least 1.6 Myr and underwent multiple melting events in the nebula. The oxygen and magnesium isotopes in anorthite were re-distributed during

thermal metamorphism in the Allende parent body.

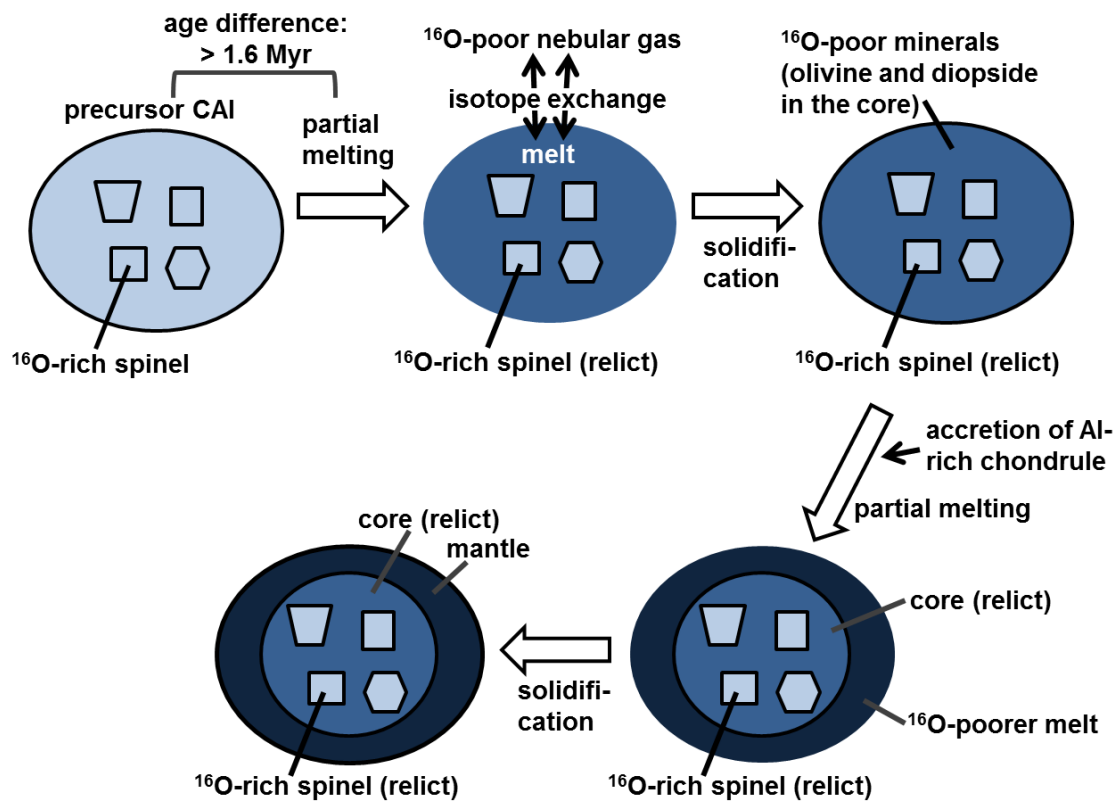


Figure 13. Schematic scenario for the formation of EK1-04-2. The CAI underwent two partial melting events after formation of the precursor CAI. The formation sequence is described as follows. The precursor CAI containing  $^{16}\text{O}$ -rich spinel was partially melted in  $^{16}\text{O}$ -poor nebular gas. The age difference between the precursor CAI formation and this partial melting was at least 1.6 Myr. Oxygen isotope exchange occurred between the partial melting melt and the surrounding  $^{16}\text{O}$ -poor nebular gas. After solidification, both  $^{16}\text{O}$ -rich spinel and  $^{16}\text{O}$ -poor minerals were present in the CAI. Al-rich chondrules were accreted on the CAI. The second partial melting occurred on the CAI surrounded by Al-rich chondrules and this event formed the mantle of the CAI.

## 5. $^{26}\text{Al}$ -Mg chronology and magnesium isotopic fractionation for reversely zoned melilite crystals in a fluffy Type A CAI from Vigarano CV3

### 5.1 RESULTS

#### 5.1.1 Petrographic observation

V2-01 is the fluffy Type A CAI from the Vigarano CV3 with a size of ~7 mm across. A detailed petrographic description for V2-01 and chemical and oxygen isotopic distributions in the reversely zoned melilite crystals were presented in Katayama et al. (2012). Figure 1 shows a backscattered electron (BSE) image and an elemental map of the CAI. The CAI is mainly composed of melilite, in addition to spinel, hibonite, fassaite, perovskite and Fe-metal as accessory minerals. Anorthite is present as secondary alteration mineral replacing melilite. Spinel and hibonite are mainly observed at limited part of the CAI and are enclosed by melilite crystals. Another area is mostly composed of numerous melilite crystals having sizes of ~50 to 600  $\mu\text{m}$ . Two types of fassaite are present in V2-01. Lath shaped fassaite crystals with sizes of less than 1  $\mu\text{m}$

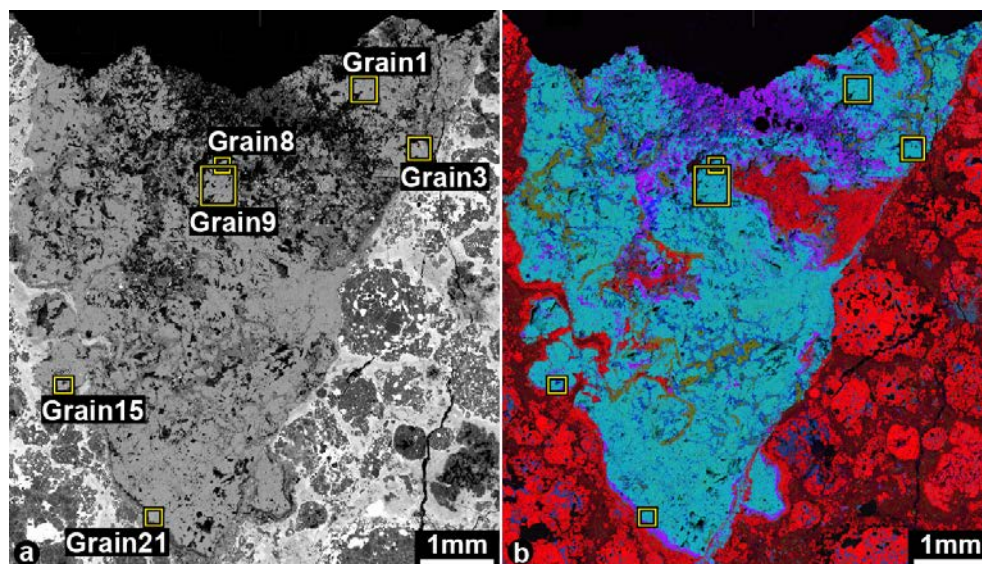


Figure 1. (a) Backscattered electron (BSE) image of the fluffy Type A CAI, V2-01, from the Vigarano CV3 chondrite. Yellow boxes indicate the areas of grains 1, 3, 8, 9, 15, and 21, respectively. (b) Combined X-ray elemental map of V2-01 with Mg (red), Ca (green), and Al (blue).

are observed within the melilite crystals. Rounded anhedral fassaite crystals ranging in size from of several microns to ~50  $\mu\text{m}$  are also observed within the melilite crystals and are often attached with perovskite grains. V2-01 shows irregular “fluffy” shape and has a Wark-Lovering (W-L) rim (Wark and Lovering, 1977) surrounding the CAI entirely. The W-L rim shows a mineral layer of spinel, melilite and diopside. The W-L rim minerals and forsterite accretionary rim often seem to be present at the CAI interior due to the highly irregular rim shape of the CAI.

### 5.1.2 Chemical and oxygen isotopic zoning of reversely zoned melilite crystals

Katayama et al. (2012) examined nine reversely zoned melilite crystals from V2-01 by the oxygen isotope measurement. In this paper, we have measured Al-Mg isotopic compositions of six melilite grains (grains 1, 3, 8, 9, 15, and 21) from those nine grains. Four grains (grains 1, 9, 15, and 21) were attached with the W-L rim while two grains (grains 3 and 8) were not attached with the W-L rim. We summarize descriptions for the chemical and oxygen isotopic zoning of six reversely zoned melilite crystals below.

The grain 1 has a size of 200 $\times$ 400  $\mu\text{m}$  and is attached with the W-L rim (Fig. 2a). The grain 1 shows reverse zoning from core (~ $\text{\AA}k30$ ) to rim (~ $\text{\AA}k4$ ), although highly gehlenitic composition (< ~ $\text{\AA}k6$ ) was only present at the W-L rim side of the grain. The chemical zoning pattern seems to be continuous with an adjacent grain at right side of the grain 1 (Fig. 2a). The oxygen isotopic variation was found at the chemical composition ranging from  $\text{\AA}k6$  to  $\text{\AA}k5$ . The oxygen isotopic composition was homogeneously  $^{16}\text{O}$ -poor at the grain interior ( $\Delta^{17}\text{O} \sim -6\text{‰}$ ) and changed to  $^{16}\text{O}$ -rich from  $\text{\AA}k6$  continuously to  $\Delta^{17}\text{O} \sim -25\text{‰}$  near the rim ( $\text{\AA}k5$ ).

The grain 3 has a size of 250 $\times$ 300  $\mu\text{m}$  and is not attached with the W-L rim (Fig. 2b). The grain 3 shows reverse zoning from core (~ $\text{\AA}k21$ ) to rim (~ $\text{\AA}k5$ ). The oxygen isotopic compositions of the grain 3 were homogeneously distributed ( $\Delta^{17}\text{O} \sim -5\text{‰}$ ).

The grain 8 has a size of 150 $\times$ 200  $\mu\text{m}$  and is not attached with the W-L rim. The upper half of the crystal is shown in Fig. 2c. The grain 8 shows reverse zoning from core (~ $\text{\AA}k15$ ) to rim (~ $\text{\AA}k5$ ). The line profiles of chemical and oxygen isotopic compositions (Fig. 7 of Katayama et al., 2012) showed that the oxygen isotopic composition was homogeneous at the grain interior ( $\Delta^{17}\text{O} \sim -13\text{‰}$ ) and changed to more  $^{16}\text{O}$ -rich composition from  $\text{\AA}k7$  continuously to  $\Delta^{17}\text{O} \sim -20\text{‰}$  near the rim ( $\text{\AA}k4$ ). The grain 9 has a size of 300 $\times$ 600  $\mu\text{m}$  and is attached with the W-L rim. The upper half of the crystal is shown in Fig. 2d. The grain 9 shows reverse zoning from core (~ $\text{\AA}k18$ )

to rim ( $\sim\text{\AA}k5$ ). The oxygen isotopic variation was found at the chemical composition ranging from  $\text{\AA}k8$  to  $\text{\AA}k5$ . The oxygen isotopic compositions were ranged from  $\Delta^{17}\text{O} = -5$  to  $-28\text{\textperthousand}$  and tend to become  $^{16}\text{O}$ -rich composition with decreasing a distance from crystal rim.

The grain 15 has a size of  $80\times 150\ \mu\text{m}$  and is attached with the W-L rim (Fig. 2e). The grain 15 shows reverse zoning from core ( $\sim\text{\AA}k20$ ) to rim ( $\sim\text{\AA}k3$ ), although highly gehlenitic composition ( $< \sim\text{\AA}k8$ ) was only present at the W-L rim side of the grain. The oxygen isotopic variation was found at the chemical composition ranging from  $\text{\AA}k6$  to  $\text{\AA}k3$ . The oxygen isotopic composition was homogeneously  $^{16}\text{O}$ -poor at the grain interior ( $\Delta^{17}\text{O} \sim -7\text{\textperthousand}$ ) and changed to  $^{16}\text{O}$ -rich from  $\text{\AA}k6$  to  $\Delta^{17}\text{O} \sim -16\text{\textperthousand}$  near the rim ( $\text{\AA}k3$ ).

The grain 21 has a size of  $80\times 120\ \mu\text{m}$  and is attached with the W-L rim (Fig. 2f). The grain 21 shows reverse zoning from core ( $\sim\text{\AA}k24$ ) to rim ( $\sim\text{\AA}k2$ ), although highly gehlenitic composition ( $< \sim\text{\AA}k6$ ) was only present at the W-L rim side of the grain. The oxygen isotopic variation was found at the chemical composition ranging from  $\text{\AA}k5$  to  $\text{\AA}k2$ . The oxygen isotopic composition was homogeneously  $^{16}\text{O}$ -poor at the grain interior ( $\Delta^{17}\text{O} \sim -8\text{\textperthousand}$ ) and changed to  $^{16}\text{O}$ -rich from  $\text{\AA}k5$  continuously to  $\Delta^{17}\text{O} \sim -20\text{\textperthousand}$  near the rim ( $\sim\text{\AA}k2$ ).



### 5.1.3 $^{26}\text{Al}$ -Mg isochrons of reversely zoned melilite crystals

The Al-Mg isotopic compositions of the reversely zoned melilite crystals in V2-01 are summarized in Table 1. Figure 3 shows the magnesium isotopic compositions and  $\text{Al}^{24}/\text{Mg}$  ratios of each grain plotted on  $^{26}\text{Al}$ -Mg isochron diagrams. Single  $^{26}\text{Al}$ -Mg isochrons seem to be obtained for each grain, respectively. The data plots for each grain are not systematically scattered from the isochron lines at either high or low sides of  $\text{Al}^{24}/\text{Mg}$  ratio. The isochron of grain 1 shows an initial value of  $(^{26}\text{Al}/^{27}\text{Al})_0 = (4.6 \pm 0.3) \times 10^{-5}$  and  $(\delta^{26}\text{Mg}^*)_0 = 0.3 \pm 0.7\text{‰}$  (Fig. 3a). The isochron of grain 3 shows an initial value of  $(^{26}\text{Al}/^{27}\text{Al})_0 = (4.7 \pm 0.6) \times 10^{-5}$  and  $(\delta^{26}\text{Mg}^*)_0 = 0.1 \pm 1.0\text{‰}$  (Fig. 3b). The isochron of grain 8 shows an initial value of  $(^{26}\text{Al}/^{27}\text{Al})_0 = (4.6 \pm 0.4) \times 10^{-5}$  and  $(\delta^{26}\text{Mg}^*)_0 = 0.3 \pm 1.0\text{‰}$  (Fig. 3c). The isochron of grain 9 shows an initial value of  $(^{26}\text{Al}/^{27}\text{Al})_0 = (4.9 \pm 0.4) \times 10^{-5}$  and  $(\delta^{26}\text{Mg}^*)_0 = -0.2 \pm 0.8\text{‰}$  (Fig. 3d). The isochron of grain 15 shows an initial value of  $(^{26}\text{Al}/^{27}\text{Al})_0 = (4.8 \pm 0.3) \times 10^{-5}$  and  $(\delta^{26}\text{Mg}^*)_0 = -0.4 \pm 0.6\text{‰}$  (Fig. 3e). The isochron of grain 21 shows an initial value of  $(^{26}\text{Al}/^{27}\text{Al})_0 = (4.5 \pm 0.3) \times 10^{-5}$  and  $(\delta^{26}\text{Mg}^*)_0 = 0.3 \pm 0.7\text{‰}$  (Fig. 3f). Validities of the isochrons for each grain are tested later after the discussion for their formation processes. The inferred initial values for all grains are indistinguishable each other (Fig. 4). When we define the single isochron for all six melilite grains, an initial value would be  $(^{26}\text{Al}/^{27}\text{Al})_0 = (4.70 \pm 0.14) \times 10^{-5}$  and  $(\delta^{26}\text{Mg}^*)_0 = 0.04 \pm 0.29\text{‰}$  (Fig. 5).

Table 1. Al/<sup>24</sup>Mg ratios and Mg isotopic compositions of melilite crystals in V2-01.

Grain	#	Al/ <sup>24</sup> Mg	2σ	δ <sup>26</sup> Mg*	2σ	δ <sup>25</sup> Mg	2σ	Grain	#	Al/ <sup>24</sup> Mg	2σ	δ <sup>26</sup> Mg*	2σ	δ <sup>25</sup> Mg	2σ
1	87	18.91	0.06	6.2	1.2	2.2	1.0	8	181	21.91	0.04	8.6	1.2	0.9	0.8
1	89	47.36	0.15	16.5	1.2	0.7	1.0	9	182	35.32	0.13	12.8	1.2	7.8	0.8
1	90	44.00	0.47	15.3	1.7	0.1	1.2	9	183	44.87	0.12	15.3	1.0	9.7	0.8
1	91	28.56	0.03	9.5	1.0	0.2	1.0	9	184	43.77	0.12	15.2	1.0	8.5	0.8
1	95	24.87	0.15	8.7	1.7	1.1	1.1	9	186	30.20	0.08	10.2	1.4	6.3	1.0
1	96	32.28	0.23	10.8	1.0	1.1	0.9	9	187	27.44	0.04	8.4	1.2	6.0	0.9
1	97	13.67	0.11	4.9	1.2	3.5	0.9	9	191	14.39	0.03	5.3	1.1	3.1	0.8
1	99	8.16	0.08	2.4	1.5	6.4	0.9	9	192	14.58	0.07	4.7	1.0	3.3	0.8
1	100	30.66	0.21	9.8	1.1	2.4	0.8	9	227	35.70	0.19	12.5	1.0	7.5	0.9
1	116	6.89	0.01	2.9	1.2	5.6	0.8	9	229	20.60	0.09	7.9	1.2	4.0	1.0
1	117	50.04	0.27	17.1	1.1	0.1	0.8	9	230	15.69	0.06	4.9	0.9	4.2	1.0
1	118	11.24	0.04	4.8	1.1	4.8	0.8	9	232	10.47	0.04	3.4	1.0	4.0	0.9
3	67	33.35	0.08	11.5	1.3	1.7	1.2	15	269	11.04	0.02	4.0	1.1	4.8	0.6
3	86	16.32	0.05	6.2	1.1	2.1	1.0	15	270	16.96	0.06	5.6	0.9	4.2	0.6
3	277	10.28	0.02	3.2	1.1	2.5	0.6	15	271	129.27	4.65	44.3	3.0	1.4	1.5
3	278	26.97	0.09	8.8	0.9	2.0	0.6	15	272	17.23	0.09	5.0	0.9	4.2	0.6
3	285	22.60	0.23	7.7	1.4	1.7	0.9	15	273	13.96	0.03	4.3	1.1	5.7	0.7
3	286	28.97	0.09	9.9	0.9	1.6	0.8	15	274	21.37	0.08	7.4	0.8	2.2	0.5
3	289	13.41	0.08	4.7	1.0	1.7	0.8	15	275	84.12	1.16	28.9	2.2	0.9	1.4
3	290	10.25	0.08	3.5	1.4	2.1	1.0	15	276	21.10	0.07	6.2	0.9	4.4	0.6
8	101	27.86	0.19	10.4	1.4	1.8	0.9	21	233	11.83	0.05	4.7	1.3	1.2	1.0
8	102	22.95	0.13	8.7	1.2	1.2	0.9	21	234	17.32	0.04	5.8	1.3	1.5	1.0
8	103	39.81	0.25	13.7	1.0	3.6	0.8	21	235	23.94	0.04	8.0	1.0	0.9	0.9
8	104	19.06	0.13	5.8	1.1	0.6	0.8	21	236	37.00	0.27	11.8	1.8	0.6	1.2
8	119	34.02	0.17	11.9	1.2	1.2	0.9	21	237	47.00	3.14	16.6	1.9	0.9	1.1
8	120	40.19	0.33	13.4	1.1	4.6	0.9	21	238	24.90	0.11	8.9	1.2	1.7	0.9
8	121	24.37	0.08	7.8	1.3	1.8	0.8	21	264	18.01	0.04	5.7	1.2	2.5	0.7
8	122	15.00	0.10	4.7	1.0	1.0	0.9	21	265	27.43	0.06	9.0	0.9	0.9	0.6
8	123	33.17	0.13	10.8	1.3	3.0	0.9	21	266	44.35	0.05	15.1	1.4	1.5	0.8
8	125	52.96	0.38	17.6	1.3	3.8	0.8	21	267	143.83	1.23	47.0	2.4	2.2	1.1
8	126	40.19	0.25	13.3	1.2	2.5	0.7	21	268	41.28	0.41	13.2	1.4	1.5	0.8

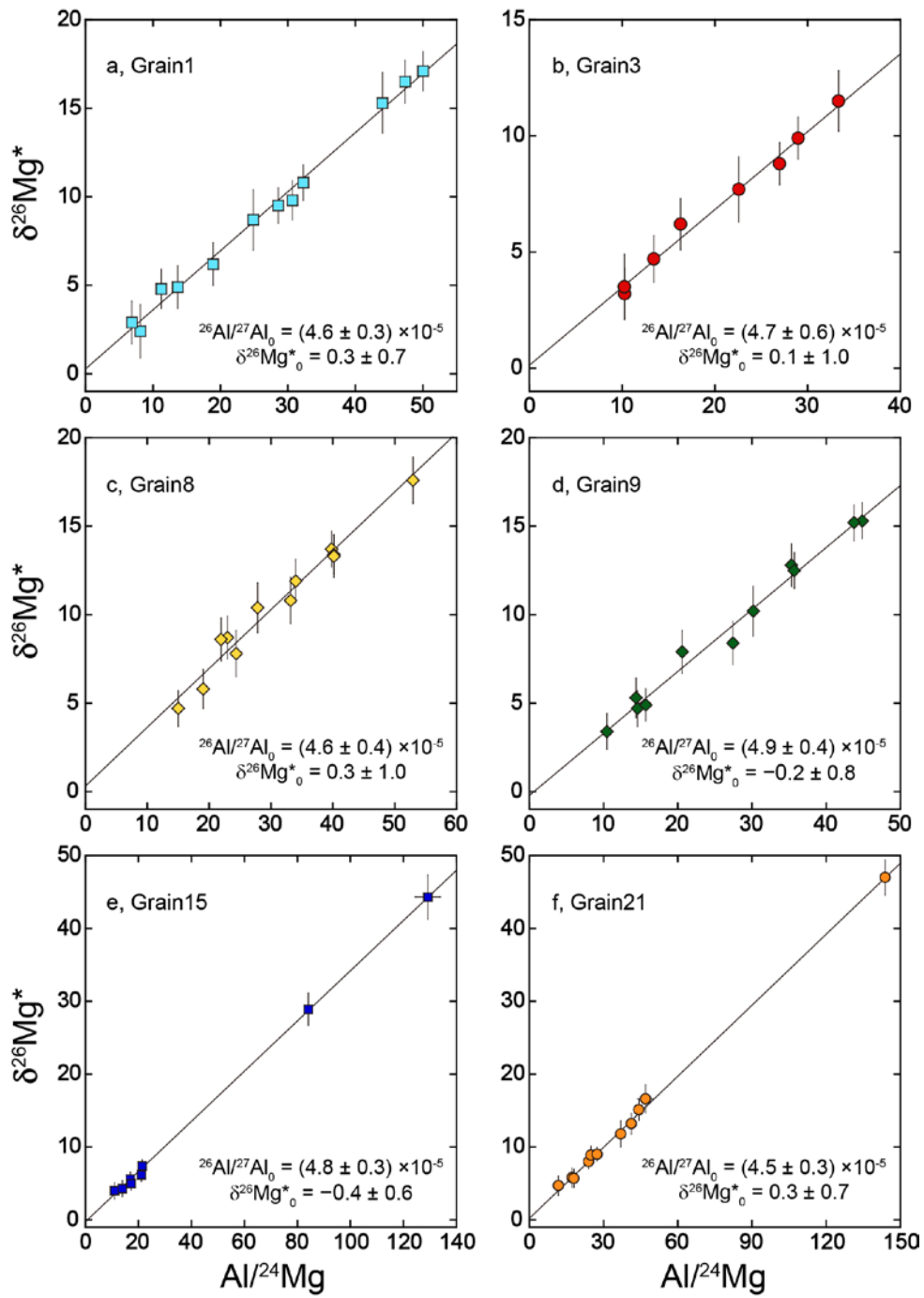


Figure 3.  $^{26}\text{Al}$ -Mg isochron diagram for the reversely zoned melilite crystals in V2-01. Errors are  $2\sigma$ .

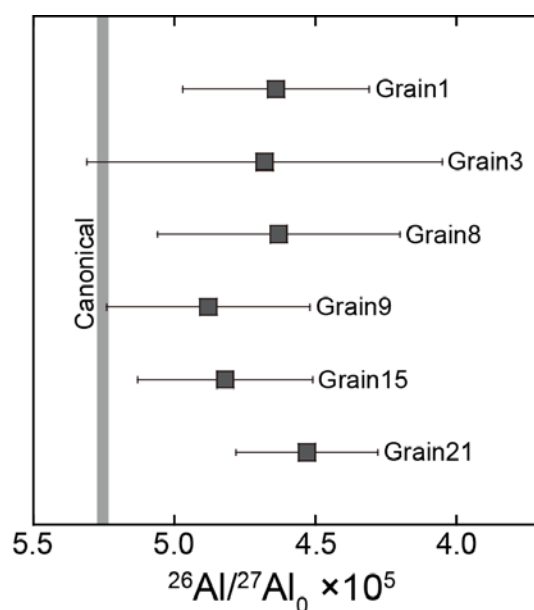


Figure 4. Comparisons of  $(^{26}\text{Al}/^{27}\text{Al})_0$  among the six grains. Errors are  $2\sigma$ . Canonical value of  $(^{26}\text{Al}/^{27}\text{Al})_0 = (5.252 \pm 0.019) \times 10^{-5}$  is from Larsen et al. (2011).

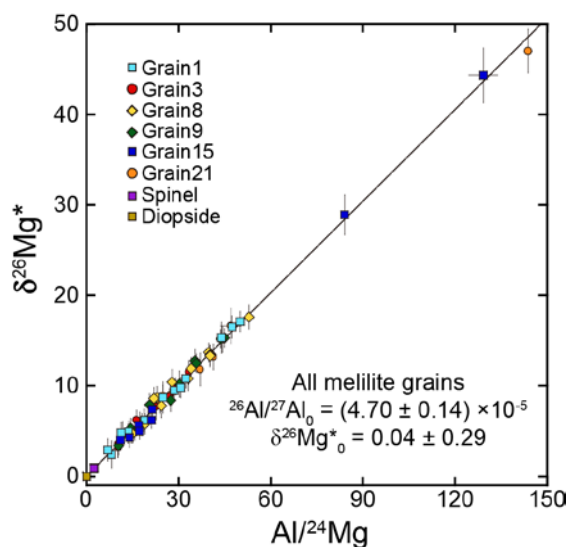


Figure 5.  $^{26}\text{Al}$ -Mg isochrons for all six reversely zoned melilite crystals in V2-01. Al-Mg isotopic compositions for spinel and diopside are plotted for comparison.

#### 5.1.4 Magnesium isotopic fractionations of reversely zoned melilite crystals

We have found variations for magnesium isotopic fractionations within the reversely zoned melilite crystals (Fig. 6). Three patterns of magnesium isotopic fractionation with the grains have been recognized. The  $\delta^{25}\text{Mg}$  values of the grains 1 and 15 tend to become small with decreasing åkermanite content (Figs. 6a and 6e). The

grains 3 and 21 show homogeneous  $\delta^{25}\text{Mg}$  values (Figs. 6b and 6f). The  $\delta^{25}\text{Mg}$  values of the grains 8 and 9 tend to become large with decreasing åkermanite content (Figs. 6c and 6d).

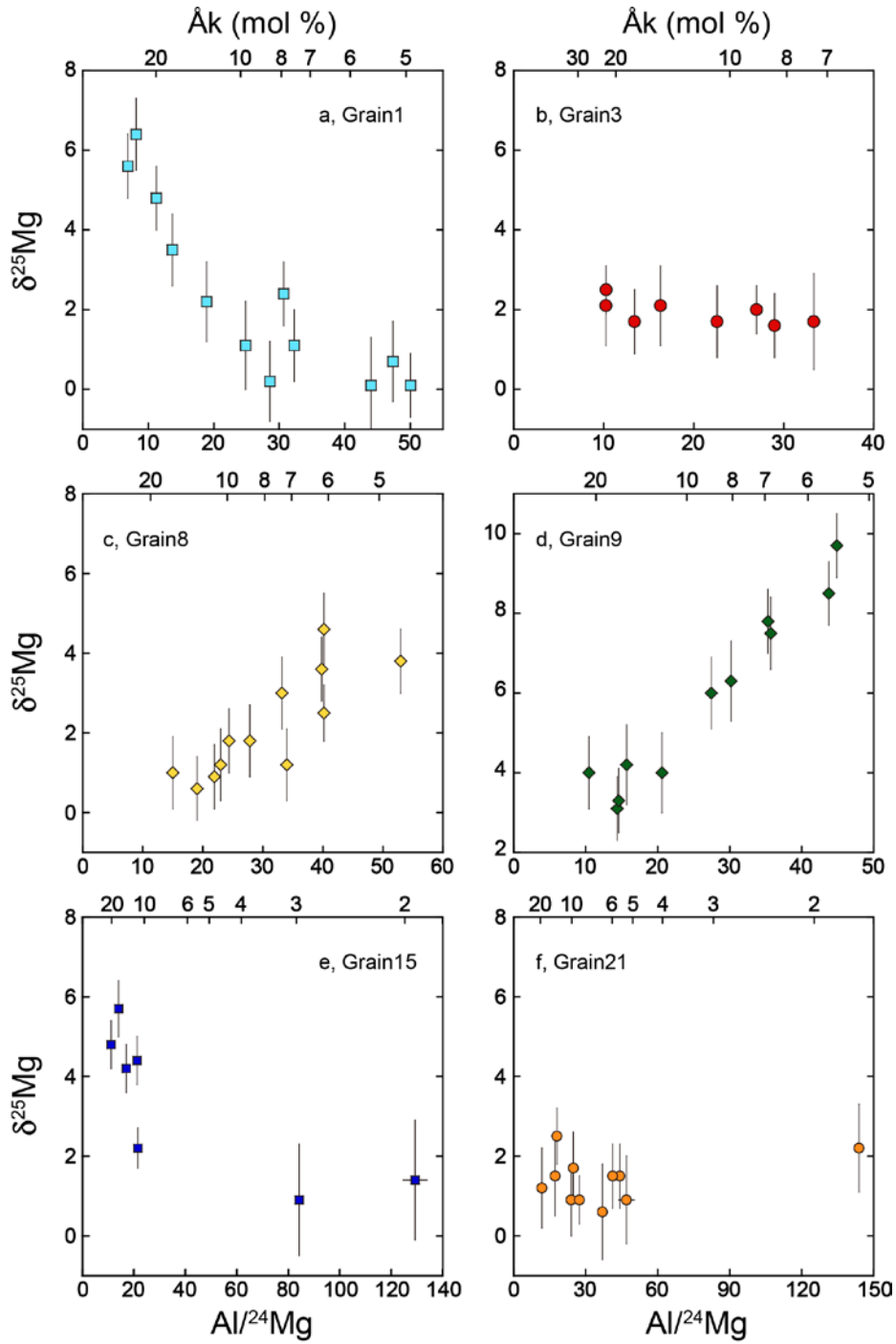


Figure 6. Relationships between the  $\delta^{25}\text{Mg}$  values and chemical compositions for each grain. Errors are  $2\sigma$ .

The grain 1 shows the magnesium isotopic compositions ranging from  $\delta^{25}\text{Mg} \sim 6$  to  $0\%$  along with reversely zoned crystal growth (Fig 6a). The  $\delta^{25}\text{Mg}$  became small gradually with increasing åkermanite content. The  $^{16}\text{O}$ -rich part of the grain 1 ( $< \text{Åk}6$ ) has a homogeneous  $\delta^{25}\text{Mg}$  value of  $\sim 0\%$ . The grain 3 shows the homogeneous  $\delta^{25}\text{Mg}$  value of  $\sim 2\%$  (Fig. 6b). The grain 8 shows the magnesium isotopic variations ranging from  $\delta^{25}\text{Mg} \sim 1$  to  $\sim 5\%$  (Fig. 6c). In the grain 8, the part having the chemical composition of  $> \text{Åk}8$  shows almost homogeneous  $\delta^{25}\text{Mg}$  value of  $\sim 1\%$  while  $< \text{Åk}8$  has variations of  $\delta^{25}\text{Mg}$  value ( $\sim 1$  to  $\sim 5\%$ ). The grain 9 shows the magnesium isotopic compositions ranging from  $\delta^{25}\text{Mg} \sim 3$  to  $\sim 10\%$  along with reversely zoned crystal growth (Fig. 6d). In the grain 9, the part having the chemical composition of  $> \text{Åk}10$  shows almost homogeneous  $\delta^{25}\text{Mg}$  value of  $\sim 4\%$  while  $< \text{Åk}10$  has variations of  $\delta^{25}\text{Mg}$  value ( $\sim 6$  to  $\sim 10\%$ ). The  $\delta^{25}\text{Mg}$  value of grain 9 gradually changes from  $\sim 6\%$  at  $\sim \text{Åk}9$  to  $\sim 10\%$  at  $\sim \text{Åk}6$ . The grain 15 shows the magnesium isotopic compositions ranging from  $\delta^{25}\text{Mg} \sim 6$  to  $\sim 1\%$  (Fig. 6e). The  $\delta^{25}\text{Mg}$  value seems to become small gradually with increasing åkermanite content as a same trend as the grain1. The  $^{16}\text{O}$ -rich part of the grain 1 ( $< \text{Åk}6$ ) has a homogeneous  $\delta^{25}\text{Mg}$  value of  $\sim 1\%$ . The grain 21 shows the homogeneous  $\delta^{25}\text{Mg}$  value of  $\sim 1\%$  (Fig. 6f). The properties for reversely zoned melilite crystals were summarized in Table 2.

Table 2. Summary of property for reversely zoned melilite crystals in V2-01.

Property	Grain 1	Grain 3	Grain 8	Grain 9	Grain 15	Grain 21
Grain size ( $\mu\text{m}$ )	200×400	250×300	150×200	300×600	80×150	80×120
Chemical zoning (Åk)	30 to 4	21 to 5	15 to 5	20 to 5	20 to 3	24 to 2
attached with W-L rim ?	yes	no	no	yes	yes	yes
O-isotope zoning ( $\Delta^{17}\text{O}$ )	-6 to -25	$\sim -5$	-13 to -20	-5 to -28	-7 to -16	-8 to -20
$\Delta^{17}\text{O}$ zoning displacement	Åk6	no change	Åk7	Åk8	Åk6	Åk5
$(^{26}\text{Al}/^{27}\text{Al})_0 \times 10^5$	$4.8 \pm 0.3$	$4.8 \pm 0.7$	$4.6 \pm 0.7$	$5.0 \pm 0.3$	$5.0 \pm 0.3$	$4.7 \pm 0.3$
$(\delta^{26}\text{Mg}^*)_0$	$0.3 \pm 0.7$	$0.1 \pm 1.0$	$0.4 \pm 1.6$	$-0.1 \pm 0.8$	$-0.5 \pm 0.6$	$0.3 \pm 0.7$
$\delta^{25}\text{Mg}$ zoning	0 to 6	$\sim 2$	1 to 5	4 to 10	1 to 6	$\sim 1$

### 5.1.5 Oxygen and magnesium isotopic compositions of the accessory minerals

The oxygen isotopic compositions of diopside, hibonite and spinel and the Al-Mg isotopic compositions of diopside and spinel in V2-01 are summarized in Tables 3 and 4, respectively. The oxygen isotopic compositions of these minerals show homogeneously  $^{16}\text{O}$ -rich compositions ( $\Delta^{17}\text{O} \sim -23\%$ ) that plotted on the CCAM line.

The magnesium isotopic compositions and Al/<sup>24</sup>Mg ratios of diopside and spinel seem to be plotted on the <sup>26</sup>Al-Mg isochron line for melilite (Fig. 5).

Table 3. Oxygen isotopic compositions of accessory minerals in V2-01.

mineral	$\delta^{17}\text{O}$	$2\sigma$	$\delta^{18}\text{O}$	$2\sigma$	$\Delta^{17}\text{O}$	$2\sigma$
CAI interior						
Hib	-46.8	2.1	-45.3	1.2	-23.2	2.0
Hib	-45.5	2.4	-41.7	1.5	-23.8	2.3
Hib	-45.2	1.9	-43.4	1.6	-22.6	1.7
Sp	-47.8	2.1	-44.7	1.6	-24.5	2.1
Sp	-46.1	1.8	-44.0	1.4	-23.3	1.6
W-L rim						
Di	-44.0	2.3	-42.3	1.4	-22.0	2.4
Di	-45.5	1.8	-42.0	1.4	-23.7	1.8
Sp	-45.8	2.1	-44.0	1.3	-22.9	2.0
Sp	-45.2	1.9	-42.9	1.7	-22.9	1.6

Di: diopside, Hib: hibonite, Sp: spinel

Table 4. Al/<sup>24</sup>Mg ratios and Mg isotopic compositions of accessory minerals in V2-01.

Mineral	Al/ <sup>24</sup> Mg	$2\sigma$	$\delta^{26}\text{Mg}^*$	$2\sigma$	$\delta^{25}\text{Mg}$	$2\sigma$
Di	0.01	0.00	-0.1	0.1	-1.5	0.4
Di	0.03	0.00	0.0	0.3	-1.3	0.5
Sp	2.42	0.05	0.8	0.2	0.1	0.1
Sp	2.48	0.05	0.9	0.2	0.3	0.1
Sp	2.43	0.05	1.0	0.3	0.0	0.1
Sp	2.44	0.05	1.0	0.2	-0.1	0.1
Sp	2.46	0.05	0.9	0.2	0.3	0.1

An: anorthite, Px: pyroxene, Ol: olivine, Sp: spinel

## 5.2 DISCUSSION

### 5.2.1 Formation processes of reversely zoned melilite crystals

#### 5.2.1.1 Grains of which $\delta^{25}\text{Mg}$ becomes small along with crystal growths

The oxygen isotopic compositions of grains 1 and 15 were changed from <sup>16</sup>O-poor to <sup>16</sup>O-rich and the  $\delta^{25}\text{Mg}$  became small along with the reversely zoned crystal growth. Oxygen and magnesium isotope exchanges in CAI minerals by solid-state diffusion in the solar nebula or on the parent body have been suggested (e.g., Itoh and

Yurimoto, 2003; Itoh et al., 2004; Fagan et al., 2004; Ito and Messenger, 2010; Simon et al., 2011). Thus, we should consider a possibility for the solid-state diffusion of oxygen and magnesium in reversely zoned melilite crystals as the origin of oxygen and magnesium isotopic variations. Katayama et al. (2012) showed that the oxygen isotopic zoning in grain 1 is not related to the distance from crystal rim but only to the crystal growth, indicating that oxygen self-diffusion in the melilite cannot form the oxygen isotopic variations in grain 1. The grain 15 has same relationships between the oxygen isotopic composition and the distance from crystal rim or the chemical composition. The magnesium self-diffusion in gehlenite is relatively slower than the oxygen self-diffusion at a temperature below ~1500 K (Yurimoto et al., 1989; Ito and Ganguly, 2009). These suggest that the magnesium isotopic variations in grains 1 and 15 cannot be explained by the solid-state diffusion in reversely zoned melilite crystals. The well-correlated  $\delta^{26}\text{Mg}^*$  values and  $\text{Al}/^{24}\text{Mg}$  ratios of grains 1 and 15 (Figs. 3a and 3e) are also inconsistent with the partial exchange of magnesium isotopes after the solidification. Therefore, the grains 1 and 15 should preserve their original magnesium isotopic fractionation patterns during crystal growth.

MacPherson and Grossman (1984) showed that reversely zoned melilite crystals found in fluffy Type A CAIs can be explained by the condensation from a solar nebular gas during a period of decreasing pressure. The reversely zoned melilite crystals in V2-01 fluffy Type A CAI also seemed to be explained by the condensation from the solar nebular gas (Katayama et al., 2012). In contrast, Grossman et al. (2002) suggested that the reversely zoned melilite crystal could also be formed by the crystallization from incomplete melt with melt evaporation. They predicted the magnesium isotopes of reversely zoned melilite formed by such process would have significantly enriched  $\delta^{25}\text{Mg}$  at the gehlenitic side of crystal. However, the grains 1 and 15 have depleted  $\delta^{25}\text{Mg}$  at the gehlenitic side of crystal (Figs 6a and 6e), which are inconsistent with the formation of reverse zoning by crystallization from incomplete melt with melt evaporation (Grossman et al., 2002). Therefore, the grains 1 and 15 were likely formed by the condensation from the solar nebular gas as suggested by Katayama et al. (2012). The magnesium isotopic variations in grains 1 and 15 may correspond to the change of magnesium isotopic compositions of surrounding nebular gas from which the grains were condensed. On the other hand, the pressure of surrounding nebular gas may be decreased during the condensation (MacPherson and Grossman, 1984). In summary, the oxygen isotopic compositions of surrounding nebular gas were changed from  $^{16}\text{O}$ -poor to  $^{16}\text{O}$ -rich while the  $\delta^{25}\text{Mg}$  became small, and the pressure was decreased, during the condensation of grains 1 and 15. The  $^{16}\text{O}$ -rich gehlenitic parts of grains 1 and 15

showed homogeneous  $\delta^{25}\text{Mg}$  of  $\sim 0$  or  $\sim 1$ , respectively, indicating that the  $^{16}\text{O}$ -rich nebular gaseous reservoir had nearly solar  $\delta^{25}\text{Mg}$  at their formation.

### 5.2.1.2 Grains with constant $\delta^{25}\text{Mg}$

The grains 3 and 21 showed the homogeneous  $\delta^{25}\text{Mg}$  of  $\sim 2$  and  $\sim 1$ , respectively (Figs. 6b and 6f). As similar to the case of grains 1 and 15 discussed in the previous section 4.2.1.1, the grains 3 and 21 showed no significantly enriched  $\delta^{25}\text{Mg}$  at the gehlenite-rich side of crystal, indicating that they were not formed by the crystallization from incomplete melt with melt evaporation but may be formed by the condensation from the solar nebular gas.

The oxygen isotopic compositions for grain 3 were homogeneously  $^{16}\text{O}$ -poor ( $\Delta^{17}\text{O} \sim -5\%$ ) while those for grain 21 showed the variations ranging from  $\Delta^{17}\text{O} \sim -8$  to  $-20\%$  and changing from  $^{16}\text{O}$ -poor to  $^{16}\text{O}$ -rich along with the reverse zoning. The oxygen and magnesium isotopic variations in grains 3 and 21 suggest that the grain 3 was formed in a homogeneous  $^{16}\text{O}$ -poor nebular gaseous reservoir having nearly solar  $\delta^{25}\text{Mg}$  while the grain 21 was formed in a nebular gas changing from  $^{16}\text{O}$ -poor to  $^{16}\text{O}$ -rich and having nearly solar  $\delta^{25}\text{Mg}$ .

### 5.2.1.3 Grains of which $\delta^{25}\text{Mg}$ becomes large along with crystal growths

The grains 8 and 9 have enriched  $\delta^{25}\text{Mg}$  at the gehlenitic side of crystal (Figs 6c and 6d). The formation of grains 8 and 9 also seems to be explained by the condensation from solar nebular gas. If they were formed by the condensation, the  $\delta^{25}\text{Mg}$  of solar nebular gas surrounding grains 8 and 9 became large during their crystal growths, which is opposite change to that for the grains 1 and 15. However, the relationships between  $\delta^{25}\text{Mg}$  values and chemical compositions for grains 8 and 9 (Figs 6c and 6d) are indeed consistent with the formation of reversely zoned melilite crystal by the crystallization from evaporating melt (Grossman et al., 2002). We thus also explore the model for crystallization from evaporating melt as the formation processes of the reversely zoned melilite crystals, the grains 8 and 9.

The melt evaporation causes loss of magnesium and silicon relative to more refractory aluminum and calcium, which results that the magnesium and silicon isotopic compositions for the residual melt become heavier than those for the precursor. Laboratory evaporation experiments showed that the isotopic fractionation of the melt follows the Rayleigh law (Richter et al., 2007; Mendybaev et al., 2013), and the equation was written as  $R/R_0 = f^{(\alpha-1)}$ , where  $R$  is  $^{25}\text{Mg}/^{24}\text{Mg}$  in the residual melt,  $R_0$  is  $^{25}\text{Mg}/^{24}\text{Mg}$  of the melt before evaporation,  $f$  is the fraction of magnesium remaining in

the residual melt, and  $\alpha$  is the kinetic isotope fractionation factor. Richter et al. (2007) determined the kinetic isotope fractionation factor,  $\alpha$ , for magnesium from the CAI-melt in vacuum at various temperature conditions. The relationship between the magnesium isotope fractionation and the fraction of magnesium remaining in the residual melt at given temperature can be calculated.

The chemical compositions for grains 8 and 9 were ranged within  $\text{Åk5-20}$ . According to the phase diagram (Osborn and Schairer, 1941), the temperature of melting would be higher than  $\sim 1480$  °C and lower than  $\sim 1560$  °C, because 1480 °C and 1560 °C are the solidus temperature of  $\text{Åk20}$  and  $\text{Åk5}$ , respectively. We use the kinetic isotope fractionation factor of  $\alpha = 0.98822$  at 1600 °C (Richter et al., 2007) that is the lowest experimental temperature they applied. Observed magnesium isotope fractionations for the grains 8 and 9 were  $\sim 4\%$  and  $\sim 6\%$  in  $\delta^{25}\text{Mg}$ , respectively (Table 1, Figs 6c and 6d). The fraction of magnesium remaining in the residual evaporating melt can be calculated using the kinetic isotope fractionation factor of  $\alpha = 0.98822$  and the magnesium isotope fractionation ( $\sim 4\%$  and  $\sim 6\%$  in  $\delta^{25}\text{Mg}$ ). The fractions of magnesium remaining in the residual melt for grains 8 and 9 are estimated to be  $\sim 71\%$  and  $\sim 60\%$ , respectively. According to the temperature dependence of kinetic fractionation factor inferred by Richter et al. (2007), the difference of temperature between 1600 °C and  $\sim 1480$  to  $\sim 1560$  °C may cause the change of less than 5% for the fraction of magnesium remaining in the residual melt, which is negligible for the discussion here. The part of grains 8 with the magnesium isotopic fractionations of  $\sim 4\%$  in  $\delta^{25}\text{Mg}$  is  $\text{Al}^{24}\text{Mg} \sim 40$  (Figs. 6c) while the part of grains 9 with the magnesium isotopic fractionations of  $\sim 6\%$  in  $\delta^{25}\text{Mg}$  is  $\text{Al}^{24}\text{Mg} \sim 45$  (Figs. 6c). When the fractions of magnesium remaining in the residual melt were  $\sim 71\%$  at grain 8 and  $\sim 60\%$  at grain 9 at the evaporative melting, the melt composition before the evaporation would be  $\text{Al}^{24}\text{Mg} \sim 28$  for grain 8 and  $\text{Al}^{24}\text{Mg} \sim 27$  for grain 9, respectively, which correspond to the chemical compositions of melted melilite. These inferred chemical compositions are comparable with the chemical compositions where  $\delta^{25}\text{Mg}$  starts to become large (Figs. 6c and 6d), indicating that the grains 8 and 9 already had reverse zoning before evaporative melting and subsequently experienced incomplete melting with melt evaporation and crystallization to overgrow as the reverse zoning on the relict. This formation process is consistent with the model for the crystallization of reverse zoning from evaporating melt suggested by Grossman et al. (2002) who concluded that incomplete melting and overgrowth were necessary to explain the chemical and magnesium isotopic variations of reversely zoned melilite crystals in fluffy Type A CAIs. In both grains 8 and 9, the  $\delta^{25}\text{Mg}$  values seem to be gradually changed correlated

with the  $\text{Al}^{24}\text{Mg}$  ratio, suggesting that the melts were evaporating during their crystal growths.

We note that the kinetic fractionation factor,  $\alpha$ , depends on the chemical composition of starting melt (Mendybaev et al. 2013). In the evaporation experiments by Richter et al. (2007), the starting composition was  $\text{MgO} \sim 11$  wt%, while reversely zoned melilite crystals in fluffy Type A CAIs have the composition with  $\text{MgO} < 5$  wt%. However, there are no experimental studies at such chemical composition. We thus used the value of  $\alpha$  from Richter et al. (2007), although the evaporation experiments using the melt having melilite composition is necessary to discuss more accurately.

The oxygen isotopic compositions of grains 8 and 9 became  $^{16}\text{O}$ -rich from  $\sim\text{\AA}k7$  ( $\text{Al}^{24}\text{Mg} \sim 35$ ) at grain 8 and from  $\sim\text{\AA}k8$  ( $\text{Al}^{24}\text{Mg} \sim 30$ ) at grain 9, respectively, along with the reverse zoning. These chemical compositions at starting to change the oxygen isotopic compositions were more little gehlenitic (i.e., higher  $\text{Al}^{24}\text{Mg}$ ) than that for  $\delta^{25}\text{Mg}$  ( $\text{Al}^{24}\text{Mg} \sim 30$  and  $\sim 25$  for grains 8 and 9, respectively; Figs. 6c and 6d). These suggest that the oxygen isotopic compositions of surrounding gas for grains 8 and 9 were changed from  $^{16}\text{O}$ -poor to  $^{16}\text{O}$ -rich and the oxygen isotope exchange between gas and melt were occurring during the crystallization from evaporative melt, or that the melting events occurred under the  $^{16}\text{O}$ -rich nebular gas condition and the gradual change of oxygen isotopic composition reflects the exchange rate of oxygen isotopes between gas and melt.

### 5.2.2 Time duration for the formation of reversely zoned melilite crystals

As discussed in section 5.2.1.1 and 5.2.1.2, the grains 1, 3, 15 and 21 were likely formed by the condensation from solar nebular gas. If the crystal growth of these condensed grains were enough slow, the gehlenitic sides would have depleted  $\delta^{26}\text{Mg}^*$  relative to the isochron lines in the  $^{26}\text{Al}$ -Mg isochron diagrams, due to the evolution of  $^{26}\text{Al}$ -Mg system of solar nebular gas. However, Fig. 3 shows that  $\delta^{26}\text{Mg}^*$  at gehlenitic sides for these grains are not systematically depleted relative to the isochron slopes, which indicates that they were formed within the time durations corresponding to errors of initial  $(^{26}\text{Al}/^{27}\text{Al})_0$  for each isochron. The time durations for formation of the grains are calculated to be shorter than 0.15 Myr for grain 1, 0.28 Myr for grain 3, 0.13 Myr for grain 15, and 0.12 Myr for grain 21, respectively. Therefore, the condensation of reversely zoned melilite crystals (grains 1, 3, 15 and 21) from solar nebular gas occurred within the time duration for 0.12-0.28 Myr. The data of grain 21 indicates that the time scale of oxygen isotope change for the solar nebular gas from  $^{16}\text{O}$ -poor to  $^{16}\text{O}$ -rich was less than 0.12 Myr.

As discussed in section 5.2.1.3, the grains 8 and 9 could be explained by both the condensation and the crystallization from the evaporating melt. If they were formed by the condensation, the time durations for formation of them are calculated by the same procedure as other grains to be shorter than 0.20 Myr for grain 8, 0.16 Myr for grain 9. If on the other hand they were formed by the crystallization from the evaporating melt, two isochrons both for the relict part and the melted part could be determined to test the time duration. For the grain 8, the relict part could show an initial value of  $(^{26}\text{Al}/^{27}\text{Al})_0 = (6.2 \pm 1.5) \times 10^{-5}$  and  $(\delta^{26}\text{Mg}^*)_0 = -2.1 \pm 2.5\%$ , and the melted part could show an initial value of  $(^{26}\text{Al}/^{27}\text{Al})_0 = (4.5 \pm 1.1) \times 10^{-5}$  and  $(\delta^{26}\text{Mg}^*)_0 = 0.5 \pm 3.2\%$ . For the grain 9, the relict part could show an initial value of  $(^{26}\text{Al}/^{27}\text{Al})_0 = (5.2 \pm 1.0) \times 10^{-5}$  and  $(\delta^{26}\text{Mg}^*)_0 = -1.1 \pm 2.6\%$ , and the melted part could show an initial value of  $(^{26}\text{Al}/^{27}\text{Al})_0 = (6.0 \pm 2.1) \times 10^{-5}$  and  $(\delta^{26}\text{Mg}^*)_0 = -1.3 \pm 2.3\%$ . For both the grains 8 and 9, the initial values of  $(^{26}\text{Al}/^{27}\text{Al})_0$  and  $(\delta^{26}\text{Mg}^*)_0$  for the relict and melted parts are indistinguishable each other. Therefore, the time durations for formation of grains 8 and 9 from the formation of precursor grain and subsequent melting and crystallization could be shorter than 0.20 Myr for grain 8, 0.16 Myr for grain 9, if they were formed by the crystallization from the evaporating melt.

### 5.2.3 Interpretation of initial $(^{26}\text{Al}/^{27}\text{Al})_0$ for melilite in V2-01

The initial  $(^{26}\text{Al}/^{27}\text{Al})_0$  values for each grain in V2-01 were systematically distinct from the canonical, Solar System initial  $(^{26}\text{Al}/^{27}\text{Al})_0 = (5.252 \pm 0.019) \times 10^{-5}$  (Larsen et al., 2011) (Fig. 4). The systematic shift for  $(^{26}\text{Al}/^{27}\text{Al})_0$  values due to problems on analysis of  $\text{Al}/^{24}\text{Mg}$  ratio could be one possibility to explain the discrepancy of initial  $(^{26}\text{Al}/^{27}\text{Al})_0$ . We use synthetic melilite glass as the standard with  $\text{Al}/^{24}\text{Mg} = 3.82$  for the relative sensitive factor (RSF) for aluminium and magnesium. If the RSF were shifted at  $\sim 11\%$  level, the discrepancy of  $(^{26}\text{Al}/^{27}\text{Al})_0$  can be produced. However, Kita et al. (2012) showed that the RSFs for aluminium and magnesium among melilites with  $\text{Al}/^{24}\text{Mg} = \sim 1$  to  $\sim 13$  were not systematically changed along with the change of  $\text{Al}/^{24}\text{Mg}$ , suggesting that the discrepancy of initial  $(^{26}\text{Al}/^{27}\text{Al})_0$  for the V2-01 melilite from the canonical may not be produced by the inaccurate RSF. Therefore, the problem on analysis of  $\text{Al}/^{24}\text{Mg}$  ratio is excluded.

The difference of the initial  $(^{26}\text{Al}/^{27}\text{Al})_0$  values between the all melilite and the canonical corresponds to be the age difference of  $0.12 \pm 0.03$  Myr. If the melilite grains in V2-01 were formed from the solar nebular gas which evolved from the canonical with closed system, the melilite grains in V2-01 were formed at  $0.12 \pm 0.03$  Myr after the canonical CAI formation. If the  $^{26}\text{Al}$  was heterogeneously distributed in the

CAI-forming region, formation age of V2-01 melilite could not be estimated.

The Al-Mg isotopic compositions for spinel and diopside were plotted on the melilite isochron (Fig. 6). However, we cannot determine whether these minerals were formed at the same time as the melilite because both the error of  $(\delta^{26}\text{Mg}^*)_0$  for the melilite isochron and the those of  $\delta^{26}\text{Mg}^*$  for diopside are too large to be compared. The oxygen isotopic compositions for spinel and hibonite were homogeneously  $^{16}\text{O}$ -rich ( $\Delta^{17}\text{O} \sim -23\text{‰}$ ) and these minerals enclosed by melilite crystals were formed before the melilite condensation, suggesting that  $^{16}\text{O}$ -rich environment was present before the condensation of  $^{16}\text{O}$ -poor melilite.

#### 5.2.4 Formation of V2-01 fluffy Type A CAI

In the grains 1, 15, and 21, highly gehlenitic and  $^{16}\text{O}$ -rich compositions were only observed at the W-L rim side of grains and the changes of oxygen isotopic compositions from  $^{16}\text{O}$ -poor to  $^{16}\text{O}$ -rich started from Åk5-6. On the other hand, the  $^{16}\text{O}$ -rich composition was not observed in the grain 3, which was not attached with the W-L rim. These indicate that the condensation overgrowth of melilite with highly gehlenitic and  $^{16}\text{O}$ -rich composition on  $^{16}\text{O}$ -poor melilite crystals occurred after the accumulation of the melilite crystals to form the precursor of V2-01 fluffy Type A CAI in the solar nebula. The continuous chemical zoning pattern between the grain 1 and the adjacent grain (Fig. 2a) is consistent with this scenario. The grains 1 and 15 have the variations for  $\delta^{25}\text{Mg}$ , of which the  $\delta^{25}\text{Mg}$  becomes small with decreasing åkermanite content (Figs. 6a and 6e). In contrast, the  $\delta^{25}\text{Mg}$  for grains 3 and 21 were constant despite of variations for åkermanite content (Figs. 6b and 6f). These suggest that these melilite grains had grown in distinct environments of the solar nebula, and subsequently accumulated together in the solar nebula. The  $^{26}\text{Al}$ -Mg systematics indicates that the sequence of formation processes including the condensation of  $^{16}\text{O}$ -poor melilite, the accumulation of melilite crystals, and the condensation overgrowth of  $^{16}\text{O}$ -rich melilite occurred within 0.12 Myr.

If the grains 8 and 9 were formed by the crystallization from the evaporating melt, the heating temperature was  $\sim 1480$  to  $\sim 1560$  °C as discussed in section 5.2.1.3. In contrast, the condensation temperatures for grains 1, 3, 15, and 21 were  $\sim 1120$  to  $\sim 1150$  °C at  $P_{\text{total}} = 10^{-4}$  atm or  $\sim 1200$  to  $\sim 1230$  °C at  $P_{\text{total}} = 10^{-3}$  atm, from the solar composition gas, according to the phase diagram (Yoneda and Grossman, 1995). The heating temperature for melting of grains 8 and 9 was significantly higher than that for condensation of grains 1, 3, 15, and 21, indicating they were formed in distinct environments in the solar nebula and accumulated together. On the other hand, if the

grains 8 and 9 were formed by the condensation, the  $\delta^{25}\text{Mg}$  of nebular gas surrounding grains 8 and 9 should be distinct from those surrounding grains 1, 3, 15, and 21, indicating they also were formed in distinct environments in the solar nebula and accumulated together.

A Type A CAI from the Efremovka CV3, HKE 01, is composed of two domains, each of which has grown in distinct nebular reservoirs for oxygen isotopic composition, and temperature and/or pressure (Kawasaki et al., 2012). The formation of HKE 01 seems to be similar to that of V2-01. The crystals and domains were formed separately in the solar nebula, and they accumulated together to form the CAIs. For V2-01, the  $^{26}\text{Al}$ -Mg systematics indicates that these formation processes occurred during the period within 0.28 Myr, although the age of W-L rim formation remains controversial.

### **5.2.5 Implication for astrophysical setting of Type A CAI-forming region**

Katayama et al. (2012) proposed that the change of oxygen isotopic composition of surrounding nebular gas from  $^{16}\text{O}$ -poor to  $^{16}\text{O}$ -rich during crystal growth of reversely zoned melilite crystals corresponds to the inner edge region of the solar nebula where  $^{16}\text{O}$ -rich solar and  $^{16}\text{O}$ -poor planetary gases are encountered and mixed (Yurimoto et al., 2008). The environmental change around the melilite crystals might occur by the fluctuation of the inner edge of the solar nebula (Shu et al., 1997; Itoh and Yurimoto, 2003) or the radial transportation of grains (Ciesla, 2007; 2009). Similar nebular environments were suggested based on measurements of oxygen isotopic and chemical zoning for intra- and inter- melilite crystals in other Type A CAIs from the Efremovka and Allende CV3 (Kawasaki et al., 2012; Park et al., 2012). As discussed in the section 5.2.2, the oxygen isotope change of solar nebular gas from  $^{16}\text{O}$ -poor to  $^{16}\text{O}$ -rich occurred within 0.12 Myr, implying that the time scale for fluctuation of the inner edge of solar nebula or radial transportation to change the oxygen isotopic composition of the gas surrounding the melilite grains was within 0.12 Myr.

The oxygen isotopic compositions of nebular gas surrounding the grains 1 and 15 were changed from  $^{16}\text{O}$ -poor to  $^{16}\text{O}$ -rich where the  $\delta^{25}\text{Mg}$  became small to be nearly solar  $\delta^{25}\text{Mg}$  with decreasing pressure, as discussed in the section 5.2.1.1. Course-grained CAIs have various  $\delta^{25}\text{Mg}$  values and many of them show large  $\delta^{25}\text{Mg}$  of up to  $\sim 12\%$  (e.g., Bizzarro et al., 2004; Larsen et al., 2011). The inferred  $\delta^{25}\text{Mg}$  of the surrounding gas for the grains 1 and 15 ( $\delta^{25}\text{Mg} \sim 6$ ) could be produced by the vaporization of such large  $\delta^{25}\text{Mg}$  CAIs at the region with high dust-to-gas ratio, which is consistent with the formation in the inner edge region of solar nebula where the dust

component is highly enriched relative to the gaseous component (Shu et al., 1997; Itoh et al., 2003). The grains 1 and 15 probably condensed from such CAI vapor there. Both the change of oxygen isotopic compositions from  $^{16}\text{O}$ -poor to  $^{16}\text{O}$ -rich and the change of  $\delta^{25}\text{Mg}$  from large ( $\delta^{25}\text{Mg} \sim 6$ ) to nearly solar values ( $\delta^{25}\text{Mg} \sim 0$  or  $\sim 1$ ) can be explained by the mixing between the CAI vapor and  $^{16}\text{O}$ -rich solar gas.

The  $\delta^{25}\text{Mg}$  values of gas surrounding grains 3 and 21 were distinct from those surrounding grains 1 and 15. On the other hand, as discussed in 4.1.3, it is inferred that the heating temperature of melting for the grains 8 and 9 was significantly higher than condensation temperature for other grains, or that the  $\delta^{25}\text{Mg}$  values of gas surrounding grains 8 and 9 were distinct from those surrounding other grains. These differences of heating temperature or  $\delta^{25}\text{Mg}$  values can also be explained by the consequence of the model for the formation in the inner edge region of the solar nebula, based on the fact that the ambient temperature for the melilite grains could be varied by heliocentric distance and dust-to-gas ratio and the fact that oxygen and magnesium isotopic compositions could have variations due to the difference of mixing proportion between the CAI vapor and  $^{16}\text{O}$ -rich solar gas. The relationships among the ambient temperature, the oxygen isotopic composition, and the  $\delta^{25}\text{Mg}$  could always varied by the cyclic fluctuation of the inner edge of the solar nebula (Shu et al., 1997; Itoh and Yurimoto et al., 2003). In summary, each reversely zoned melilite crystals were locally formed at distinct environment in the early Solar System, and accreted together to form V2-01.

### 5.3 Conclusions

We have measured the magnesium isotopic compositions and  $\text{Al}/^{24}\text{Mg}$  ratios of six reversely zoned melilite crystals in V2-01 with changes of oxygen isotopic compositions from  $^{16}\text{O}$ -poor to  $^{16}\text{O}$ -rich along with crystal growths as indicated by Katayama et al. (2012). The magnesium isotopic fractionation patterns for reversely zoned melilite crystals can be categorized as three types; (1)  $\delta^{25}\text{Mg}$  was constant despite of variation for  $\text{Al}/^{24}\text{Mg}$  (grains 3 and 21), (2)  $\delta^{25}\text{Mg}$  became small along with crystal growth of reverse zoning (grains 1 and 15), and (3)  $\delta^{25}\text{Mg}$  became large along with crystal growth of reverse zoning (grains 8 and 9). The oxygen and magnesium isotopic and chemical zoning indicates that the grains 3 and 21 were grown by the condensation from the nebular gas changing from  $^{16}\text{O}$ -poor to  $^{16}\text{O}$ -rich of which  $\delta^{25}\text{Mg}$  became smaller, while the grains 1 and 15 were condensed from the nebular gas changing from  $^{16}\text{O}$ -poor to  $^{16}\text{O}$ -rich with constant  $\delta^{25}\text{Mg}$ . The oxygen isotope change of solar nebular gas from  $^{16}\text{O}$ -poor to  $^{16}\text{O}$ -rich occurred at the time scale of less than 0.12 Myr. In contrast, the grains 8 and 9 may have been formed by incomplete melting of reversely

zoned melilite crystal and crystallization from partial melting melt with melt evaporation in the  $^{16}\text{O}$ -rich nebular gas or formed by the condensation from the nebular gas. The formation environments of reversely zoned melilite crystals in V2-01 may correspond to the inner edge region of the solar nebula having high dust-to-gas ratio where  $^{16}\text{O}$ -rich solar and  $^{16}\text{O}$ -poor planetary gases are encountered and mixed and (Yurimoto et al., 2008). The single isochrons for each reversely zoned melilite crystal could readily be defined and the initial  $(^{26}\text{Al}/^{27}\text{Al})_0$  for each grain was the same within the error. The  $^{26}\text{Al}$ -Mg systematics indicates that formation of these grains occurred at  $0.12 \pm 0.03$  Myr after the canonical CAI formation, and the time durations of formation were less than 0.12-0.28 Myr. Our study shows that each reversely zoned melilite crystals were locally formed at distinct environment in the early Solar System within 0.28 Myr, and accreted together to form V2-01.

## 6. Implications and future works

From the evidences of chemical and oxygen isotopic distributions, HKE 01, the Type A CAI from Efremovka CV3 (Chapter 3; Kawasaki et al., 2012) and V2-01, the fluffy Type A CAI from Vigarano CV3 (Katayama et al., 2012; Chapter 5) were likely formed at similar environments in the inner edge region of the solar nebula where  $^{16}\text{O}$ -rich solar and  $^{16}\text{O}$ -poor planetary gases are encountered and mixed (Yurimoto et al., 2008). HKE 01 is composed of two domains, each of which has grown in distinct nebular reservoirs for oxygen isotopic composition, and temperature and/or pressure. The sizes of these domains are orders of centimeters or millimeters and these domains are composed of numerous melilite crystals with sizes of few tens of micrometers. On the other hand, each melilite crystal in V2-01 was individually formed in the early Solar System, and accreted together. The sizes of these melilite crystals are orders of sub-millimeters. The  $^{26}\text{Al}$ -Mg systematics indicates that the formation of melilite crystals in V2-01 occurred at  $0.12 \pm 0.03$  Myr after the canonical CAI formation, and the time durations of their formation were less than 0.12-0.28 Myr. On the other hand, there have been no Al-Mg isotope measurements for melilite of HKE 01 yet. For comparison with V2-01, the  $^{26}\text{Al}$ -Mg systematics of HKE 01 should be investigated in the future work. The chronological study of melilite crystals with different sizes in the Type A CAIs may have a potential for understanding the dust size evolution in the CAI-forming region. Such attempt has not been studied yet.

Recently, the heterogeneity in the initial abundance of  $^{26}\text{Al}$  in the early Solar System has been inferred and is one of the most important matters in the field of cosmochemistry (e.g., Larsen et al., 2011; Krot et al., 2012; Bizzarro et al., 2014). If the distribution of  $^{26}\text{Al}$  was significantly heterogeneous, the  $^{26}\text{Al}$ -Mg system could not be an accurate chronometer for the early Solar System. For example, the inferred ages of spinel in EK1-04-2 (Chapter 4) and melilite crystals in V2-01 (Chapter 5) would not be valid because these ages were estimated with the assumption that the  $^{26}\text{Al}$ -Mg systems of these minerals were evolved from the canonical  $(^{26}\text{Al}/^{27}\text{Al})_0$ . The comparative study between the  $^{26}\text{Al}$ -Mg system and other clocks (e.g.,  $^{10}\text{Be}$ -B,  $^{41}\text{Ca}$ -K,  $^{182}\text{Hf}$ -W, and Pb-Pb systems) can test the homogeneity or heterogeneity for initial abundance of  $^{26}\text{Al}$  distribution in the early Solar System (e.g., Holst et al., 2013; Bizzarro et al., 2014). However, to probe the homogeneity may be much more difficult than to discuss the heterogeneity, even if the focus were made only for the CAI-forming region. Other approaches to determine the accurate ages are necessary for the  $^{26}\text{Al}$ -Mg system.

A most plausible attempt at present to determine the heating ages of CAIs is

probably the  $^{26}\text{Al}$ -Mg systematics of CAIs that underwent multiple melting events. When the  $^{26}\text{Al}$ -Mg systematics was the closed system for each CAI, the age differences of heating events for them can be determined using multi-internal  $^{26}\text{Al}$ -Mg isochrons. Indeed, the  $^{26}\text{Al}$ -Mg systematics of EK1-04-2 (Chapter 4) is a good example for determinations of the age differences using multi-internal  $^{26}\text{Al}$ -Mg isochrons. For EK1-04-2, the age difference between the precursor CAI and later formed minerals with distinct oxygen isotopic compositions that crystallized from the partial melting melt has been estimated as at least 1.6 Myr, which is independent from the unresolved issue of heterogeneous  $^{26}\text{Al}$  distribution. This study strongly suggests that the transient heating events had occurred at least 1.6 Myr after the CAI formation regardless of the heterogeneous distributions of initial abundance for  $^{26}\text{Al}$ . The multiple melting events for EK1-04-2 may be related to the chondrule heating events because (1) the textures seem to correspond to those for Al-rich chondrules and experimental products that crystallized with relatively rapid cooling at faster than 100 °C/h (MacPherson and Huss, 2003; Tronche et al., 2007), (2) Al-rich chondrule components were accreted on the precursor CAI of EK1-04-2 before the second partial melting event and these events occurred probably in the chondrule-forming region, and (3) olivine and pyroxene in the core and these minerals in the mantle had indistinguishable  $\delta^{25}\text{Mg}$  values although the mantle was re-melted after the core formation and the melted coarse-grained CAIs usually have enriched  $\delta^{25}\text{Mg}$  values by the evaporative loss of magnesium during the melting and crystallization (e.g., Bullock et al., 2012; Kita et al., 2012; MacPherson et al., 2012; Paque et al., 2013). These infer that a chondrule heating event occurred at least 1.6 Myr after the CAI formation. The new chronological information from multi-internal  $^{26}\text{Al}$ -Mg isochrons of EK1-04-2 is consistent with single internal  $^{26}\text{Al}$ -Mg isochrons of compound CAI-chondrule objects from the Allende CV3 that suggest chondrule heating events probably occurred ~2 Myr after the formation of most CAIs with the assumption of the uniform  $^{26}\text{Al}$  distribution in the CAI and chondrule-forming regions (Krot et al., 2005, 2007). I suggest that it is better to determine such ages using multi-internal  $^{26}\text{Al}$ -Mg isochrons unless the problems on  $^{26}\text{Al}$  distribution would be resolved well. Such attempts to determine multi-internal  $^{26}\text{Al}$ -Mg isochrons were little investigated yet (Podosek et al., 1991; Hsu et al., 2000; MacPherson et al., 2012).

The absolute chronology using U-corrected Pb-Pb system has also determined the ages of CAI and chondrule formations (Connelly et al., 2012). The Pb-Pb dating by Connelly et al. (2012) showed that the age of CAIs are  $4567.30 \pm 0.30$  Myr and the chondrule formation started contemporaneously with CAIs and lasted ~3 Myr, which is also a consistent result with the  $^{26}\text{Al}$ -Mg chronology of EK1-04-2. However, the heating

ages of CAIs that underwent multiple melting events cannot be determined accurately by the bulk analyses because the melting events for coarse-grained CAIs often are the partial melting and crystallization processes and they have the isotopic disequilibrium states. Therefore,  $^{26}\text{Al-Mg}$  systematics using SIMS coordinated with oxygen isotope distributions and petrography like this study about EK1-04-2 is probably the best way to determine the chronological histories of the heating events for CAIs. I note that I would like to apply the  $^{26}\text{Al-Mg}$  systematics of multiple melting for various coarse-grained CAIs, in order to make the chronological table of heating events in the early Solar System, which may have a large impact for the determination of the heating sources in the early Solar System and the models for evolutions of the early Solar System and protoplanetary disks.

## **ACKNOWLEDGEMENTS**

I am indebted to Professor Hisayoshi Yurimoto. I am grateful to him for numerous valuable suggestions and his kind support throughout this work. I have learned many things in the field of cosmochemistry and mass spectrometry from him.

I thank to other members of my doctoral committee, Professor Takaya Nagai, Dr. Shogo Tachibana, and Dr. Junji Yamamoto for their advices and valuable comments.

I thank to Dr. N. Sakamoto and Dr. S. Itoh for their skillful help with SIMS measurements. They showed me how to measure the chemical and isotopic compositions using SIMS instruments. I also thank them for their helpful suggestion, discussions, and encouragements.

I am grateful to other staffs, students, and former members of Yurimoto Lab for many helpful suggestions and encouragements.

## REFERENCES

- Amelin Y., Krot A. N., Hutcheon I. D. and Ulyanov A. N. (2002) Lead isotopic ages of chondrules and Calcium-Aluminum-rich inclusions. *Science* **297**, 1678–1683.
- Aléon J., El Goresy A. and Zinner E. (2007) Oxygen isotopic heterogeneities in the earliest protosolar gas recorded in a meteoritic calcium-aluminum-rich inclusion. *Earth and Planetary Science Letters* **263**, 114–127.
- Aléon J., Krot A. N., McKeegan K. D., MacPherson G. J. and Ulyanov A. A. (2005) Fine-grained, spinel-rich inclusions from the reduced CV chondrite Efremovka: II. Oxygen isotopic compositions. *Meteoritics & Planetary Science* **40**, 1043–1058.
- Beckett J. R. and Stolper E. (1994) The stability of hibonite, melilite and other aluminous phases in silicate melts: implications for the origin of hibonite-bearing inclusions from carbonaceous chondrites. *Meteoritics* **29**, 41–65.
- Bizzarro M., Baker J. A. and Haack H. (2004) Mg isotope evidence for contemporaneous formation of chondrules and refractory inclusions. *Nature* **431**, 275–278.
- Bizzarro M., Olsen M., Itoh S., Kawasaki N., Schiller M., Bonal L. and Yurimoto H. (2014) Evidence for a reduced initial abundance of  $^{26}\text{Al}$  in chondrule forming regions and implications for the accretion timescales of protoplanets (abstract #5125). 77th Annual Meteoritical Society Meeting.
- Ciesla F. J. (2007) Outward transport of high-temperature materials around the midplane of the solar nebula. *Science* **318**, 613–615.
- Ciesla F. J. (2009) Two-dimensional transport of solids in viscous protoplanetary disks. *Icarus* **200**, 655–671
- Clayton R. N. (1993) Oxygen isotopes in meteorites. *Annual Review of Earth and Planetary Science* **21**, 115–149.
- Clayton R. N. and Mayeda T. K. (1999) Oxygen isotope studies of carbonaceous chondrites. *Geochimica et Cosmochimica Acta* **63**, 2089–2104.
- Clayton R. N., Onuma N., Grossman L. and Mayeda T. K. (1977) Distribution of the presolar component in Allende and other carbonaceous chondrites. *Earth and Planetary Science Letters* **34**, 209–224.
- Connelly J. N., Bizzarro M., Krot A. N., Nordlund Å., Wielandt D. and Ivanova M. A. (2012) The absolute chronology and thermal processing of solids in the solar Protoplanetary disk. *Science* **338**, 651–655.

- Davis A. M., Richter F. M., Mendybaev R. A., Janney P. E., Wadhwa M. and McKeegan K. D. (2005) Isotopic mass fractionation laws and the initial solar system  $^{26}\text{Al}/^{27}\text{Al}$  ratio (abstract #2334). 36th Lunar and Planetary Science Conference.
- Fagan T. J., Guan Y. and MacPherson G. J. (2007) Al-Mg isotopic evidence for episodic alteration of Ca-Al-rich inclusions from Allende. *Meteoritics & Planetary Science* **42**, 1221–1240.
- Fagan T. J., Krot A. N., Keil K. and Yurimoto H. (2004a). Oxygen isotopic evolution of amoeboid olivine aggregates in the reduced CV3 chondrites Efremovka, Vigarano, and Leoville. *Geochimica et Cosmochimica Acta* **68**, 2591–2611.
- Fagan T. J., Krot A. N., Keil K. and Yurimoto H. (2004b) Oxygen isotopic alteration in Ca-Al-rich inclusions from Efremovka: Nebular or parent body setting? *Meteoritics & Planetary Science* **39**, 1257–1272.
- Grossman L. (1972) Condensation in the primitive solar nebula. *Geochimica et Cosmochimica Acta* **36**, 597–619.
- Grossman L. (1975) Petrography and mineral chemistry of Ca-rich inclusions in the Allende meteorite. *Geochimica et Cosmochimica Acta* **39**, 433–454.
- Grossman L. (1980) Refractory inclusions in the Allende meteorite. *Annual Review of Earth and Planetary Sciences* **8**, 559–608.
- Grossman L., Ebel D. S. and Simon S. B. (2002) Formation of refractory inclusion by evaporation of condensate precursors. *Geochimica et Cosmochimica Acta* **66**, 145–161.
- Harazono K. and Yurimoto H. (2003) Oxygen isotopic variations in a fluffy Type A CAI from the Vigarano meteorite. (abstract #1540). 34th Lunar Planetary Science Conference. CD-ROM.
- Holst J. C., Olsen M. B., Paton C., Nagashima K., Schiller M., Wielandt D., Larsen K. K., Connelly J. N., Jørgensen J. K., Krot A. N., Nordlund Å. and Bizzarro M. (2013)  $^{182}\text{Hf}$ - $^{182}\text{W}$  age dating of a  $^{26}\text{Al}$ -poor inclusion and implications for the origin of short-lived radioisotopes in the early Solar System. *Proceedings of the National Academy of Sciences of the United States of America* **110**, 8819–8823.
- Hsu W., Wasserburg G. and Huss G. (2000) High time resolution by use of the  $^{26}\text{Al}$  chronometer in the multistage formation of a CAI. *Earth and Planetary Science Letters* **182**, 15–29.
- Ito M. and Ganguly J. (2009) Magnesium diffusion in minerals in CAIs: new experimental data for melilites and implications for the Al-Mg chronometer and thermal history of CAIs. (abstract #1753). 40th Lunar Planetary Science Conference.

- Ito M. and Messenger S. (2010) Thermal metamorphic history of a Ca, Al-rich inclusion constrained by high spatial resolution Mg isotopic measurements with NanoSIMS 50L. *Meteoritics & Planetary Science* **45**, 583–595.
- Ito M., Nagasawa H. and Yurimoto H. (2004) Oxygen isotopic SIMS analysis in Allende CAI: details of very early thermal history of the solar system. *Geochimica et Cosmochimica Acta* **68**, 2905–2923.
- Ito M., Yurimoto H. and Nagasawa H. (2000) Microanalysis of oxygen-isotopic distributions in a Type-C calcium-rich inclusion, EK1-04-2 from Allende meteorite. *Meteoritics & Planetary Science* **35**, Supplement, A81.
- Itoh S., Kojima H. and Yurimoto H. (2004) Petrography and oxygen isotopic compositions in refractory inclusions from CO chondrites. *Geochimica et Cosmochimica Acta* **68**, 183–194.
- Itoh S., Makide K. and Yurimoto H. (2008) Calculation of radiogenic  $^{26}\text{Mg}$  of CAI minerals under high precision isotope measurement by SIMS. *Applied Surface Science* **255**, 1476–1478.
- Itoh S. and Yurimoto H. (2003) Contemporaneous formation of chondrules and refractory inclusions in the early solar system. *Nature* **423**, 728–731.
- Katayama J., Itoh S. and Yurimoto H. (2012) Oxygen isotopic zoning of reversely zoned melilite crystals in a Fluffy Type A Ca-Al-rich inclusion from the Vigarano meteorite. *Meteoritics & Planetary Science* **47**, 2094–2106.
- Kawasaki N., Sakamoto N. and Yurimoto H. (2012) Oxygen isotopic and chemical zoning of melilite crystals in a Type A Ca-Al-rich inclusion of Efremovka CV3 chondrite. *Meteoritics & Planetary Science* **47**, 2084–2093.
- Keil K. (2000) Thermal alteration of asteroids: evidence from meteorites. *Planetary and Space Science* **48**, 887–903.
- Kim G. L., Yurimoto H. and Sueno S. (2002) Oxygen isotopic composition of a compound Ca-Al-rich inclusion from Allende meteorite: implications for origin of palisade bodies and O-isotopic environment in the CAI forming region. *Journal of Mineralogical and Petrological Science* **97**, 161–167.
- Kita N. T., Ushikubo T., Knight K.B., Mendybaev R. A., Davis A. M., Richter F. M. and Fournelle J. H. (2012) Internal  $^{26}\text{Al}$ - $^{26}\text{Mg}$  isotope systematics of a Type B CAI: Remelting of refractory precursor solids. *Geochimica et Cosmochimica Acta* **86**, 37–51.
- Kobayashi S., Imai H. and Yurimoto H. (2003) New extreme  $^{16}\text{O}$ -rich reservoir in the early solar system. *Geochemical Journal* **37**, 663–669.
- Krot A. N., Chaussidon M., Yurimoto H., Sakamoto N., Nagashima K., Hutcheon I. D.

- and MacPherson G. J. (2008) Oxygen isotopic compositions of Allende Type C CAIs: Evidence for isotopic exchange during nebular melting and asteroidal metamorphism. *Geochimica et Cosmochimica Acta* **72**, 2534–2555.
- Krot A. N., Makide K., Nagashima K., Huss G. R., Ogliore R. C., Ciesla F. J., Yang L., Hellebrand E. and Gaidos E. (2012) Heterogeneous distribution of  $^{26}\text{Al}$  at the birth of the solar system: Evidence from refractory grains and inclusions. *Meteoritics & Planetary Science* **47**, 1948–1979.
- Krot A. N., Yurimoto H., Hutcheon I. D., Chaussidon M., MacPherson G. J. and Paque J. (2007) Remelting of refractory inclusions in the chondrule-forming regions: Evidence from chondrule-bearing type C calcium-aluminum-rich inclusions from Allende. *Meteoritics & Planetary Science* **42**, 1197–1219.
- Krot A. N., Yurimoto H., Hutcheon I. D. and MacPherson G. J. (2005) Chronology of the early Solar System from chondrule-bearing calcium-aluminum-rich inclusions. *Nature* **434**, 998–1001.
- Larsen K. K., Trinquier A., Paton C., Schiller M., Wielandt D., Ivanova M. A., Connelly J. N., Nordlund Å., Krot A. N. and Bizzarro M. (2011) Evidence for magnesium isotope heterogeneity in the solar protoplanetary disk. *The Astrophysical Journal Letters* **735**, L37–L43.
- LaTourrette T. and Wasserburg G. J. (1998) Mg diffusion in anorthite: implications for the formation of early solar system planetesimals. *Earth and Planetary Science Letters* **158**, 91–108.
- Liermann H-P. and Ganguly J. (2002) Diffusion kinetics of  $\text{Fe}^{2+}$  and Mg in aluminous spinel: Experimental determination and applications. *Geochimica et Cosmochimica Acta* **66**, 2903–2913.
- Lodders (2003) Solar system abundances and condensation temperatures of the elements. *The Astrophysical Journal* **591**, 1220–1247.
- MacPherson G. J. (2003) Calcium-Aluminum-rich inclusions in chondritic meteorites. In *Meteorites, comets, and planets*, edited by Davis A. M. Treatise on Geochemistry, vol. 1. Oxford: Elsevier-Pergamon. pp. 201-246.
- MacPherson G. J., Davis A. M. and Zinner E. K. (1995) The distribution of aluminum-26 in the early Solar System-A reappraisal. *Meteoritics* **30**, 365–386.
- MacPherson G. J. and Grossman L. (1981) A once-molten, coarse-grained, Ca-rich inclusion in Allende. *Earth and Planetary Science Letters* **52**, 16–24.
- MacPherson G. J. and Grossman L. (1984) Fluffy Type A Ca-, Al-rich inclusions in the Allende meteorite. *Geochimica et Cosmochimica Acta* **48**, 29–46.

- MacPherson G. J. and Huss G. R. (2005) Petrogenesis of Al-rich chondrules: Evidence from bulk compositions and phase equilibria. *Geochimica et Cosmochimica Acta* **69**, 3099–3127.
- MacPherson G. J., Kita N. T., Ushikubo T., Bullock E. S. and Davis A. M. (2012) Well-resolved variations in the formation ages for Ca-Al-rich inclusions in the early Solar System. *Earth and Planetary Science Letters* **331–332**, 43–54.
- MacPherson G. J., Paque J. M., Stolper E. and Grossman L. (1984) The origin and significance of reverse zoning in melilite from Allende Type B inclusions. *The Journal of Geology* **92**, 289–305.
- Maruyama S. and Yurimoto H. (2003) Relationship among O, Mg isotopes and petrography of two spinel-bearing compound chondrules. *Geochimica et Cosmochimica Acta* **67**, 3943–3957.
- Maruyama S., Yurimoto H. and Sueno S. (1999) Oxygen isotope evidence regarding the formation of spinel-bearing chondrules. *Earth and Planetary Science Letters* **169**, 165–171.
- Mendybaev R. A., Richter F. M., Georg R. B., Janney P. E., Spicuzza M. J., Davis A. M. and Valley J. W. (2013) Experimental evaporation of Mg- and Si-rich melts: Implications for the origin and evolution of FUN CAIs. *Geochimica et Cosmochimica Acta* **123**, 368–384.
- Mishra R. K. and Chaussidon M. (2014) Timing and extent of Mg and Al isotopic homogenization in the early inner Solar System. *Earth and Planetary Science Letters* **390**, 318–326.
- Morioka M. (1981) Cation diffusion in olivine–II. Ni-Mg, Mn-Mg, Mg and Ca. *Geochimica et Cosmochimica Acta* **45**, 1573–1580.
- Müller T., Dohmen R., Becker H. W., ter Heege J. H. and Chakraborty S. Fe-Mg interdiffusion rates in clinopyroxene: experimental data and implications for Fe-Mg exchange geothermometers. *Contributions to Mineralogy and Petrology* **166**, 1563–1576.
- Osborn E. and Schairer J. F. (1941) The ternary system pseudowollastonite-åkermanite-gehlenite. *American Journal of Science* **239**, 715–763.
- Oishi Y. and Ando K. (1984) Oxygen self-diffusion coefficient in single-crystal forsterite. In *Materials science of the Earth's interior*, edited by Sunagawa I. Terra Science Publishing Company, Tokyo, Japan. pp. 271–280.
- Onuma K and Moridaira H. (1991) The system diopside-åkermanite-gehlenite at 1 atm. *Journal of Mineralogy, Petrology and Economic Geology* **86**, 554–559.

- Paque J. M., Sutton S. R., Simon S. B., Beckett J. R., Burnett D. S., Grossman L., Yurimoto H., Itoh S. and Connolly Jr H. C. (2013) XANES and Mg isotopic analyses of spinels in Ca-Al-rich inclusions: Evidence for formation under oxidizing conditions. *Meteoritics & Planetary Science* **48**, 2015–2043.
- Park C., Wakaki S., Sakamoto N., Kobayashi S. and Yurimoto H. (2012) Oxygen isotopic variations of melilite crystals in a Type A CAI from Allende. *Meteoritics & Planetary Science* **47**, 2070–2083.
- Podosek F. A., Zinner E. K., MacPherson G. J., Lundberg L. L. Brannon J. C. and Fahey A. J. (1991) *Geochimica et Cosmochimica Acta* **55**, 1083–1110.
- Richter F. M., Davis A. M., Ebel D. S. and Hashimoto A. (2002) Elemental and isotopic fractionation of Type B calcium-, aluminum-rich inclusions: experiments, theoretical considerations, and constraints on their thermal evolution. *Geochimica et Cosmochimica Acta* **66**, 521–540.
- Richter F. M., Janney P. E., Mendybaev R. A., Davis A. M. and Wadhwa M. (2007) Elemental and isotopic fractionation of Type B CAI-like liquids by evaporation. *Geochimica et Cosmochimica Acta* **71**, 5544–5564.
- Ryerson F. J. and McKeegan K. D. (1994) Determination of oxygen self-diffusion in åkermanite, anorthite, diopside, and spinel: Implications for oxygen isotopic anomalies and the thermal histories of Ca-Al-rich inclusions. *Geochimica et Cosmochimica Acta* **58**, 3713–3734.
- Sakamoto N., Seto Y., Itoh S., Kuramoto K., Fujino K., Nagashima K., Krot A. N. and Yurimoto H. (2007) Remnants of the early solar system water enriched in heavy oxygen isotopes. *Science* **317**, 231–233.
- Scott E. R. D. and Krot A. N. (2003) Chondrites and their components. In *Meteorites, comets, and planets*, edited by Davis A. M. Treatise on Geochemistry, vol. 1. Oxford: Elsevier-Pergamon. pp. 143–200.
- Sheng Y. J., Wasserburg G. J. and Hutcheon I. D. (1992) Self-diffusion of magnesium in spinel and in equilibrium melts: Constraints on flash heating of silicates. *Geochimica et Cosmochimica Acta* **56**, 2535–2546.
- Shu F. H., Shang H., Glassgold A. E. and Lee T. (1997) X-rays and fluctuating x-winds from protostars. *Science* **277**, 1475–1479.
- Simon J. I., Hutcheon I. D., Simon S. B., Matzel J. E. P., Ramon E. C., Weber P. K., Grossman L. and DePaolo D. J. (2011) Oxygen isotope variations at the margin of a CAI records circulation within the solar nebula. *Science* **331**, 1175–1178.
- Simon S. B., Grossman L. and Davis A. M. (1991) Fassaite composition trends during crystallization of Allende Type B refractory inclusion melts. *Geochimica et*

- Cosmochimica Acta* **55**, 2635–2655.
- Stolper E. (1982) Crystallization sequence of Ca-Al-rich inclusions from Allende: An experimental study. *Geochimica et Cosmochimica Acta* **46**, 2159–2180.
- Stolper E. and Paque J. M. (1986) Crystallization sequences of Ca-Al-rich inclusions from Allende: The effects of cooling rate and maximum temperature. *Geochimica et Cosmochimica Acta* **50**, 1785–1806.
- Tronche E. J., Hewins R. H. and MacPherson G. J. (2007) Formation conditions of aluminum-rich chondrules. *Geochimica et Cosmochimica Acta* **71**, 3361–3381.
- Ushikubo T., Kimura M., Kita N. T. and Valley J. W. (2012) Primordial oxygen isotope reservoirs of the solar nebula recorded in chondrules in Acfer 094 carbonaceous chondrite. *Geochimica et Cosmochimica Acta* **90**, 242–264.
- Wakaki S., Itoh S., Tanaka T. and Yurimoto H. (2013) Petrology, trace element abundances and oxygen isotopic compositions of a compound CAI-chondrule object from Allende. *Geochimica et Cosmochimica Acta* **102**, 261–279.
- Wark D. A. (1987) Plagioclase-rich inclusions in carbonaceous chondrite meteorites: liquid condensates? *Geochimica et Cosmochimica Acta* **51**, 221–242.
- Wark D. A. and Lovering J. F. (1977) Marker events in the early solar system: evidence from rims on Ca-Al-rich inclusions in carbonaceous chondrites. Proceedings, 8th Lunar and Planetary Science Conference. pp. 95–112.
- Wasson J. T., Yurimoto H. and Russell S. S. (2001) <sup>16</sup>O-rich melilite in CO3.0 chondrites: Possible formation of common, <sup>16</sup>O-poor melilite by aqueous alteration. *Geochimica et Cosmochimica Acta* **65**, 4539–4549.
- Wood J. A. and Hashimoto A. (1993) Mineral equilibrium in fractionated nebular systems. *Geochimica et Cosmochimica Acta* **57**, 2377–2388.
- Yoneda S. and Grossman L. (1995) Condensation of CaO-MgO-Al<sub>2</sub>O<sub>3</sub>-SiO<sub>2</sub> liquids from cosmic gases. *Geochimica et Cosmochimica Acta* **59**, 3413–3444.
- Yoshitake M., Koide Y. and Yurimoto H. (2005) Correlations between oxygen-isotopic composition and petrologic setting in a coarse-grained Ca, Al-rich inclusion. *Geochimica et Cosmochimica Acta* **69**, 2663–2674.
- Yurimoto H., Ito M. and Nagasawa H. (1998) Oxygen isotope exchange between refractory inclusion in Allende and solar nebula gas. *Science* **282**, 1874–1877.
- Yurimoto H. and Kuramoto K. (2004) Molecular cloud origin for the oxygen isotope heterogeneity in the solar system. *Science* **305**, 1763–1766.
- Yurimoto H., Morioka M. and Nagasawa H. (1989) Diffusion in single crystals of melilite: I. Oxygen. *Geochimica et Cosmochimica Acta* **53**, 2387–2394.
- Yurimoto H., Nagasawa H., Mori Y. and Matsubaya O. (1994) Micro-distribution of

- oxygen isotopes in a refractory inclusion from the Allende meteorite. *Earth and Planetary Science Letters* **128**, 47–53.
- Yurimoto H., Krot N. K., Choi B., Aléon J., Kunihiro T. and Brearley A. J. (2008) Oxygen isotopes in chondritic components. In *Oxygen in the Solar System*, edited by MacPherson G. J. Reviews in Mineralogy and Geochemistry, vol. 68. Washington, D. C.: Mineralogical Society of America. pp. 141–186.
- Zhang A-C., Itoh S., Sakamoto N., Wang R-C. and Yurimoto H. (2014) Origins of Al-rich chondrules: Clues from a compound Al-rich chondrule in the Dar al Gani 978 carbonaceous chondrite. *Geochimica et Cosmochimica Acta* **130**, 78–92.
- Zhang X., Ganguly J. and Ito M. (2010) Ca-Mg diffusion in diopside: tracer and chemical inter-diffusion coefficients. *Contributions to Mineralogy and Petrology* **159**, 175–186.